Numerical investigation of Marine Hydrokinetic Turbines: methodology development for single turbine and small array simulation, and application to flume and full-scale reference models.

Amir Teymour Javaherchi Mozafari

A dissertation submitted in partial fulfillment
of the requirements for the degree of

Doctor of Philosophy

University of Washington

2014

Program Authorized to Offer Degree: Mechanical Engineering

University of Washington
Graduate School

This is to certify that I have examined this copy of a Ph.D. dissertation by

Amir Teymour Javaherchi Mozafari

and have found that it is complete and satisfactory in all respects,
and that any and all revisions required by the final
examining committee have been made.

_____

Alberto Aliseda

Committee Members:

_____

Alberto Aliseda

_____

Dana Dabiri

_____

Brian Fabian

_____

Brian Polagye

_____

Jim Riley

Date: _____

University of Washington

Abstract

Numerical investigation of Marine Hydrokinetic Turbines: methodology development for single turbine and small array simulation, and application to flume and full-scale reference models.

Amir Teymour Javaherchi Mozafari

Professor Alberto Aliseda
Department of Mechanical Engineering

A hierarchy of numerical models, Single Rotating Reference Frame (SRF) and Blade Element Model (BEM), were used for numerical investigation of horizontal axis Marine Hydrokinetic (MHK) Turbines. In the initial stage the SRF and BEM were used to simulate the performance and turbulent wake of a flume- and a full-scale MHK turbine reference model. A significant level of understanding and confidence was developed in the implementation of numerical models for simulation of a MHK turbine. This was achieved by simulation of the flume-scale turbine experiments and comparison between numerical and experimental results. Then the developed numerical methodology was applied to simulate the performance and wake of the full-scale MHK reference model (DOE Reference Model 1). In the second stage the BEM was used to simulate the experimental study of two different MHK turbine array configurations (i.e. two and three coaxial turbines). After developing a numerical methodology using the experimental comparison to simulate the flow field of a turbine array, this methodology was applied toward array optimization study of a full-scale model with the goal of proposing an optimized MHK turbine configuration with minimal computational cost and time. In the last stage the BEM was used to investigate one of the potential environmental effects of MHK turbine. A general methodological approach was developed and experimentally validated to investigate the effect of MHK turbine

wake on the sedimentation process of suspended particles in a tidal channel.

TABLE OF CONTENTS

LIST OF FIGURES

LIST OF TABLES

ACKNOWLEDGMENT

I am heartily thankful to my adviser, professor Alberto Aliseda, whose encouragement, supervision and support from the preliminary to the concluding level helped me in developing and understanding of this subject. I would also like to thank National Northwest Marine Renewable Energy Center (NNMREC) and its faculty members at University of Washington for supporting this thesis both financially and scientifically. Last but not the least, I want to thank my parents, brother, family and friends for their never ending moral support.

DEDICATION

To my mother, father and brother
who helped to make this dream come true.

Chapter 1
INTRODUCTION

1.1 Renewable Energy

"Renewable Energy" is a term that has drawn the attention of scientists, engineers and even politicians toward itself during last five decades. The main idea behind renewable energy is to take advantage of the available natural energy resources, such as sun, wind, tides and many more, and convert them to the desired form of energy such as electricity. The generation of the electricity from renewable energy resources while minimizing any possible environmental effects is a positive alternative to mitigate the currently extraordinary use of fossil fuels. From a purely economic, purely environmental, purely strategic viewpoint, or any combination thereof, decreasing the use of fossil fuels in stationary electricity generation is a winning proposition and represents one of the major engineering challenges for the 21^{st} century.

The available technologies for harvesting different renewable energy resources have various historical backgrounds. Some of these resources have been producing electricity for decades. For example, solar energy is being harvested by solar-thermal or photovoltaic panels to generate thermal and electrical energy respectively. They are being used widely now in European countries such as Spain, Germany and some states such as California in US. Harvesting the kinetic energy of wind via wind turbines is another example of a well-known and developed renewable energy technology, which generates electrical energy from the available kinetic energy of wind in countries such as Denmark, Germany and some states in the US in large commercial scales. On the other hand, there are energy resources and harvesting technologies that are fairly new and in the early stages of research and development. The current challenge with these

resources and technologies is performing research, experiment and developing numerical methodologies to simulate and understand the operation process for harvesting energy. The main goal here is to find answers to the questions and reducing the uncertainty in the economic feasibility (Cost of Energy) and environmental compatibility behind the development and commercialization of these resources and technologies.

One example of the fairly new resources is the Tidal Energy. Recently the increasing demand for electricity in regions with tidal resources has led to significant interest in capturing energy from tidal currents. The idea is to extract the potential energy of tides when it becomes available in the form of kinetic energy in high speed tidal current in channels and estuaries. Tidal turbines operate in a very similar way to wind turbines in high wind areas. Therefore, it is believed that today tidal technology is at a stage of research similar to where wind energy technology was three decades ago. However, a significant number of technical as well as environmental issues of tidal technology are different from wind. Hence, they need to be addressed and investigated via experimental or numerical studies a priori, before large scale device deployment and commercialization. This puts the tidal technology at a critical point in the maturity and to reach the stage of production and commercialization. It is hoped that this research on numerical methodology development and validation for characterization of tidal turbines will guide this technology to be commercialized in a similar, but faster, way to how the wind energy industry has evolved. This development can help reduce the ever increasing demand for fossil fuels.

1.2 Tidal Energy, a Renewable Energy Resource.

Tides are formed due to the attraction forces between the sun, moon and earth. Based on Newton's law of gravitation, two different masses, m_1 and m_2, with a distance r between them, attract each other with a force pointing along the line intersecting the masses. This force is directly proportional to two masses and inversely proportional to the square of the distance between them:

$$F_{12} = F_{21} = G \,.\, \frac{m_1 \,.\, m_2}{r^2}. \tag{1.1}$$

In this equation F_{12} and F_{21} are the attraction forces and G is the universal gravitational constant, equal to $6.6743 \times 10^{-11}[N(\frac{m}{kg})^2]$. Therefore, the exerted attraction force by the sun and moon on the earth changes the height of the sea and ocean water level as the orientation and location of the earth and moon changes with respect to the sun [1]. Since the distance between earth and moon is smaller than the distance between sun and earth, the moon is responsible, on average, for about 70% of the tide strength, while sun causes about 30% of the effect on tides.

The strongest and weakest tides are called *spring* and *neap* tides, respectively. As shown on top of the figure 1.1, neap tide form when the sun and moon are in opposite positions with respect to earth. As a result of this orientation, shown at the top of figure 1.1, the gravitational forces work against each other and form neap tides. Spring tides form when the sun and moon are in line with earth and attraction forces are in a direction that are added together to form the strongest tide as shown at the bottom of figure 1.1.

The tides generated from the attraction forces between the sun, moon and earth will result in strong tidal currents in regions where the water elevation drives high flows through narrow passages carrying a significant amount of kinetic energy. The specific flux of kinetic energy in these tidally current flows is defined as follows:

$$P = \frac{1}{2}\rho A V^3. \tag{1.2}$$

In this equation ρ is the density of the fluid (i.e. sea water), A is the cross sectional area that the current goes through and V is the velocity of the flowing fluid (i.e. tidal current). An interesting point is that, although the average velocity of tides (2 to 3 $[\frac{m}{s}]$) is smaller than the average wind velocity (12 $[\frac{m}{s}]$), water is 850 times denser than air and therefore tidal currents have significant energy conversion potential even for

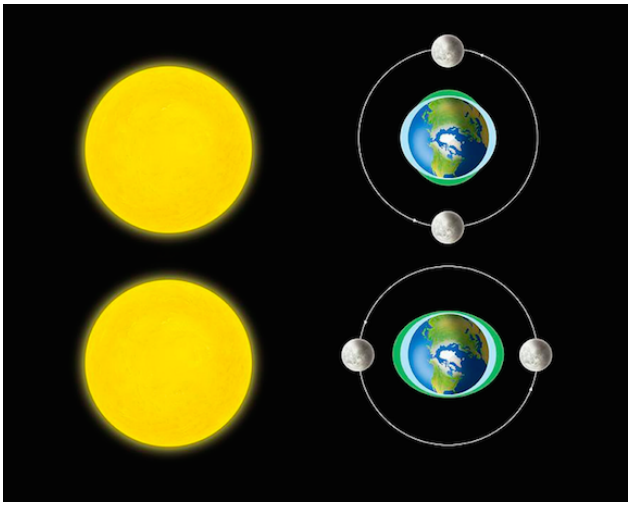

Figure 1.1: **Schematic of Spring and Neap tides formation based on the sun, moon and earth orientation. (source: http://fineartamerica.com/featured/neap-and-spring-tides-diagram-gary-hincks.html)**

relatively slow velocities. As long as extracting the available power from wind via wind turbines was a successful process, harvesting the tidal energy seems to be promising as well. The idea of harvesting the available energy of tidal current via tidal turbines is very similar to harvesting the kinetic energy of wind. Although energy generation from tidal currents has many similarities to wind, the balance between kinetic and potential energy is a key element in tidal channels that invalidates "Betz's" limit at high blockage ratios [2]. Cavitation is another concern regarding harvesting the tidal energy that differentiates the design of Marine Hydrokinetic (MHK) turbines from wind turbines. These similarities and differences of tidal and wind energy made this area of research interesting and has attracted significant attention to develop and commercialize tidal energy from both industrial and economical point of view as well as meeting the long term goals of generating energy from renewable energy sources. The evolution in device development to efficiently extract energy from tides is also

similar to wind energy technology. At this R&D early stages for tidal turbines, different shapes and types of devices are being suggested from different companies. Few samples of the proposed designs, such as the ring configuration from Open Hydro or the cross flow horizontal axis configuration from Ocean Renewable Power Company (ORPC) turbine are shown in figure 1.2. In this thesis, however, we have chosen to study a traditional horizontal axis turbine with axial flow, similar to the predominant design in the wind energy industry. There are multiple proposed designs that follow this configuration, such as SeaGen design shown in figure 1.2.

As mentioned earlier in the early stages of development in the wind industry, similarly different shapes and designs were proposed for wind turbines and, after a long process of optimization and redesigns, the horizontal axis, three-bladed turbine has emerged as the leading commercial-scale offering for electricity generation from wind. It is possible that the MHK industry will follow a similar process. But it is not our intention to choose winners or predict the future. Simply, we have studied the Horizontal Axis Tidal Turbine (HATT) concept to build on the wealth of methods and existing information on the aerodynamics of this design from thirty years of wind turbine development. The goal of this thesis is developing and validating general numerical methodologies and guidelines for analysis various aspects of HAHTs, such as performance and flow field characterization of a single HAHT, optimization and characterization of turbines array and investigation the potential environmental effects of these devices.

(a) SeaGen tidal turbine

(b) ORPC tidal turbine

(c) Openhydro tidal turbine

Figure 1.2: **Different tidal turbine designs. (source: from companies website)**

1.3 Literature Review

Previous studies on energy extraction from tidal resources show that scientists, engineers and device developers are interested in building methodologies for characterization of available tidal resources as well as devices. In 2007 Couch et. al. [3] pointed out two main procedures for understanding and developing the energy extraction technology from tidal energy sources. The first procedure was specifying a methodology for characterization of the resource available at the proposed tidal sites and the second one was developing a methodology for device performance characterization. They also mentioned that the potential environmental effects of power extraction in isolated devices or at commercial scale is a knowledge gap that should be filled. Therefore, the focus of this thesis is mainly on development and validation of numerical methodologies to investigate on the flow field and performance characterization of HAHTs. Later on these methodologies are used as a tool to characterize performance of HAHTs array and optimization of their configuration. These developed numerical tools are also used for investigation on one of the important potential environmental effects of HAHT (turbine-sedimentation interaction). This section presents a broad review of the previous work done in the above-mentioned research branches of marine hydrokinetic technology, which are the basis of the work presented in this thesis.

Characterization of Single HAHT

On the area of single device performance characterization one of the very first works was done by Bahaj et al. [4]. They performed research on development and validation of a numerical methodology for characterization of HAHTs. First, they ran a set of experiments on an 800 [mm] diameter device that modeled a 16 [m] diameter HAHT turbine, in a 2.4 [m] by 1.2 [m] cavitation tunnel. A consistent set of experimental data was generated, which provided useful design information suitable for validation process of theoretical and numerical methods in future. Later, Batten et al. [5] used

the above-mentioned experimental data to validate a numerical scheme for modeling HAHTs. This numerical model was based on blade element momentum theory and a model for wind turbine design developed by Barnsley and Wellicome in 1990 [6]. This model integrates the effect of rotating blades, by having the geometrical (i.e. pitch angle and chord length) and physical variables (i.e lift and drag coefficients) for the predefined elements along the span of the blades as inputs. In this study, the geometrical specifications were known from the blade design step for the experimental setup. However, the physical variables were calculated with the 2D panel code XFoil, which is a linear vorticity stream function panel method [7, 8]. The numerical results, such as power and thrust coefficients, were validated against the experimental results from previous studies and good agreement was found between two sets of results. This validated numerical method could be used as a tool for designing and optimizing energy output with current data from specific locations [5].

The above-mentioned works are just few examples of the introductory experimental and numerical studies on marine hydrokinetic devices, specifically HAHT. Ng et. al. provide a summary of more research and work done on various aspects of HAHT from 2002 to 2012 in a review paper [9]. In this review paper Ng. et. al. narrate the story of nucleation and evolution of R&D on HAHTs. They review numbers of the previous work on tidal site assessment, experimental and numerical analysis of performance and wake of the HAHTs, and the potential environmental effect of HAHTs.

At the current research stage, after about one decade of research and development, that enormous amount of time and effort were invested on addressing, investigating and understanding various aspects of marine hydrokinetic technology, researchers and engineers are working together on proposing and modeling optimized reference or industrial models for HAHTs [10–12]. The main goal behind the current efforts is to have more successful, from technical and environmental aspects, pilot and commercial device deployment for electricity production in the near future.

The US department of Energy (DOE) in collaboration with the National Renew-

able Energy Laboratory (NREL) recently proposed a new turbine design, officially named DOE Reference Model 1 (DOE RM1), as an open source design for HAHT. Researchers can use this design to benchmark numerical models and simulations. Lawson et al. [11] have performed numerical analysis on this reference model using RANS-based simulation. They performed mesh resolution studies for numerical modeling of the DOE RM1 and also some performance and flow field analysis.

Gunawan et. al. present the numerical modeling of a three bladed horizontal axis turbine, called Sandia National Laboratories' Axial Flow Hydrokinetic Turbine (SAFT) [13]. This turbine is another reference model for HAHT. In this work rotating reference model in a RANS simulation closed with SST $k-\omega$ turbulent model, implemented in STAR-CCM+, is used to numerically model the performance and wake of the turbine. Gunawan et. al. compared the corresponding numerical and experimental values of the device's integral variables (i.e. performance, thrust and torque coefficients) and reported a good agreement. Furthermore, in this work two components, streamwise and vertical, of the modeled and measured velocity deficit profiles in turbine wake are compared against each other. However, in the presented results the experimental data in various downstream stations are not fully captured and presented. This has limited the accuracy and completeness of this comparison at multiple stations downstream the turbine.

Another recent interesting study on numerical modeling of HATH was done by Kang et al. [12] at Anthony Falls Laboratory (SAFL) in the University of Minnesota. This work is based on a previously-developed Large Eddy Simulation (LES) for analysis of HAWTs. Kang et al. performed LES on the Gen4 axial flow MHK turbine developed by Verdant Power for the Roosevelt Island Tidal Energy (RITE) project in the East River in New York City, USA. They performed a very detailed study of the near wake of this turbine, modeling the full turbine structure (i.e. blades, nacelle and base), and analyzing the coherent vortex structures shed in the near wake.

Beside the ongoing research on study of HAHTs there are many other numerical

and experimental investigations on the other MHK turbine designs. One of these design is the cross-flow turbine. Polagye et. al. presented results from numerical simulations, laboratory experiment and filed studies on a helical, cross flow turbine [14]. In this work they emphasized on performance and wake characterization of the device and responsiveness of the device to the inflow turbulence condition. According to comparison of the results, from three different approaches, they concluded that in the cross-flow turbines the dynamic stall and the blockage ratio are the two main variables that need careful consideration when this turbine design is modeled numerically via RANS-based simulations. Furthermore, Bachant and Wosnik performed numerical and experimental analysis on a three bladed cross-flow turbine, called UNH-RVAT [15] [16]. In their most recent paper [16] they investigate the effect of Reynolds number on the performance and wake evolution of this specific MHK turbine design. On the numerical side of this study, the turbine was modeled using 2D RNAS closed with $k-\omega$ SST model, implemented in OPEN FOAM. Despite the fact that their experimental results showed Reynolds number independency for the turbine performance, their numerical results revealed a strong Reynolds dependency for the device efficiency. Bachant et. al. hypothesized the reason behind this disagreement is the effect of the increased blockage ratio in 2D simulation compared to 3D experiment. On the other hand, in this work a good agreement between the measured and experimental velocity deficit in the wake was reported, which lent credibility to the presented numerical approach.

In this thesis a general numerical methodology, consist of a hierarchy of numerical models, is validated against experimental data for a modified scaled-model of the DOE RM1 turbine [17]. After validation, this methodology is applied toward study of the full-scale DOE RM1. The main difference between the presented work in this thesis and previously cited papers is in the step-by-step presentation of validation and application procedure of the methodology for study of HAHT. Our numerical methodology development started with the NREL Phase VI two-bladed wind turbine [18].

We took advantage of the previous numerical modeling techniques for study of this turbine [19–22], and developed the work flow to simulate a turbine design with a hierarchy of models that capture different aspects of the flow physics. We validated the results of this methodology, including the meshing, turbulence closure models, boundary conditions, etc. [23] based on experimental results for the NREL Phase VI wind turbine available in the open literature [24]. The steps for application of this same techniques for investigation on lab.- and full-scale DOE RM1 turbine are presented in this thesis. It is showed that following the presented step-by-step methodology in this work will result in precise simulation of a performance and wake characterization of HAHT, while it significantly reduces the required time and effort for developing these simulations from scratch (1-2 years time and effort would be reduced to 1-2 months). This is one of the available knowledge gap in previous work, lack of presentation of the steps for developing the numerical models, that has been tried to be filled in chapter 2 of this work.

Characterization of HAHT Array

In the area of HAHT array simulation, various works has been done since 2005. In these works different combination of numerical models are used to simulate wake and performance of turbines in an array. The spectrum of these numerical approaches is very wide and varies from a 2D finite element model with turbines being simulated in via a drag force [25] to the combination of different implementation of Blade Element Theory (BET) with RANS-based simulations [26–28]. In majority of these works first the numerical model is developed and validated to simulate the performance and flow field around an isolated turbine. Once the methodology is developed successfully it is used to model various array configurations. The primary goal of these studies is investigation on the role of possible dominant constraints (i.e. lateral or offset spacing between devices [28–31] and direction of blade rotation [29] [32]) on the performance of the turbine array. The main contribution of these works was toward the development

of various numerical methodologies for study of HAHTs arrays and discovering the functionality between the array performance and most important constraints. However, the main unanswered question in all of the previously cited works is the lack of a general methodological approach for array optimization process. Results presented in the above-mentioned references are specific to the configurations studied and do not provide a general process to answer the questions relevant to array optimization in any setting. Chapter 3 of this thesis fills this knowledge gap and provide general guidelines for the optimization process that can be applied to any turbine design, any channel conditions and any array configuration.

Investigation on a Potential Environmental Effect of HAHT

Addressing and investigating the potential environmental effects of MHK turbines is a fairly new area of research and development compared to the other branches of research in field of marine renewable energy. There are some works that initiated the investigation on potential interactions between MHK technology and marine life: Polagye et. al. published a technical report on environmental effects of tidal energy development in 2010 [33]. Bassett et. al. performed comprehensive investigations on the noise level in admiralty inlet from different aspects to characterize potential effects of MHK devices' noise on marine life in this proposed tidal site [34] [35]. Researches and scientists in Pacific Northwest National Laboratory (PNNL) performed number of research and investigations on potential interaction of fish with marine hydrokinetic- and hydroelectric turbines. These studies were both performed experimentally [36–38] and numerically [39]. In Saint Anthony Falls Laboratory (SAFL) Hill et. al. are performing experimental investigation on interactions between near and far-field sediment transport and HAHT performance for single and multiple turbines. However, the results of these studies are not publicly available yet. Furthermore, US Department of Energy has recently funded Sandia Lab. to initiate research projects to study the potential interaction of turbine-sedimentation in tidal channel.

These are only few examples of the most recent top of the edge research going on in this field. As mentioned earlier these works are all in the early stages of the development and have room become more precise and oriented toward making conclusions on the level of severity for each of the named potential effect of the MHK turbines. Similar to these works chapter 4 of this thesis discuss the development of a numerical methodology to simulate particle motion in highly turbulent flows (tidal channels). This methodology can be used as a tool to model interaction between near- and far flow of a MHK turbine with suspended particles in tidal channels. At the last part of this thesis the developed methodology, for modeling particle motions in a tidal channel, is applied toward addressing and investigating the turbine wake and suspended sediments interaction.

The main goal of this thesis is to apply general CFD techniques to simulate the flow field around HAHT, and to develop general methodologies for the analysis of engineering problems, energetics and environmental, that depend on the modification of the marine current flow by the presence of this technology. These tools are expected to contribute to acceleration of the R&D process and fill the existing knowledge gaps in this research field.

Chapter 2

NUMERICAL CHARACTERIZATION OF A SINGLE HORIZONTAL AXIS HYDROKINETIC TURBINE

In this chapter, the characterization of the flow field and performance of two different types of Horizontal Axis Hydrokinetic Turbines (HAHT) is presented. The first turbine is a laboratory scaled-model HAHT turbine. The second one is the full scale DOE Reference Model 1 (DOE RM1) turbine, a two-bladed HAHT designed and published as a reference model by the US Department of Energy. The laboratory-scaled model turbine is a modified design of the full scale DOE RM1 geometry. The rotor was designed to match the performance of the full scale turbine, for a wide range of Tip Speed Ratios ($TSR = \frac{r\omega}{V}$), at the Reynolds number reached at the lab scale ($\mathrm{Re}_{chord} \approx 10^5$), making the experimental study of the flow field and performance of the DOE RM1 possible [17]. Two numerical models with different level of fidelity, Single Rotating Reference Frame (SRF) and Blade Element Model (BEM), were used to match the experimental conditions and simulate the performance and wake of this device [61]. The numerical results presented in the second section of this chapter, provided the foundation for the experimental validation of the numerical methodologies used in this work. The validated numerical methodologies are then applied towards characterization of the flow field and performance of the full scale DOE RM 1 turbine [62]. The results from these numerical simulations are presented in the third section of this chapter. The numerical results from the DOE RM1 simulations in this thesis are compared, at the end of this chapter, against other previous numerical modeling of the DOE RM1 available in the literature [11].

2.1 Numerical Methodology

2.1.1 Single Rotating Reference Frame (SRF)

The Single Rotating Reference Frame (SRF) model is used to solve the Reynolds-Averaged Navier Stokes (RANS) equations in a rotating reference frame. Using this technique, the flow field around and in the wake of a Horizontal Axis Hydrokinetic Turbine (HAHT) blades can be simulated with a relatively simple formulation. In this type of problem, the flow field is unsteady in the fixed, inertial reference frame since the blades are rotating with respect to this frame. However, it is possible to perform calculations in a non-inertial reference frame, rotating with the turbine blades, where the flow is steady. In this formulation, the effect of rotation is input into the equations of fluid motion by adding body forces that represent the inertial effects associated with the centrifugal and Coriolis accelerations felt by the fluid in its motion with respect to the non-inertial reference frame. The addition of these body forces and the transformation of the velocity components due to the change of the frame of reference in the equations of motion are as follows:

$$\frac{\partial \rho}{\partial t} + \nabla \cdot \rho \vec{v}_r = 0, \tag{2.1}$$

$$\frac{\partial}{\partial t}(\rho \vec{v}_r) + \nabla \cdot (\rho \vec{v}_r \vec{v}_r) + \rho(2\vec{\omega} \times \vec{v}_r + \vec{\omega} \times \vec{\omega} \times \vec{r}) = -\nabla p + \nabla \cdot \bar{\bar{\tau}}_r + \vec{F}. \tag{2.2}$$

Here, $\vec{v_r}$ is the velocity relative to the rotating reference frame and is equal to $(\vec{v} - \vec{\omega} \times \vec{r})$, where $\vec{v}$ is the absolute velocity and $(\vec{\omega} \times \vec{r})$ is the velocity due to the rotation of the reference frame. In equation 2.2, $(2\vec{\omega} \times \vec{v}_r)$ is the Coriolis acceleration and $(\vec{\omega} \times \vec{\omega} \times \vec{r})$ is the centripetal acceleration, which are added as body forces to the conservation of momentum equation [88].

This method renders an unsteady problem in a fixed reference frame into a steady problem with respect to the rotating reference frame. This allows the problem to be integrated using a stationary grid and to avoid the complexity and stiffness associated with rotating mesh simulations. The trade-off in the use of this method is that it requires an axisymmetric domain and boundary conditions. This requirement has to be taken into account in selecting the turbulence closure models, since many existing models compute Reynolds stresses in a way that is not independent of the rate of rotation and therefore will not perform well in a rotating reference frame. For more details on the SRF model theory, readers are referred to [18] [23] [88].

2.1.2 Blade Element Model (BEM)

The BEM represents a step down in complexity compared to the SRF for simulation of the flow around turbine rotating blades. This model is based on Blade Element Theory [7] and models the presence of the rotating turbine blades in the computational domain via a fluid sub-domain that occupies the disk swept by the turbine blades over a complete revolution [64]. In the BEM, the blade span is sectioned from root to tip, and the lift and drag forces on each section are computed based on the local angle of attack (AOA), chord length and airfoil shape. The BEM simulates the effect of the rotating blades by imposing on the fluid inside the rotor disk domain (i.e. fluid sub-domain) a body force equal in magnitude but opposite in sign to the lift and drag on each blade element, averaged over a full revolution. Eq. (2.3) shows the formulation of the sectional lift and drag forces.

$$f_{L,D} = C_{L,D}(\alpha, \mathrm{Re}) \; . \; c(r/R) \; . \; \frac{\rho . V_{tot}^2}{2}. \tag{2.3}$$

This equation uses the value of the lift or drag coefficient, $C_{L,D}$ to calculate the body forces applied by the BEM on the fluid domain. These coefficients come from a lookup table that contains the their values as a function of AOA (α) and Reynolds number

(Re) for the blade airfoils. $c(r/R)$ is the chord length of the blade section, ρ is the fluid density and V_{tot} is the fluid velocity relative to the blade. The lift and drag forces calculated for each element are averaged over a full blade revolution to calculate the equivalent source/sink term in each cell of the numerical discretization [67]. The full numerical implementation of the BEM in a numerical RANS solver requires inputs that can be divided into two main groups: the size, number and pitch angle of the wind turbine blades; and the geometrical specifications of the blade sections along its span, with the corresponding lift and drag coefficients look-up tables for each blade element. Each look-up table defines the characteristics of the different airfoil sections along the blade span. With these inputs, the body forces at each blade section are calculated and averaged over the swept area of the blade. The body forces are included into the RANS equations to model the effect of wind turbine rotating blades, in an iterative process. A detailed characterization of this process, with specific examples of input values, is given in [18] [23].

This formulation eliminates the need for creating the actual geometry of the turbine blades and a high resolution mesh around it in the computational domain. Therefore, this rotor representation reduces the mesh count, man-hours required in its generation and computational cost by between 10 and 100 times with respect to blade-resolving methods.*.

2.1.3 Turbulence Model

In this work, the numerical simulations were performed with a commercial finite volume code, FLUENT 13.0 (ANSYS Inc., Cannonsburg, PA), by solving the RANS equations with a turbulence model to provide closure for the Reynolds stress term. Among the turbulent closure models that have been used for flow field simulation

*Due to the absence of a blade geometrical model in this formulation, the implementation of this model in ANSYS FLUENT is called Virtual Blade Model (VBM)

in HAHTs, this work focuses on Shear Stress Transport (SST) $k-\omega$. SST $k-\omega$ is a modification of the original $k-\omega$ model, developed by [44] based on the transport equations for turbulence kinetic energy, k, and specific dissipation rate, ω, that overcomes its limitation for capturing the turbulent boundary layer around the blade. Additionally, far from the boundary layer region, this model transitions to the $k-\epsilon$ model to capture the free-shear flow region in the far wake. Menter developed the SST $k-\omega$ to take the best features from the $k-\omega$ and $k-\epsilon$ models in their respective regions of applicability: the calculation of the turbulent viscosity is modified to account for the transport of the principal turbulent shear stress to include the addition of a cross-diffusion term in the ω equation, and to ensure that the model equations behave appropriately in both the near-wall as well as far-field regions. In near wall regions, the blending function tends toward zero (i.e. the standard ω equation), whereas far from the walls, it tends toward unity (i.e. the standard ϵ equation) [76]. Table 2.1 summarizes the constant values for $k-\omega$ SST, that are used in this work to simulate the flow field around and in the wake of a HAHT.

k - ω **SST**							
α^*_∞	α_∞	β^*_∞	ζ^*	M_{t0}	a_1	$\beta_{i,1}$	$\beta_{i,2}$
1	0.52	0.09	1.5	0.25	0.31	0.075	0.0828
$\sigma_{k,1}$	$\sigma_{k,2}$	$\sigma_{\omega,1}$	$\sigma_{\omega,2}$				
1.176	1	2	1.168				

Table 2.1: **Constant values for the $k-\omega$ SST turbulence model.**

2.1.4 Methodology for Evaluation of Angle of Attack (AOA), 3D Lift and Drag Coefficients Along Turbine Blade Span.

In the process of performance characterization of a newly developed blade turbine design, the lift and drag coefficients are the two important physical variables that should be investigated and evaluated. In this work, the lift and drag coefficients along the blade span are computed with the help of flow field data from the SRF model coupled with RANS simulations. In the absence of experimental data for the coefficient values for the Reynolds number of interest, the computational values of these two non-dimensional coefficients help the blade performance characterization process and provide the opportunity for future validation of the numerical model/methodology. These coefficients can be compared against other measured or estimated values from either experiments or numerical simulations respectively.

In the computational domain of the SRF model, the blade span is divided equally into subsections from root to tip (see figures 2.3 and 2.11). The height of these sections are equal and the chord length varies along the blade span according to the blade design specifications. This blade discretization provides the opportunity to calculate and integrate the perpendicular and parallel force components to the relative incoming fluid flow at each section to evaluate lift and drag forces. Normalization of these forces would provide the lift and drag coefficients. However, the twist angle, chord length and airfoil thickness of each section varies from the root to the tip of this blade. Hence, calculating the flow direction with accuracy is critical to evaluate the force components and normalize them to calculate the lift and drag coefficients within the RANS simulation on each section along the blade span. Due to these uncertainties, a general methodology was developed to calculate the lift and drag forces/coefficients. In this methodology, the force components normal (dF_N) and tangential (dF_T) to the plane of blade rotation are integrated over each blade section (figure 2.1.4).

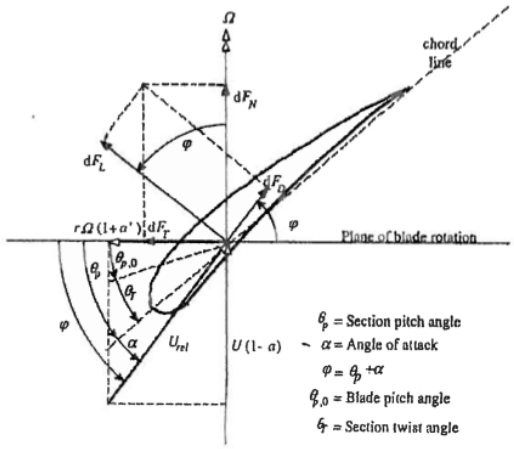

]**Diagram defining the angles, velocity components and resultant force components on a hydrofoil [68].**

The normal (F_N) and tangential force (F_T) components convert to the lift (F_L) and drag forces (F_D) from the simple trigonometric decomposition showed in figure 2.1.4 and defined by:

$$\begin{aligned} F_T &= F_L * Sin(\varphi) - F_D * Cos(\varphi), \\ F_N &= F_L * Cos(\varphi) + F_L * Sin(\varphi). \end{aligned} \tag{2.4}$$

In this system of equations, F_N and F_T are known from the SRF-RANS solution. The values of the angle of relative flow (φ) at each section is not directly known from the RANS solution. This angle is defined based on equation 2.5 as indicated in figure 2.1.4. Values of these angles at each section along the blade span is estimated based on two simplifications. First, the tangential induction factor is considered negligible ($a' = 0$). Second, the value of the local streamwise velocity ($U_\infty(1-a)$) at each blade section is estimated as the average of all the nodal values of streamwise velocity along a parallel plane covering the entire blade span at a specific distance upstream of the blade. This specific distance upstream was chosen based on flow field

visualization in post-processing. This methodology takes into account the effect of the axial induction factor, a, within a certain level of apprximation.

$$\varphi = tan^{-1}(\frac{U_\infty(1-a)}{r\omega(1+a')}) \tag{2.5}$$

The system of equations 2.4 is now determined. Thus, lift and drag forces can be calculated. Solving this system of equations will result in:

$$\begin{aligned} F_L &= F_T * Sin(\varphi) + F_N * Cos(\varphi), \\ F_D &= -F_T * Cos(\varphi) + F_N * Sin(\varphi). \end{aligned} \tag{2.6}$$

Normalization of these forces provides the 3D lift and drag coefficients at each blade section as follows:

$$C_L = \frac{F_L}{\frac{1}{2} * \rho * h * c * V_{rel}^2}, \tag{2.7}$$

$$C_D = \frac{F_D}{\frac{1}{2} * \rho * h * c * V_{rel}^2}, \tag{2.8}$$

where ρ is the fluid density, h is the height of each blade section, c is the chord length and V_{rel} is the relative velocity (i.e. vector summation of the local streamwise velocity and the rotational velocity of the blade element) at each section. As mentioned above, having the three dimensional flow values of lift and drag coefficients as a function of AOA is superior to experimental or theoretical 2D values for turbine characterization based on numerical models that use the Blade Element Theory (BET).

2.2 Experimental Validation of the Numerical Methodology

2.2.1 Experimental Setup

Preliminary experimental results obtained from laboratory testing of a 45:1 geometrically-scaled DOE Reference Model 1 (DOE RM1) rotor showed a low coefficient of per-

formance ($C_p^{maximum} \approx 20\%$) compared to predictions of full-scale DOE RM1 performance based on Blade Element Momentum Theory ($C_p^{maximum} \approx 45\%$) [62]. The relatively low efficiency of the geometrically-scaled DOE RM1 turbine compared to numerically predicted efficiency suggests that the laboratory-scale rotor should be modified in order to be dynamically similar to the full-scale DOE RM1 rotor. The rotor was redesigned to match the efficiency and peak tip speed ratio performance of the full-scale DOE RM1 [17]. The CAD model of this turbine is shown in figure 2.2

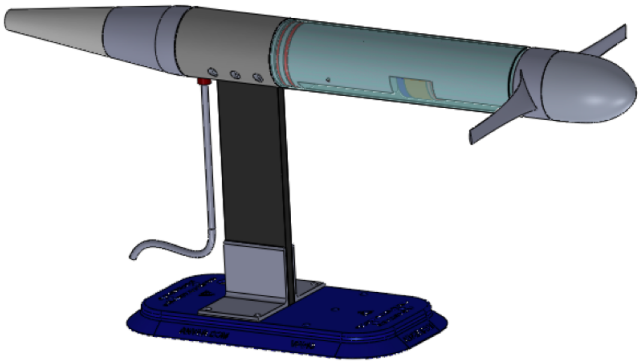

Figure 2.2: **CAD model of the modified scaled HAHT form the DOE RM 1 geometry, built for experimental testing at flume scale [17].**

2.2.2 Numerical Setup

The Single Rotating Reference Frame (SRF) and the Blade Element Model (BEM) methodologies are used to simulate the flow field associated with the laboratory-scale model turbine. As discussed earlier in section 2.1, the SRF and BEM formulations are combined with the RANS equations and a turbulent closure model to investigate the effect of the Tip Speed Ratio variation (TSR=5.5 to 10.3) on the performance and wake structure of a single turbine. The details of the computational domain and

boundary conditions to match the experimental testing conditions is as follows:
Figure 2.3 shows the computational domain and boundary conditions for the SRF model to simulate the flow field and performance of the laboratory scaled HAHT. Taking advantage of the modified DOE RM 1 turbine symmetry (two bladed rotor), only half of the domain is modeled in this thesis. The inlet conditions is constant uniform velocity and the outlet is set to uniform pressure. Cyclic-periodic boundaries are prescribed on the symmetry plane of the domain to simulate the blade rotation. The distance between the domain's top cylindrical boundary and tip of the turbine blade is 0.275 m to match the experimental blockage ratio of 20%. This boundary is modeled with a slip-free boundary condition. Figure 2.3 also shows the span of the blade and the geometry of the nacelle, included in the computational domain. Including the actual geometry of the blade in this model provides the opportunity to capture the details of the flow field in the near wake region.
The SRF computational grid for the scale-model turbine has approximately 4.7x10^6 mesh elements. The mesh is structured in most of the SRF's computational domain, except for a region at the inlet, in front of the nacelle's curved head, and in the wake of the turbine, right behind the tapered section of the nacelle. In these sections, unstructured tetrahedral elements were used. The required mesh resolution around the airfoil sections and along the blade span and other parts of the computational domain were based on the results of previous grid resolution studies [23] and [18]. The concentration of mesh elements in the SRF domain is focused around the blade span to ensure capturing the turbulent boundary layer on the blade surfaces. The number of nodes around the airfoil sections of the blade is 152 with equal spacing. The number of nodes along the blade span is 94 and they are also equally spaced. In the radial direction of the C−mesh, 19 nodes were used, with the first length from the blade wall equal to 0.5 mm. This value of first length was calculated according to the chord-based Reynolds number and the guidelines provided in [18]. For a Reynolds number of 10^5, a first length of 0.5 mm satisfies the range of y^+ between 30-300 to

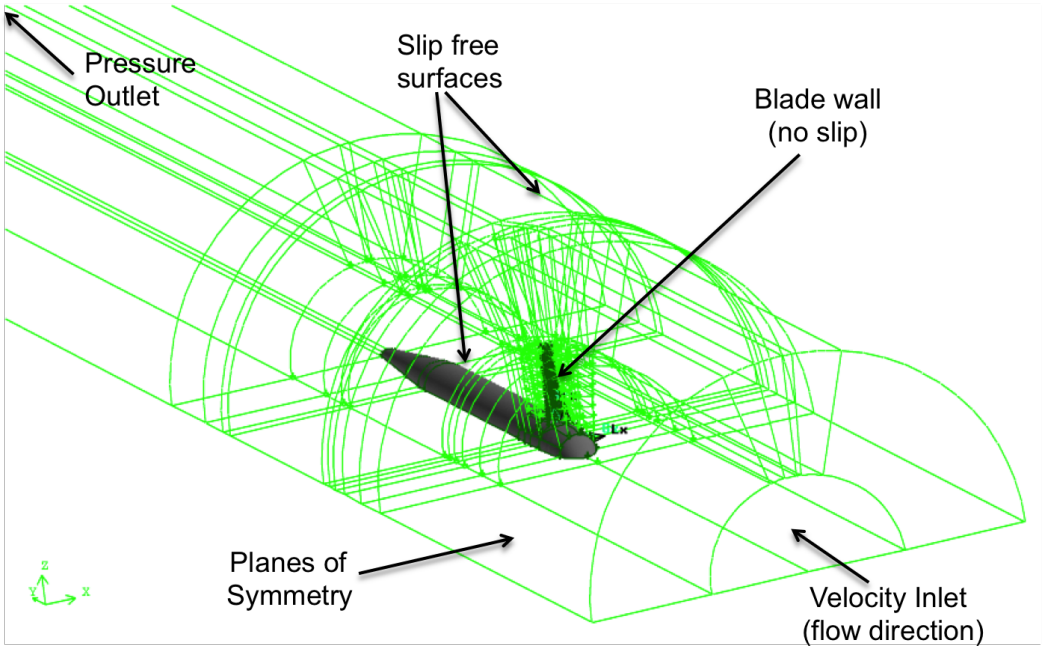

Figure 2.3: **Computational domain and boundary conditions used with the SRF model. The actual geometry of the scaled HAHT blade (gray region) is included in this computational domain.**

capture the turbulent boundary layer along the blade span using the wall functions approach. It should be noted that this mesh resolution should be modified for the full scale simulation as the Reynolds number changes by an order of magnitude.

Figure 2.4 shows the computational domain of the BEM described in section 2.1, including the swept disk of fluid to model the effect of the turbine via body forces, highlighted in gray color. The boundary conditions are: uniform streamwise velocity at the inlet and uniform pressure at the outlet. The outer walls of the domain are modeled as slip-free walls. The actual geometry of the nacelle is reproduced and its solid wall is modeled as a no-slip condition to capture its effect on wake recovery. In this simulation, as opposed to the axisymmetric domain of the SRF simulation, the actual geometry of the experimental flume tests is used as the fluid domain, since

there are no limitations on the geometry of the domain.

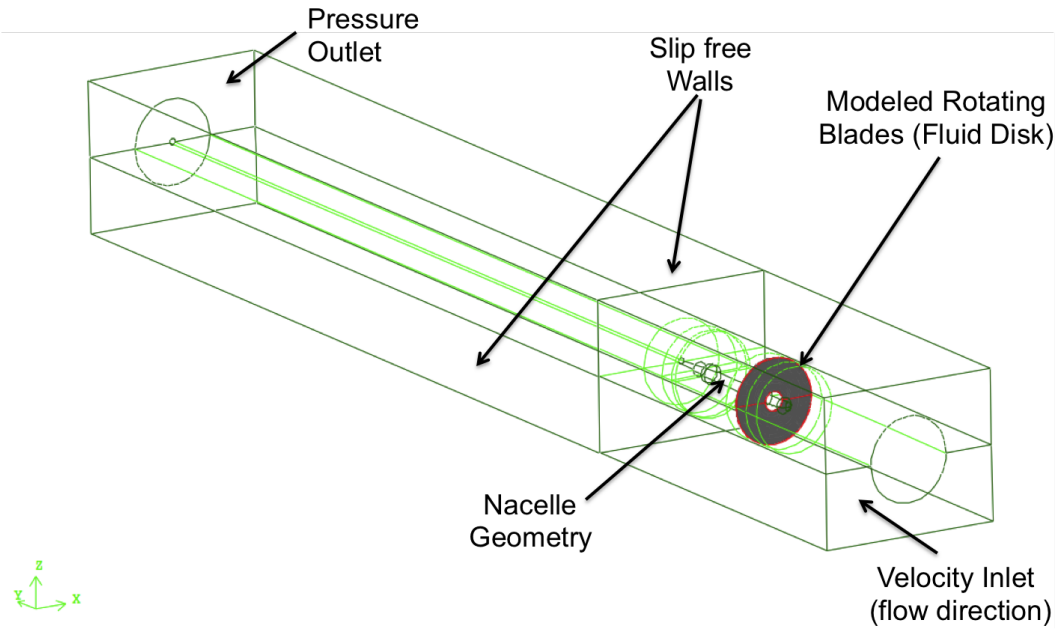

Figure 2.4: **Computational domain and boundary conditions used with BEM. The effect of the turbine is modeled via body forces applied on the disk swept by the rotor (gray region).**

As found in preliminary studies [23], the BEM model results are much less sensitive to mesh resolution than those from the SRF model. BEM greatly simplifies the mesh by using the swept disk to apply forces, instead of the actual blade geometry, to simulate the presence of the turbine rotor. As mentioned above, the required mesh resolution for the BEM computational domain in this study is based on the results in [23]. The BEM domain has about 3.6 10^5 mesh elements. The number of nodes along the width and depth of the rectangular cross section of the domain are 36 and 20 respectively. 237 mesh nodes are placed along the length of the domain with higher concentration in regions close to the rotor plane and 20 mesh nodes were used on the edge of the rotor plane. Similar to the SRF domain, the BEM mesh is structured in most of the

computational domain except for regions at the inlet, nacelle, and wake. In order to capture the turbulent boundary layer along the nacelle, the mesh resolution was adapted to satisfy the wall function requirements on the range of y^+ of the first node near the wall.

2.3 Results

2.3.1 Performance Comparison (SRF, VBM and Experiment)

Figure 2.5 shows the performance predicted by the SRF and BEM, relative to the experimental results. Comparison between the SRF curve (red) and BEM curve (green) shows that the turbine performance values at different TSR from the two models are consistent with each other, within 2-6%. For the majority of the TSR values, other than two extreme ends, BEM predicts higher performance than the SRF. The root of this difference goes back to the simplifications/idealizations used in modeling the hydrodynamic effect of the rotor within the BEM. The BEM averages the hydrodynamic forces on each blade segment over a cycle of rotation, thus, it is limited in capturing three dimensional flow effects at the blade tip or root.

Both numerical models predict a clear peak in efficiency for the scaled model turbine at TSR=8.17, as shown in figure 2.5. Moving from this peak towards the lower TSR values, the predicted performance decreases due to increases in AOA. However, higher TSRs show the agreement between SRF and BEM deteriorating. The cause of disagreement at very high TSR (i.e. TSR=10.33) is that the value of the AOA along the blade span decreases and the three dimensionality near the blade tip becomes more dominant and reduces the overall performance of the turbine. BEM cannot accurately calculate the lift and drag forces in this small but important region and therefore the performance of these blade are modeled poorly compared to the SRF model.

Alternatively, figure 2.5 presents the comparison between the turbine performance

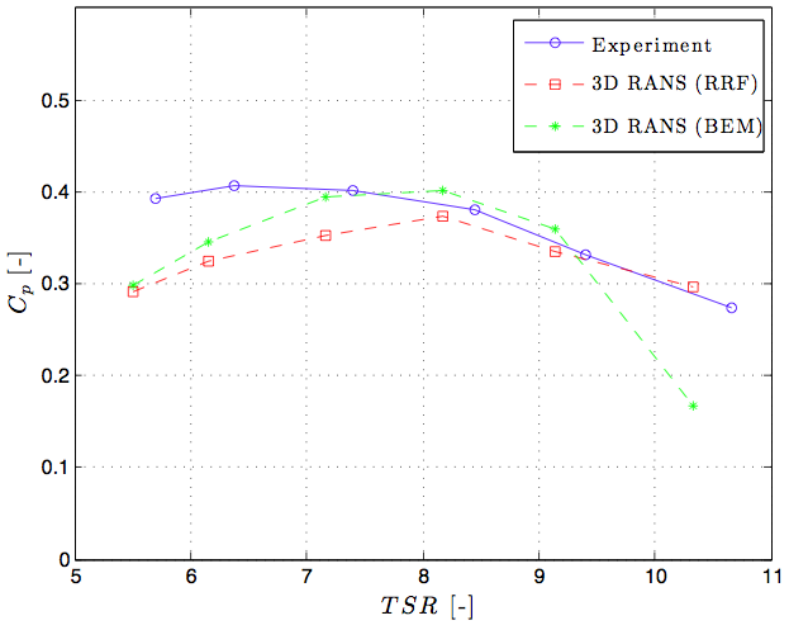

Figure 2.5: **Comparison between the performance curves (C_p vs. TSR) for experimental measurements and numerical analysis (RRF and BEM) for a single scale model HAHT.**

from the experiments and the numerical results. For the range of TSR from 8-10, the experimental and numerical performance coefficients are in good agreement. Analogue to the previous discussions, experimental results confirm that as the value of the TSR increases, the efficiency of the turbine decreases. Under these TSR conditions, the angle of attack for the majority of the airfoils along the blade span moves down from their optimum value, and therefore the power extracted by the turbine decreases. It should be noted that the SRF model, in which the actual geometry of the blade is modeled, closely matches the experimental results in this range of TSR. However, there is a large drop in the BEM prediction at TSR of 10 due to the limitations of this model as explained earlier.

The discrepancy in the efficiency between experiments and computations at lower TSR, from 5-7, brings about interesting information on the dynamics of the turbine rotor. An interesting observation, presented data in figure 2.5, is that the experimentally measured efficiency (blue curve) does not have a clearly-defined maximum. In other words, the turbine efficiency is almost constant for a wide range of TSR values, decreasing from the theoretical peak around 7 to about 5.5 with little change in performance. This is in contradiction with aero- and hydrodynamic principles: decrease in TSR will result in the increase of AOA along the blade span. Large AOA values result in flow separation and unsteadiness along the blade span, and eventually stall, especially close to the root of the blade. These phenomena should decrease the efficiency of the turbine. Further analysis of the experimental data showed that, when the turbine operates under lower TSRs conditions, there is an increase in fluctuations of the rotational velocity, which affects the flow structure at the blade surface, and therefore rotor performance [17].

Figure 2.6 shows the temporal variation of the turbine's rotational velocity at the two ends of the TSR range explored (TSR=5 and 10). The blue and green curves show the temporal variation of rotational speed normalized with the mean for TSRs equal to 5 and 10, respectively. Figure 2.6 confirms that at TSR=10, the rotational speed has small fluctuations. At lower TSR, however, the fluctuations are relatively large and there are even a few large excursions (beyond 3 times the signal rms) during the 60 seconds of measurements. Our hypothesis is that these large fluctuations in the rotational velocity postpone the potential stall at low TSR values (high AOA values). Therefore, the efficiency of the turbine remains high as the TSR value decreases and the turbine still performs close to its maximum efficiency. To investigate this hypothesis, the flow field along the suction side of the blade span in the SRF simulation is shown in figure 2.7.

Wall Shear Stress (WSS) values normalized with their maxima are used to highlight regions of flow detachment. Limited streamlines are superimposed on the WSS

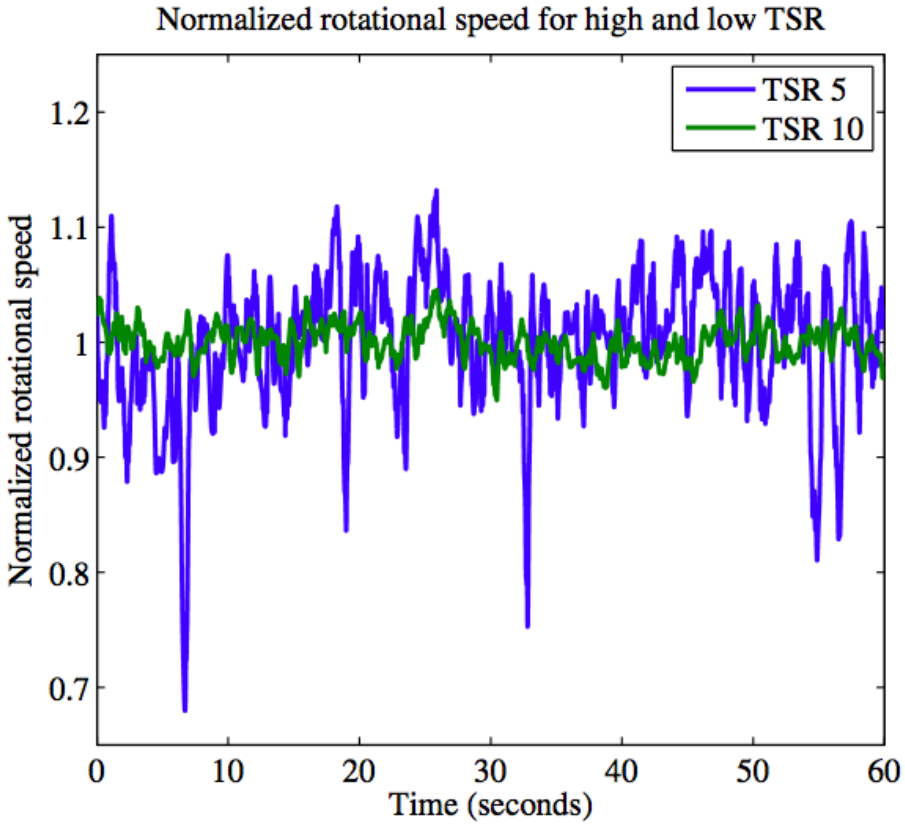

Figure 2.6: **Temporal variation of normalized rotational speed of turbine measured at the two extreme values of the TSR range (TSR=5 and 10).**

color contours to further delineate the extent of flow recirculation. As TSR decreases, from bottom right to top left of the figure, the dark blue region of low WSS grows at the root of the blade. In this region of low WSS, the flow starts to detach from the blade span and the limited streamlines diverge from each other. Significant separated flow exists from TSR 5-7, but not from 7-10. This view supports the hypothesis that fluctuations in angular velocity in the experiment could account for the difference, by postponing stall and helping to maintain a quasi-constant coefficient of performance for the turbine that is not predicted by theory or numerical simulations.

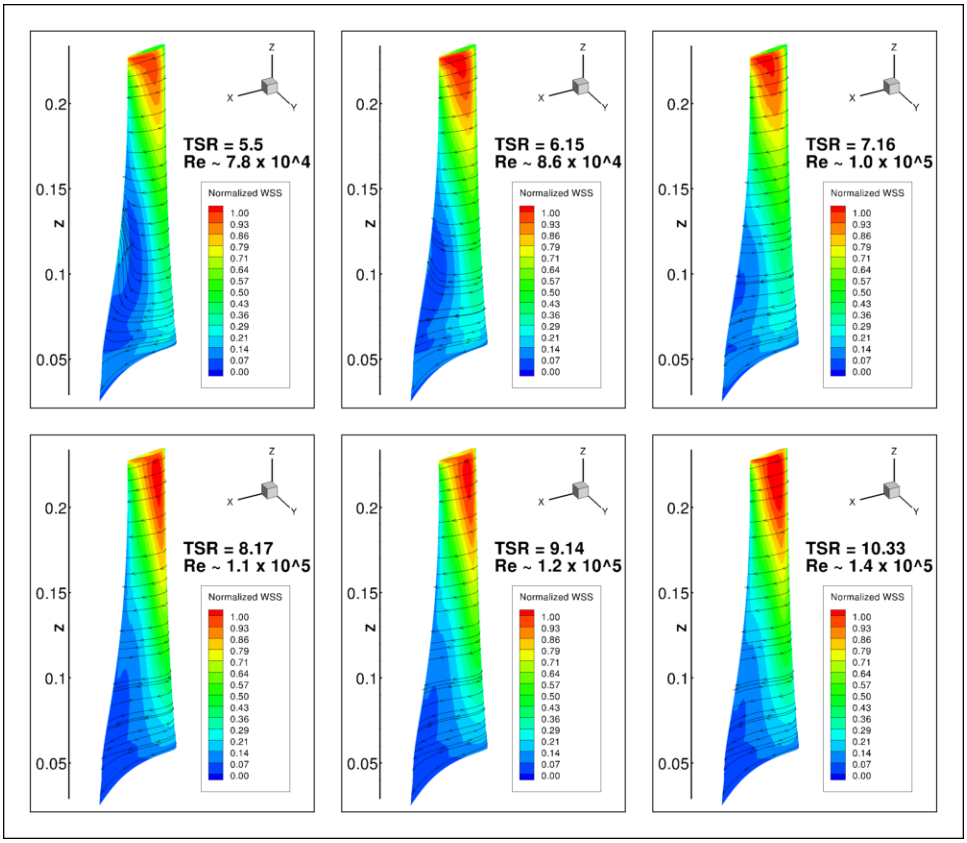

Figure 2.7: **Wall Shear Stress contours along the blade span superimposed by the limited streamlines (solid arrows) for various TSR and chord-based Reynolds number.**

2.3.2 Wake Recovery

The top and bottom plots shown in figure 2.8 represent the streamwise velocity contours normalized with the free stream velocity on a plane parallel to the flow direction, from left to right. As shown in these two velocity contours, flow decelerates as it approaches the turbine blades and the beginning of the turbine's nacelle (white region). The turbine extracts power from the incoming flow and generates a turbulent wake. Comparison between the SRF and BEM results reveals the similarities and differences

between these two numerical approaches. The top plot in figure 2.8 shows that the SRF captures the inhomogeneous flow field in the near wake region of the turbine ($\frac{y}{r} < 2D$) accurately. This inhomogeneity is apparent as two cyan blobs of decelerated flow near the blade tip and near the blade root. Furthermore, close to the blade tip, the shed vortices are captured via SRF in the form of a discrete set dark red circles. The bottom plot shows that BEM does not capture the details of the near wake region of the blade. The reason behind this limitation is that the BEM averages the hydrodynamic effect of the blade on the flow. As a result of this averaging, the inhomogeneity of the flow is smoothed out in this model. The deceleration region appears as a uniform region that starts as cyan close to the blade root and transitions to green toward the blade tip. The same process of azymuthal averaging of the hydrodynamic forces on the blade is the cause for the tip vortices not being captured by the BEM simulations.

Despite the above-mentioned differences, the far wake is consistent when modeled via the SRF and BEM approaches. The similarities in shape and magnitude of the velocity contours, visualized in figure 2.8, confirm this. For further quantitative comparison, figure 2.9 shows the velocity deficit profiles at different stations downstream of the rotor, simulated via SRF (blue) and BEM (red) and measured in experiment (black). Comparison between the numerical results from the two methods, shows that the velocity deficit predictions at 2D downstream are different over the majority of the blade span, with agreement starting close to the blade tip ($0.8 < \frac{z}{r} < 1$). It should be noted that this station is located exactly downstream of the tapered end of the nacelle, and the difference between treatment of this region in the computations affects the shape of the velocity deficit profiles near it. Comparison between the numerical and experimental results reveals that at 2D downstream, the profiles of velocity deficit from experiment (black) and SRF (blue) are in good agreement with each other. This is consistent with the comparison of measured vs predicted turbine coefficient of performance at $TSR \approx 7$, shown above. Furthermore, this agreement confirms the

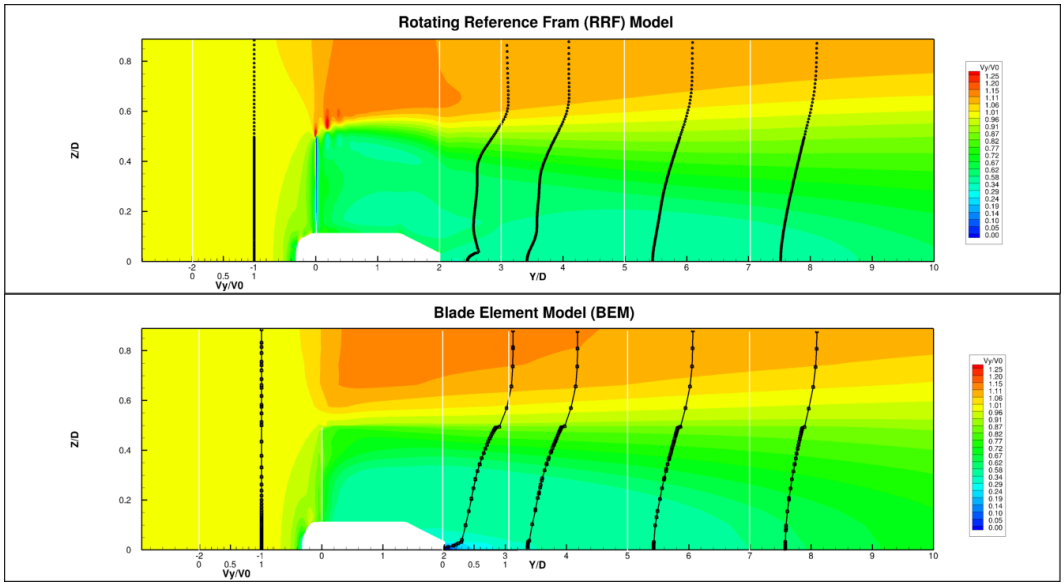

Figure 2.8: **Streamwise velocity contours, normalized with the free stream velocity, on a plane parallel to the free stream direction. RRF (top) and BEM (bottom) computational domains for a single turbine at TSR 7. Flow is from left to right.**

capability of the SRF model to capture the details of the flow field in turbine near wake region. The velocity deficit predicted by BEM (red) shows good agreement with the experimental data close to the blade tip ($0.6 < \frac{z}{r} < 1$). However, in the region close to the blade root, this agreement become poor and BEM overpredicts the deficit in the velocity.

At 3D downstream, the velocity deficit profiles predicted by SRF and BEM become closer. The influence of the nacelle and the separated region behind the blunt end loses importance in the overall wake and the velocity profiles ($0.6 < \frac{z}{r} < 1$) collapse on top of each other. Stations 5D and 7D downstream present good agreement between simulated velocity deficit profiles. The flow field and velocity deficit comparison between SRF and BEM in the far wake region of the turbine ($\frac{y}{r} > 3D$) showed

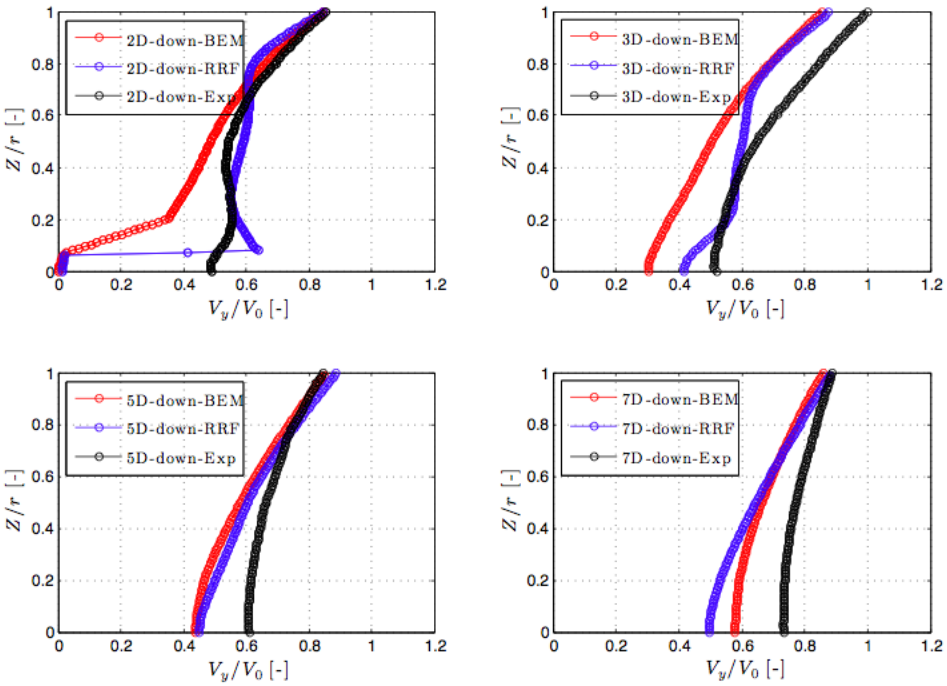

Figure 2.9: **Comparison between the measured (black) and simulated (blue and red) profiles of streamwise velocity, at various distances downstream of a single turbine at TSR=7.**

in figures 2.8 and 2.9 confirms that although BEM is limited in capturing the details of the flow field in the near wake region, it is capable of simulating the far wake region as accurately as SRF, with an order of magnitude lower numerical cost (in CPU time, memory needs and human operator time in creating the mesh of the domain).

Comparison between numerical and experimental results shows that starting from 3D and moving further downstream, the overall shape of the experimental and numerical velocity deficit profiles are similar, but the experimental velocity deficit recovers faster than the simulated velocity deficits. We hypothesize that, in the experiment, the presence of the nacelle and free-stream turbulence fluctuations enhances turbulent

mixing in the wake. It should be noted that the nacelle wall needs to be modeled as a free-slip surface in the SRF model and, due to this limitation, the turbulent boundary layer and its effect on the turbulent mixing process in the wake of the turbine are not well captured. The BEM is not limited in modeling the nacelle, hence, the effect of the nacelle in the mixing process in the near and far wake regions could potentially be captured more accurately than in the SRF. Despite the fact that the flow over the nacelle is represented more accurately by the BEM, however, averaging over the entire rotor disk makes the velocity deficit near the root poorly predicted and, as a result, the trend of the wake recovery in the near wake is not in good agreement with the experimental results.

The momentum deficit profile is used as a more dynamically meaningful metric to compare the numerical and experimental results. Momentum deficit profiles at different downstream stations, normalized by the free-stream momentum flux, are shown in figure 2.10 to quantify the net drag on the flow presented by the turbine rotor, and the complementary remaining momentum in the wake.

These momentum deficit profiles are integrated over the swept area of each blade section, at different stations downstream the turbine. The momentum deficit simulated via SRF (blue) and BEM (red) are in good agreement with each other. Despite the differences in the level of complexity of these two numerical models, they simulate the resultant momentum extraction by the turbine in a very similar fashion. On the other hand, both numerical models overpredict the momentum deficit at all stations downstream of the turbine compared to the experiments. We hypothesize that the enhanced mixing process due to the effect of the nacelle's wake and the high turbulence level in the experimental flow field, not modeled in the simulations, results in a faster wake recovery and lower momentum deficit in the experiments. Due to the flow field idealization and limitations of the numerical modeling, the effects of the above-mentioned phenomena are absent in the numerical results. The general trends of the normalized momentum deficit for the experimental and numerical results are

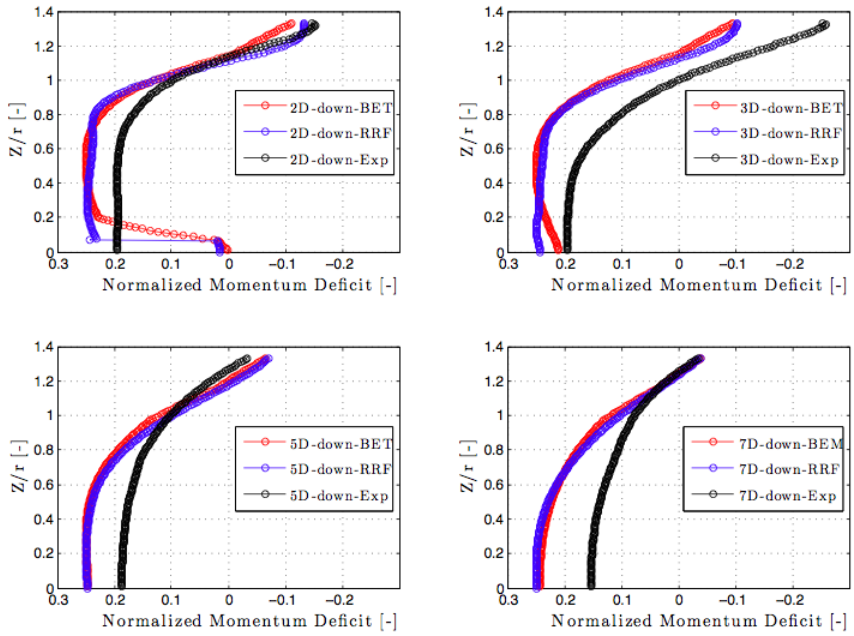

Figure 2.10: **Comparison of measured and predicted variation of the momentum deficit at various distances downstream of the rotor plane, for a single turbine at TSR=7.**

similar. The relative error in the simulations, defined with the discrepancy between experiments and simulations in the momentum deficit profiles as a metric, is of the order of 10% of the incoming momentum flux, compared to 20-30% error when based on the velocity deficit. This reveals that the simulations are capable of characterizing the wake of the turbine with acceptable level of accuracy.

2.4 Application of the Numerical Methodology to the full scale DOE RM1

2.4.1 DOE Reference Model 1

During the last decade, research and development in the field of marine renewable energy has suffered from the lack of a publicly available design for a reference MHK device (for example, a horizontal axis hydrokinetic turbine). As a result of this absence, different research groups designed in-house devices based on their problem of interest and availability of resources. This led to a patchwork of data on performance and wake of different MHK devices at different scales. The lack of open source data and comparable metrics represented an implied inefficiency in understanding the physics behind the operation of these devices and the discovery of the most important general issues behind these technologies.

Three years ago, the Department of Energy (DOE) put together an effort to design an open-source reference model for each MHK device type. An up-to-date, publicly-available CFD study on the proposed model for HAHT (DOE Reference Model 1, DOE RM1) [72] was published by Lawson et. al. [11] at NREL. In this section of the thesis, the developed numerical methodology described above will be applied to the performance and flow field simulation of the full scale DOE RM1. The numerical setup established for this full scale model is briefly discussed. The numerical simulations results are presented and explained. Last but not least, a comparison between the numerical results in this thesis and the results by Lawson [11] et al. is presented.

2.4.2 Numerical Setup

The Single Rotating Reference Frame (SRF) model was applied towards characterization of the full scale DOE RM1. The computational domain of the SRF simulations for the DOE RM1 is a half cylinder, due to the symmetry of the two-bladed rotor, 16.5 blade-radii in length and 6 blade-radii in diameter. The domain is divided into

three main blocks for meshing, as shown in figure 2.3. The volume upstream of the turbine is 2.5 radii long. The second block is where the actual geometry of the blade is located. This block also includes a number of auxiliary blocks that allow the creation of a high-resolution structured C-mesh around the blade. The high-resolution mesh near the blade wall provides an accurate solution that captures the turbulent boundary layer generated along the span of the blade, which is a key element in capturing the turbine wake. The third block, 14-radii long, is the volume downstream of the turbine, where the wake develops.

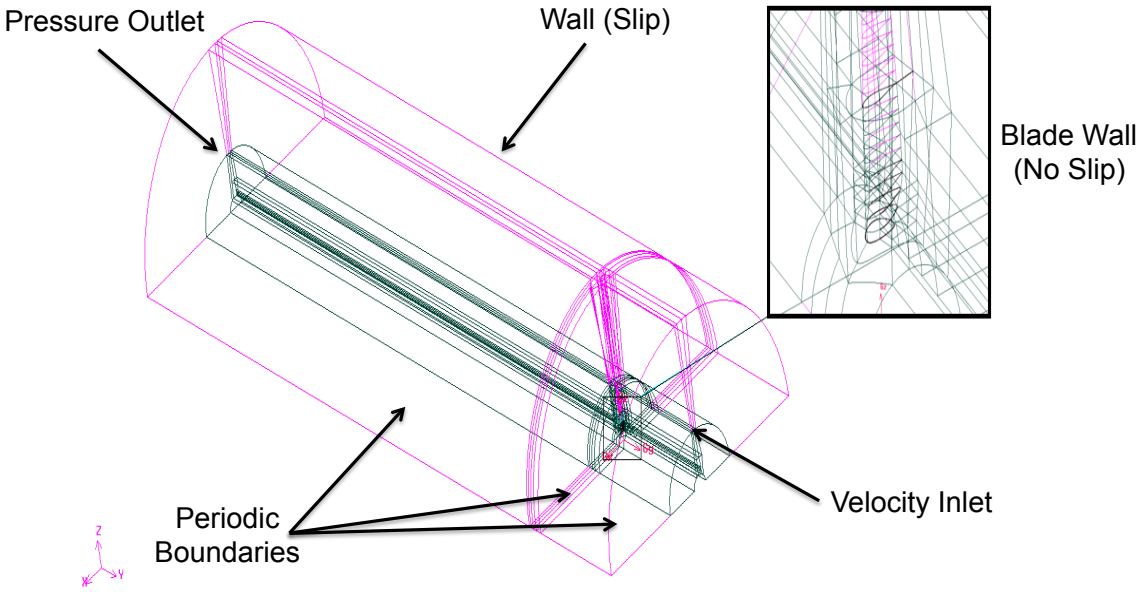

Figure 2.11: **SRF full computational domain with a zoomed-in view of the middle block including the actual geometry of the DOE Reference Model 1 blade.**

A close-up of the middle block section, needed due to the complex geometry around the blade surface, is also shown in figure 2.3 to highlight the details of the auxiliary blocks that allow the creation of a high-resolution structured C-mesh around the blade. This close-up shows how the hub is simplified to match the limitations of ax-

isymmetric boundary conditions imposed by the SRF model. The hub is represented by a stress-free cylindrical boundary that extends through the length of the domain. The blade geometry starts at the point where its cross section takes the shape of an airfoil, reducing the uncertainty about the blade root geometry and possible detached flow in the non-hydrodynamic sections of the blade root.

To successfully apply the previously developed and validated numerical methodology to the DOE RM1 turbine, similar to the previous SRF computational domain of the scaled-model turbine, the mesh elements were concentrated along the blade span and few chord lengths around it. This computational domain is discretized using only structured mesh and has about 10^7 mesh elements. generation of high and accurate mesh resolution around and along the blade span in the SRF domain would guarantee correct prediction of the turbulent boundary layer in these regions. Accuracy in capturing the flow field in these regions would result in accurate prediction of turbine's efficiency and wake structure. In this mesh the number of nodes around each airfoil section along the blade span is 220. The node distribution along the chord was not uniform. Each airfoil perimeter was segmented and the node distribution was was focused on the leading and trailing edges, adapting to the twist and taper of each section to generate a high quality structured mesh, specially around the fast-twisting root of the blade. The total number of nodes along the blade span is 153. In the radial direction of the C−mesh, 30 nodes were placed, with the first length at 1 mm from the blade wall. Similar to the mesh of scaled-model device this value of first length was calculated according to the chord-based Reynolds number and the guidelines provided in [18].

The boundary conditions of the SRF domain for the DOE RM1 turbine are exactly the same as the SRF computational domain for the scaled-model turbine. As shown in figure 2.11 the flow enters into the domain at inlet with a constant, uniform velocity from right and exits with a uniform pressure ($P = P_\infty$) from outlet on the far left. Cyclic-periodic boundaries are used on the symmetry plane (the half cylinder plane) of

the domain to simulate blade rotation. The domain's top cylindrical wall is modeled with a shear-free wall boundary condition (no stress in the tangential directions and no flow-through in the normal direction) to avoid increasing the blockage effect artificially in this high Reynolds number flow.

2.4.3 Results

3D Lift and Drag Coefficients

As mentioned above, the blade's span is divided into sections to calculate the 3D lift and drag forces/coefficients along the blade. The details of the post-processing was discussed in section 2.1.4. In this section, the results obtained for the 3D coefficients at different angles of attack are presented and discussed.

Figure 2.12 shows the values of angles of attack (AOA) (in black on the left y-axis) as well as lift and drag coefficient (right y-axis) along the blade span (x-axis). In this figure, AOAs are monotonically decreasing moving from root to tip. This is due to a combination of the increase in rotational velocity with radial distance (eq. 2.5) and the design twist angle distribution for the blade. The lift coefficient is shown in green: for the range of AOAs sampled on the blade at this TSR, lift decreases towards the tip of the blade. Noticeable here is a rapid decrease in the coefficient of lift at the region close to the blade tip. This rapid change is caused by the vortical flow that leads to the formation and shedding of tip vortices, reducing the pressure coefficients near the blade tip. Drag coefficient is shown in red: drag coefficient slowly decreases from the root to the tip, in parallel to the decrease in the value of AOA.

The values near the blade root show fast decrease of lift and increase of drag over a short section (from $r = 3.55\ m$ to the simulated blade root). Figure 2.13 shows the streamlines along the blade span superimposed on the pressure contours on the suction side of the DOE RM 1 blade. As seen in this figure, the flow is attached to the blade from the blade tip till $r = 3.55\ m$. From this point to the root, flow starts to

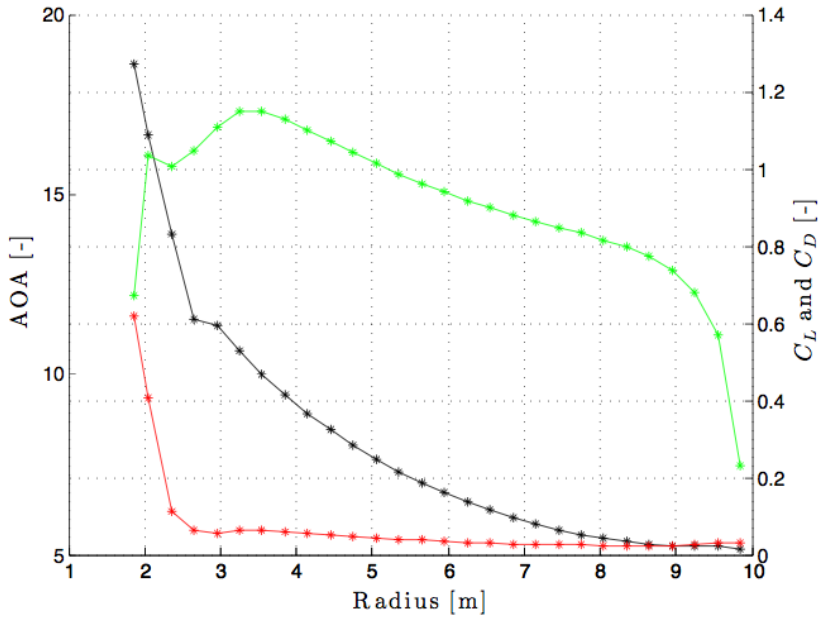

Figure 2.12: **Calculated AOA (black), 3D lift (green) and drag (red) coefficients along the DOE Ref. Model 1 blade span (TSR=6.3 and Re** $\approx 10^6$).

become separated. It can be hypothesized that this unsteady, separated flow region that expands toward the root is the reason behind the rapid decay in performance, with low lift coefficients and high values of AOAs and drag coefficients (figure 2.12). Further investigation, shows that this separation is not only due to the naturally-occurring large value of AOAs (due to the small tangential velocity component), it is also due to the shape of the airfoil sections close to the root. After $r = 3.55\ m$, the blade cross-section has an elliptical shape where the flow at large AOA quickly separates. It should also be noted that the data on the very last section of the root is not realistic. This blade section results from the limitation of the SRF model of axisymmetric boundary conditions. In order to be able to exclude the hub section from the computational domain and create the arc section showed in figure 2.3, the

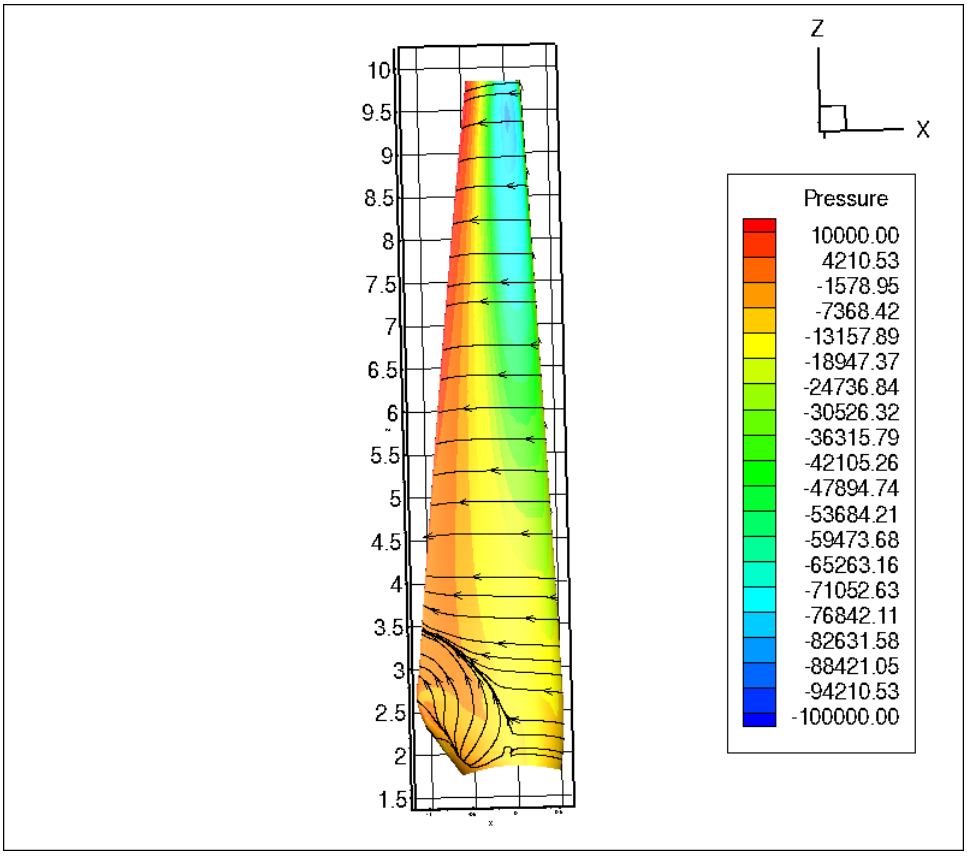

Figure 2.13: **Superimposed streamlines on the pressure contours along the suction side of the blade (TSR=6.3 and Re** $\approx 10^6$).

very last blade section has to be truncated and projected on the arc. The shape of this section becomes skewed and the AOA, lift and drag coefficients computed are not realistic.

Observation of this separated region by visualization of the streamlines also clarifies the stiffness in the convergence of the numerical simulation observed for these conditions. The steady RANS simulation is not able to capture this unsteady, separated flow. Therefore, it causes slower convergence, and appears noisy in the numerical results, for example as fluctuating values of lift and drag coefficients on this region of the blade span. It should be noted that, since the long term goal of this research is

blade performance and far wake characterization of this turbine, the separated flow in the blade root is not a region of interest. The complex fluid dynamics in this region might be interesting for other types of studies and can be addressed using an unsteady RANS simulation or a higher fidelity numerical model (LES, ...). However, since the contribution of this region to the overall power extraction from the flow is minimal and the generated unsteadiness will diffuse less than 1 radius downstream into the flow, we can exclude this section of the blade from our computational domain.

According to the discussion above, the first three sections close to the root ($r = 1.85$ *to* $2.65\ m$) were excluded from the computational domain. This was done to remove the source of numerical instability in our simulations due to the unsteady, separated flow and to reduce the uncertainty in the numerical results. Figure 2.14 shows the AOA, lift and drag coefficients calculated from the blade without the root section compared against the corresponding results with the blade that had the root section. AOA (in black and blue), lift and drag (in red and green) coefficients are in good agreement at the sections from the tip to the radial position of $r = 4\ m$. However, from this radial position to the root of the blade, the disagreement between the two simulations becomes more significant, specially in the lift coefficient.

To investigate the disagreement between the values of lift and drag coefficients more precisely, figure 2.15 shows the visualization of the streamlines along the blade span after excluding the root section. The flow is attached almost everywhere along the blade span. It is interesting to note that the flow is not separated on the sections between $r = 3\ m$ to $r = 3.5\ m$. When the elliptically-shaped sections of the root ($r = 1.85$ to $2.65\ m$) were included in the model, the flow in those intermediate root sections ($r = 3\ m$ to $r = 3.5\ m$) was detached, despite their aerodynamic shape (figure 2.13). This means that the highly separated unsteady flow close to the root was also affecting the sections above it. Unfortunately, there is no other publicly available data to confirm the accuracy of the simulation of the flow field behavior in this region.

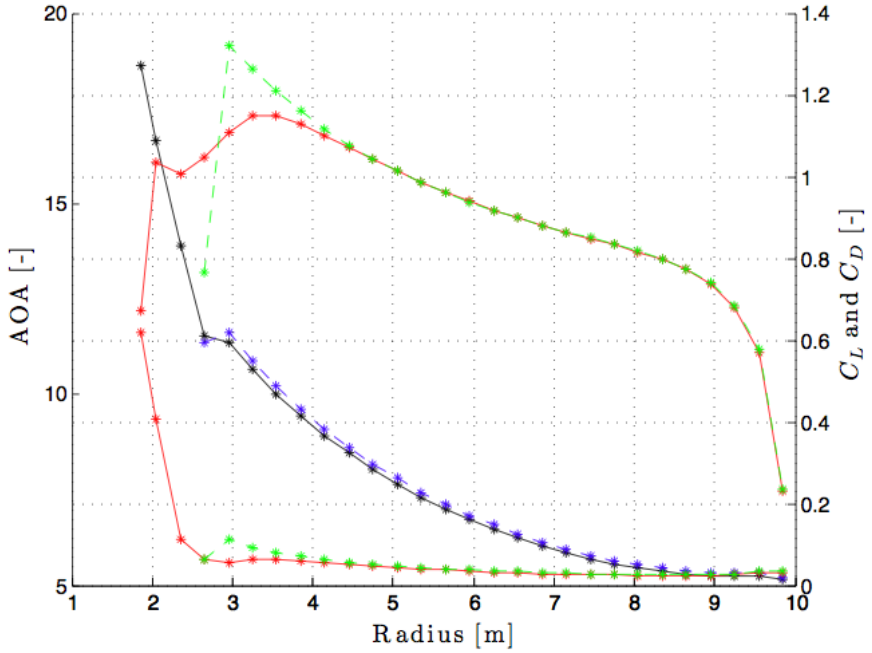

Figure 2.14: **Calculated AOA, 3D lift and drag coefficients along DOE Ref. Model 1 blade span without first three sections at the root (TSR=6.3 and Re** $\approx 10^6$).

Figure 2.16 shows the comparison between the sectional extracted power per unit chord length. Results from simulations including the root are plotted in red, and simulations without the root are in green. This comparison shows that for most the blade span, the results are unaffected by the changes in the model, and excluding the three elliptical sections at the root affects the overall power extracted by the blade by less than 3%. Considering the uncertainties inherent in this complex RANS model of the turbine, and the presence of unsteady separated flow in one of the simulations, this difference in power is negligible. Thus, excluding the root sections is a net improvement of the numerical model and the accuracy of the simulated far wake.

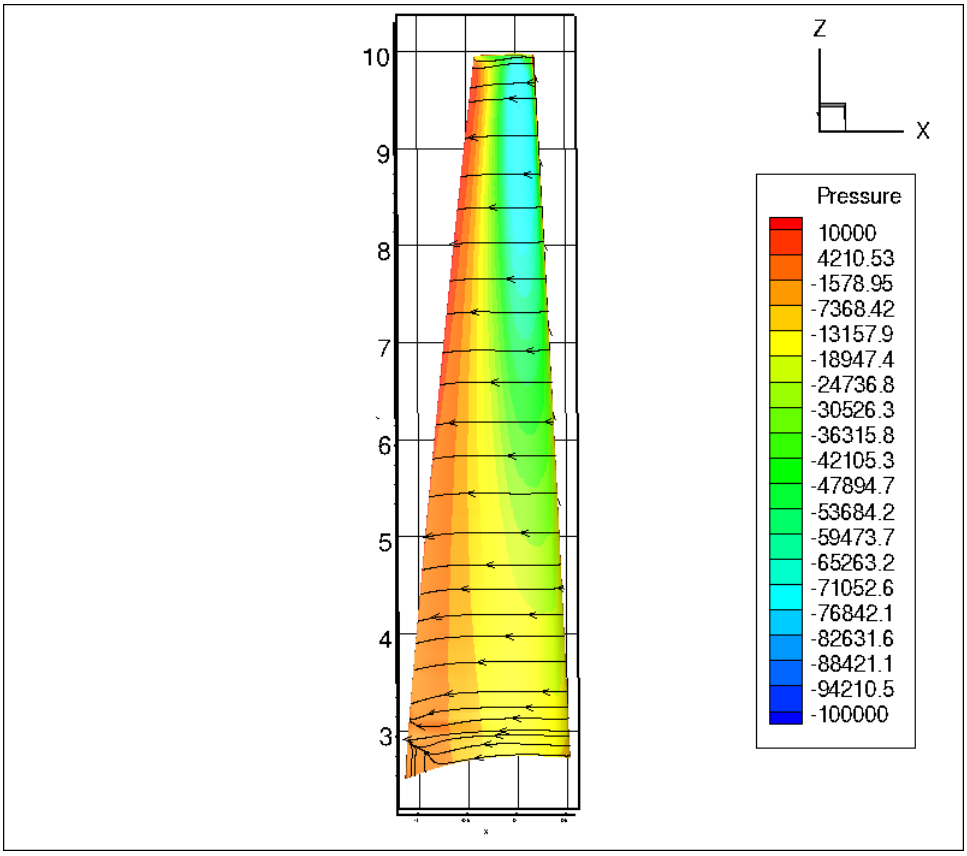

Figure 2.15: **Superimposed streamlines on the pressure contours along the suction side of the blade without root sections (TSR=6.3 and Re** $\approx 10^6$).

The Flow Field

Figure 2.17 shows the streamwise velocity contours normalized with the undisturbed free stream velocity. These contours are plotted on xz planes perpendicular to the flow direction along the computational domain. The sequence of these planes starts upstream of the turbine, $\frac{y}{r} = -0.25$ (left corner top), and moves downstream, $\frac{y}{r} = 2.5$ (right corner bottom). As shown by the evolution of the velocity contours, the flow starts to decelerate as the presence of the turbine rotor is felt through pressure changes. At the location of the blade, $\frac{y}{r} = 0$, acceleration of the flow on the suction side of the blade and deceleration on the pressure side are observed. Another

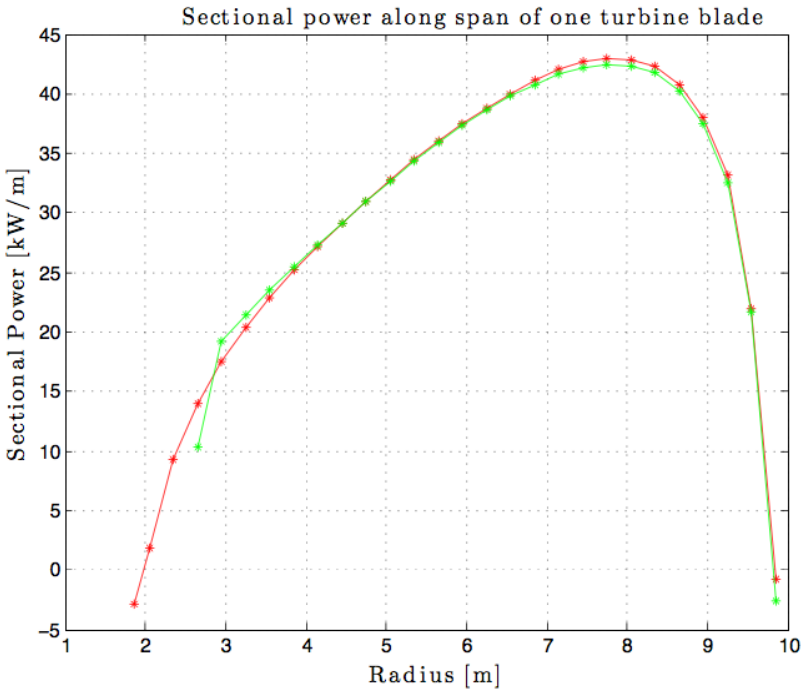

Figure 2.16: **Comparison of power extracted per unit length along the blade span for the blade including the root (red), against the blade without the root (green).**

phenomenon shown at $\frac{y}{r} = 0$ is the high velocity "leaking" from the suction side to the pressure side, associated with blade tip vortex shedding. Since the tangential velocity at the tip of the blade reaches its maximum value, the vector summation of the axial and tangential velocity components will result in a region of high velocity and low pressure. This flow acceleration is seen as a high velocity region spilling from the suction side of the blade over the tip in a counter rotating motion with respect to the blade rotation. Moving further downstream, the tip vortex diffuses into the flow, becomes weaker and disappears. As the distance downstream from the turbine increases, the velocity contour in the wake becomes more homogeneous. At about

1.5 radii downstream of the blade, the turbulent wake becomes axisymmetric. Observation of the axial symmetry of the flow in the wake only a few diameters (1-2) downstream of the rotor justifies the use of less computationally intensive models such as BEM, which reproduce the flow field around the turbine and in the wake as axisymmetric, maintaining the integral values that characterize the turbine performance (thrust, torque and power) with good accuracy and at a much lower computational cost.

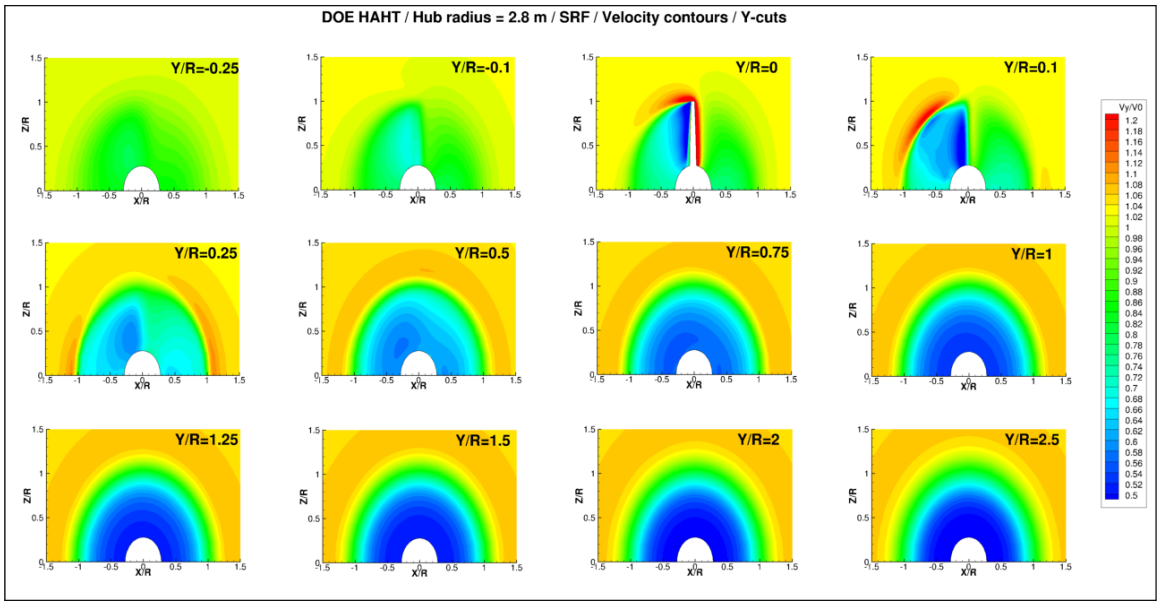

Figure 2.17: **Normalized streamwise velocity contours on the Y-cuts plane along channel.**

2.4.4 Far Wake

To visualize the wake of the DOE RM 1 turbine, figure 2.18 shows the streamwise velocity contours normalized with the free stream velocity on a yz plane (parallel to the free stream direction) in the middle of the channel. Superimposed with the contours, velocity profiles along $y = constant$ lines (perpendicular to the flow direction)

show the velocity deficit at different distances downstream of the rotor plane. The flow starts to decelerate as it approaches the rotor plane. Right behind the blades, in the near wake region, the flow becomes highly inhomogeneous and dominated by vorticity shed from the rotor and hub region. This type of detail in the physics of the wake can be simulated by the SRF model, but not the BEM. Further downstream, the turbulent wake starts to become smooth. An interesting observation from this figure is that the corkscrew vortex shedding from the tip is captured by the SRF model, and made visible in the form of small, discrete high-speed blobs near the tip of the blade, corresponding to the high velocity in the core of the vortex. The vortex core is stronger closer to the blade, and gets weaker as it develops. At about one radius downstream (the tip speed ratio is close to the value 2π at which the helical step of the tip vortex is exactly one radius per revolution), the vorticity has diffused substantially and in another helical step, eventually disappears.

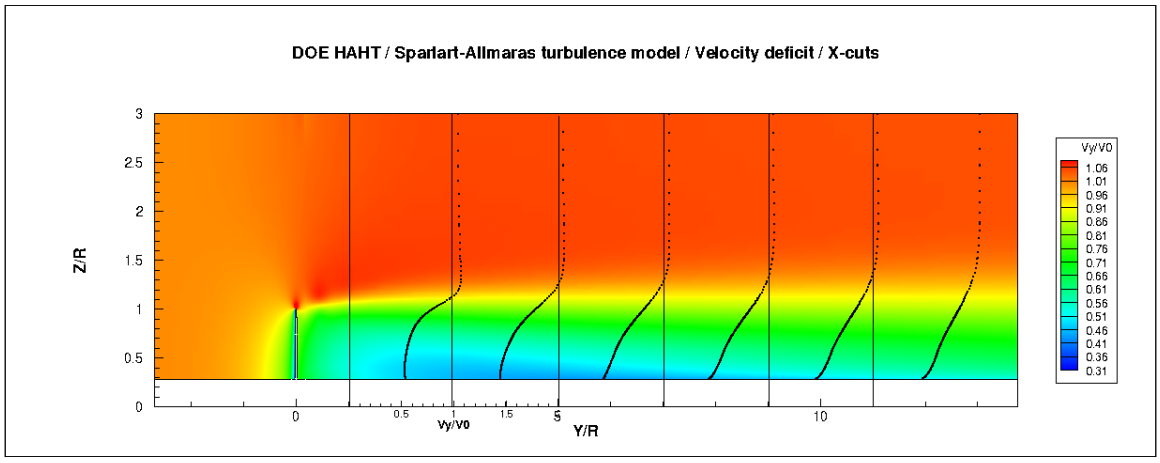

Figure 2.18: **Velocity contours in the turbulent wake simulated via the SRF model using Spalart Allmaras turbulence model.**

2.5 Validation/Comparison of the Numerical Results and Methodology

2.5.1 Numerical Comparison

Since the DOE Reference Model 1 is a newly developed reference model, there are not lot of publicly available data about this blade design. In order to build more confidence in our numerical results, we compare them against results by Lawson et al [11]. To make a precise comparison, the operating conditions (TSR, turbulent intensity and working fluid), numerical settings (turbulence model and numerical schemes) and number of grid elements from the two simulations were matched. Qualitative and quantitative comparisons are presented in this section.

Table 2.2 shows the most relevant differences between the two numerical approaches. This table shows that the difference between the values of torque on one blade of the DOE RM 1 reported by Lawson et al. and the numerical results in this thesis is less than 1.5%. Considering the exclusion of a small section of the root (about 50 cm) and the turbine nacelle in our model and also the differences between the two numerical simulations such as using two different numerical solvers, mesh structures and element types, this error is not significant. Despite the good agreement between values of torque computed by the two approaches, there are some significant differences in the simulated velocity field. Figures 2.19 and 2.20 show results from Lawson et al. (top) and this thesis (bottom). The streamwise velocity of the flow, going from left to right, shows differences in smoothness of the velocity contours upstream of the blade. In Lawson et al., the velocity contours have a skewed shape as the flow approaches the turbine blade, while the simulation in this work presents contours that smoothly decelerate and make a transition from yellow to blue color. The flow field behavior at the tip of the blade, where the vector summation of the free stream and rotational velocity components is maximum, is similar in both figures. The shed tip vortex is captured and made visible as a single high velocity contour. However, the simulation in this thesis shows sinusoidal features in the contours that mark the shear

Table 2.2: **Comparison between settings and results of two steady state simulations at the NREL and NNMREC to numerically model the DOE RM 1 HAHT.**

Research Group	NREL	NNMREC
Numerical Solver	STAR CCM+	FLUENT 12.0
Mesh Structure	Unstructured	Structured
Number of Grid Elements	11.5×10^6	11.1×10^6
Element type	Polyhedral	Brick
Torque [N-m]	2.13×10^5	2.16×10^5
Relative Difference [%]		1.41

layer starting from the tip, which are not observable in Lawson et al. These trends confirm the existence of coherent vortical structures in the near wake region.

The flow field in the root region of the blade shows differences motivated by the inclusion of the nacelle by Lawson et al. in their computational domain. As explained above, the computational domain in this thesis was simplified by excluding the nacelle and also the first two sections of the blade root. It seems that the secondary flow due to the aerodynamic shape of the nacelle, included in Lawson et al., reduces the streamwise velocity component near the blade root. This flow leads to decrease in AOA and hence reduction of flow separation at the blade root. The unsteady behavior in this region is captured well by Lawson et al., which shows a region of flow acceleration behind the nacelle, as opposed to the unphysical flow deceleration shown in the preliminary simulations including the root (but not the nacelle) in this thesis.

The velocity field in the far wake region shows some differences. Lawson et al. shows a small decelerated region near the middle of the wake region. The authors

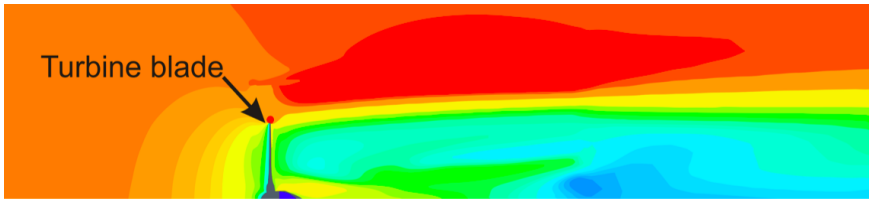

Figure 2.19: **Streamwise velocity contours in the turbulent wake simulated in NREL [11].**

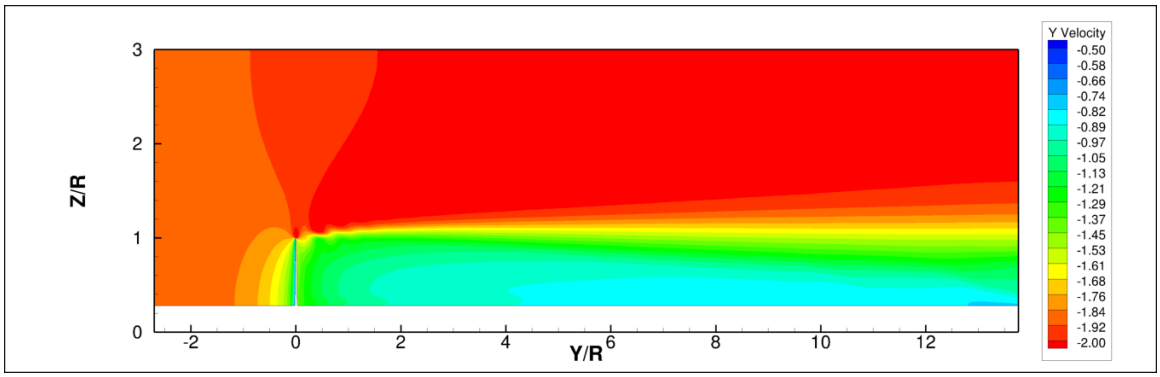

Figure 2.20: **Streamwise velocity contours in the turbulent wake simulated in NNMREC.**

mentioned in their paper that they judged the convergence of the simulations based on the residual of the torque along the blade and monotonic decrease in the other residuals (i.e. mass and velocity) by three order of magnitude (i.e. 10^{-3}). Based on our experience with these types of simulations, conditions on the convergence of residuals are necessary but not sufficient. These simulations need to run for a certain number of blade rotations to fully converge. The confirmation for this is that the regions of spurious flow resulting from the blade start-up process and step-by-step increment of the inlet and rotational velocity in the computations (to avoid divergence in teh SRF simulations) will be convected out of the computational domain, with a corresponding decrease in the residuals.

In order to confirm this hypothesis figure 2.21 shows simulation results, from this thesis, converged according to stated convergence criteria by Lawson et. al.. As visualized in figure 2.21 there are two decelerated regions (dark blue) in the wake. These regions are the above-mentioned spurious flow resulting from the blade start-up process and the gradual increment of inlet and rotational velocity magnitude to avoid divergence in the SRF simulations. Once this simulation is run for a certain number of blade rotations, these two regions of spurious flow will be convected out of the computational domain. The final and fully converged results will be the same as the result showed in figure 2.20. However, it should be pointed out that the existence of this decelerated regions in the domain does not critically affect the flow field around the blade, as proven by the consistency of the computed torque values.

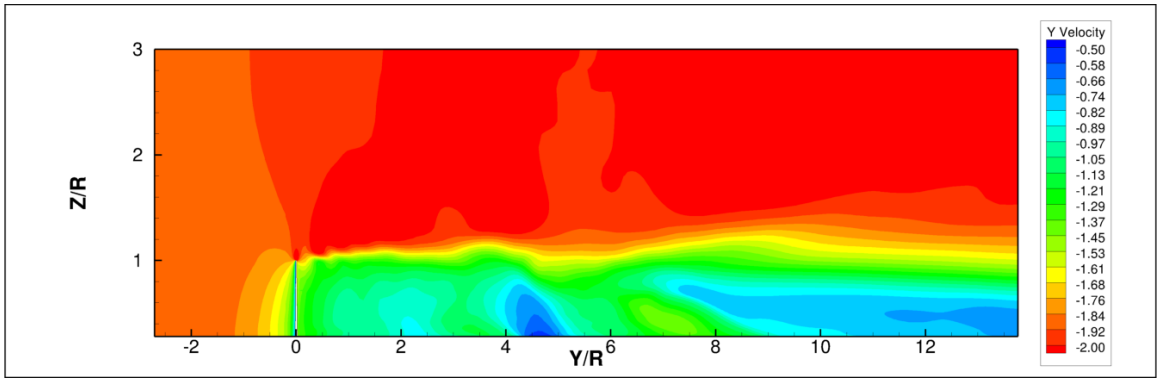

Figure 2.21: **Streamwise velocity contours, not fully converged, in the turbulent wake simulated in NNMREC.**

The last difference to point out between the simulated velocity field of Lawson et al. and the simulation in this thesis, appears in the wake near the outer boundary. Closer to the outer cylindrical boundary, the flow in Lawson et al. can be observed to slightly decelerate (slight transition from dark red to orange). In this thesis, however, the free stream velocity region persists downstream all the way to the end of the domain. This slight difference is assumed to be due to the boundary condition applied to the outer

boundary of the computational domain. Lawson et al. applies a symmetry boundary condition in that region whereas the simulations in this thesis applied a shear-free wall, with no flow out. Due to the symmetry boundary condition, the rotational velocity that is decaying from the tip of the blade outwards has to be locally conserved, forcing a slight deceleration of the streamwise velocity to conserve kinetic locally, and this is observable as a weak pattern in this region.

In conclusion, the general flow fields around and in the wake of the DOE RM1 blade from the two simulations are similar. It seems that the difference in the near wake region is due to the geometry simplification used in this thesis (by excluding the nacelle and root sections) and possibly to differences in the method for capturing the turbulent boundary layer on the blade. Differences in the far wake region can be attributed to small differences in the boundary conditions and the length of computational time used *after* the residuals appear to have converged, to allow for the spurious flow features generated, due to blade start-up and the gradual increment of inlet and rotational velocity magnitude till reaching the desired operating conditions, to convect out of the large computational domain necessary to model the far wake.

Chapter 3

HAHTS ARRAY CHARACTERIZATION: METHODOLOGY DEVELOPMENT, EXPERIMENTAL VALIDATION AND APPLICATION

Hydrokinetic turbines, similarly to wind turbines, should be placed in the form of an array to have the potential for electricity production necessary to connect to the electrical grid and feed it at a commercial scale. Due to the confined nature of tidal sites, however, the spacing of turbines in an array of HAHTs is much more critical to the energy production and economic viability of the turbine farm than in wind energy installations, and needs to be highly optimized. This optimization process must maximize the efficiency of power generation while minimizing the capital cost of the infrastructure, the potential environmental effects of the array and the fatigue load on the turbines' structure. The initial step to perform this optimization process is to understand the flow field in the array and how the devices perform while interacting with this complex velocity field. This initial step also provides an in-depth understanding of the potential constraints for the array optimization process. A numerical methodology can then be developed to model the essential physics of the flow field needed for the array computations, in an time-efficient way compatible with the optimization of turbine array performance. This numerical methodology can be used to examine the effect of various constraints in this optimization process, such as the number of turbines per surface area, the number of turbine rows, ...

In this chapter, the Blade Element Model (BEM), described in detail in Section 2.1.2 in the context of the characterization of a single HAHT, is used for the flow field simulation in an array of turbines. At this stage, the capabilities and lim-

itations of the BEM have been laid out in Chapter 2, therefore, only the specifics of the computational domain for simulation of turbine arrays is described.

The BEM of several turbines in different spatial configurations and operating at different set points is implemented to match experimental conditions in two- and three-turbine arrays in a research flume. The goal of this process is to validate the application of the BEM model to turbine wake and performance characterization in an array. After understanding the capabilities of the BEM for simulation of HAHT small arrays from the experimental validation, the most important spacing variables in the process of array optimization are proposed and numerically investigated. Drawing a general picture of the effect of different constraints and understanding the underlying physics in the array optimization process, a general numerical methodology for array optimization of HAHTs is developed. The simplifications made to narrow down the path for array optimization are explained in detail and their validity and impact on the computations of array efficiency are evaluated a posteriori. This methodology can be used for detailed turbine array optimization based on the specific range of the variables and constraints (i.e. dimensions of the tidal channel, number of allowed turbines in rows or columns in an array, etc.) using a minimum of computational cost and time.

An important point to highlight at the beginning of this chapter is the definition of the turbine efficiency used throughout this chapter. The first definition is the "global efficiency" which is defined as the ratio of the power extracted by turbine to the available kinetic energy flux in the free stream. The second definition is the "local efficiency" that is defined as the ratio of the power extracted by turbine to the available kinetic energy flux in a specific distance upstream of the turbine rotor plane. These two definitions of the turbine efficiency were used according to the requirements for performed comparisons and methodology development in this study. In each section it has been clearly mentioned the type of the definition used and the reasons and thoughts behind the choice.

3.1 Development of the Numerical Methodology for HAHT Array Simulation and Experimental Validation

3.1.1 Numerical Setup

BEM was used to model the presence of the turbines in the flow field and to predict their performance in an array. The key aspect of BEM that makes it optimal for this study is that it simulates the hydrodynamic effect of the turbine on the flow field without the need to mesh the actual geometry of the blade and without limitations in the domain boundary conditions. By eliminating the blade geometry, this rotor representation reduces the mesh cell count and the required time for creating the mesh 10 and 100 times with respect to blade-resolving methods.

BEM allows the creation of multiple rotor zones in the computational domain that can be turned on and off in different simulations, with the possibility of different turbine array configurations using the same mesh. Enabling those rotor zones that are part of the array of interest, and treating the rest as fluid regions that are part of the fluid domain, a parametric study of multiple turbines with different spacing can be conducted with a fixed mesh. The implementation of the BEM in the RANS solver used in this thesis is limited to ten turbine rotors in the domain and twenty blade elements per rotor.

As discussed thoroughly in Section 2.3.2 of this thesis, BEM is limited in its ability to capture the details of the flow field in the near wake region. This limitation is caused by the averaging across the entire rotor swept area of the hydrodynamic forces exerted by the turbine blades. Despite its limitations in capturing the non-axisymmetric flow field in the near wake, BEM does resolve the far wake region with comparable accuracy as higher fidelity numerical models [18, 23]. The far wake plays a dominant role in array optimization, as it determines the impact of upstream wakes on downstream turbines. BEM is thus the appropriate model for array optimization, based on the balance of fidelity to the dominant physics and computational turn-around.

The specifications of the numerical settings, boundary conditions and mesh resolutions for each turbine in the turbine array computational domain of a turbine array are exactly the same as the corresponding numerical setup for a single turbine explained in Section 2.2.2. These numerical settings have been previously validated experimentally in the simulation of a single HAHT. The only difference between the computational domain of a single turbine and that of an array of turbines is the additional rotor zones created along the length of the computational domain. The details of the methodology used to develop the computational domain for the simulation of multiple array configurations are given in the next two subsections.

Two Coaxial Turbines with Variable Spacing

As explained above, the computational domain for the investigation of turbine arrays was developed in a manner that enabled all the array configurations to be simulated using the same computational domain. This method provides the advantage of having identical boundary conditions and mesh resolution for all of the case studies. Figure 3.1 shows a full view of the computational domain used for simulation of arrays of two coaxial turbines with different downstream spacings. As shown in figure 3.1, all the possible positions of the nacelle and rotor of the downstream turbine are included, highlighted in gray, in the domain.

The inlet boundary condition is set to constant velocity and the outlet conditions is set to hydrostatic pressure. The sides of the prismatic domain are set as free-shear walls. As explained in Section 2.2.2, the spacing of these walls from the rotors are set to match the 20% blockage ratio in the experimental setup. The computational domain showed in figure 3.1 is meshed with approximately 1.9 million elements. The mesh is structured in most of this computational domain, similarly to the computational domain for a single turbine, except for small regions upstream of each turbine, in front of the nacelle's curved head, and in the wake of the each turbine, right behind the tapered section of the nacelle. In these sections, unstructured tetrahedral elements

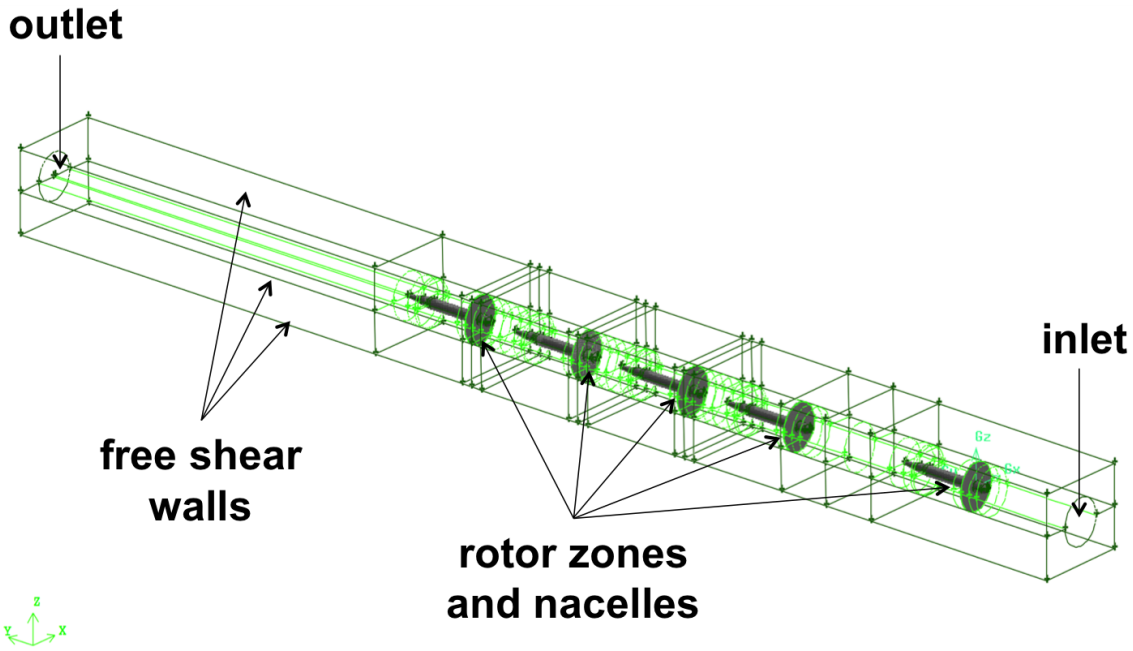

Figure 3.1: **Computational domain for modeling two-coaxial-turbine arrays with different spacings.**

were used to fill in the transition region between two regions of structured mesh in the domain. Figure 3.2 shows a zoomed-in view of the full computational domain (showed in figure 3.1). The first three rotor zones and their nacelles are clearly visible in the figure, highlighted in gray.

As an example, figure 3.2 shows the simulation of two turbines located coaxially with a spacing of 5 diameters (5D). The two first turbine rotors are activated as Blade Element body-force regions (circular gray areas in the figures) and their nacelles are set to a no-slip boundary condition. The rest of the rotor zones are defined as interior fluid zones, thus no turbine effect will be exerted on these zones. When 8D spacing is studied, the first and third turbines, in figure 3.2 are activated as rotor zones while all others are set to interior fluid zones. With this methodology, multiple downstream

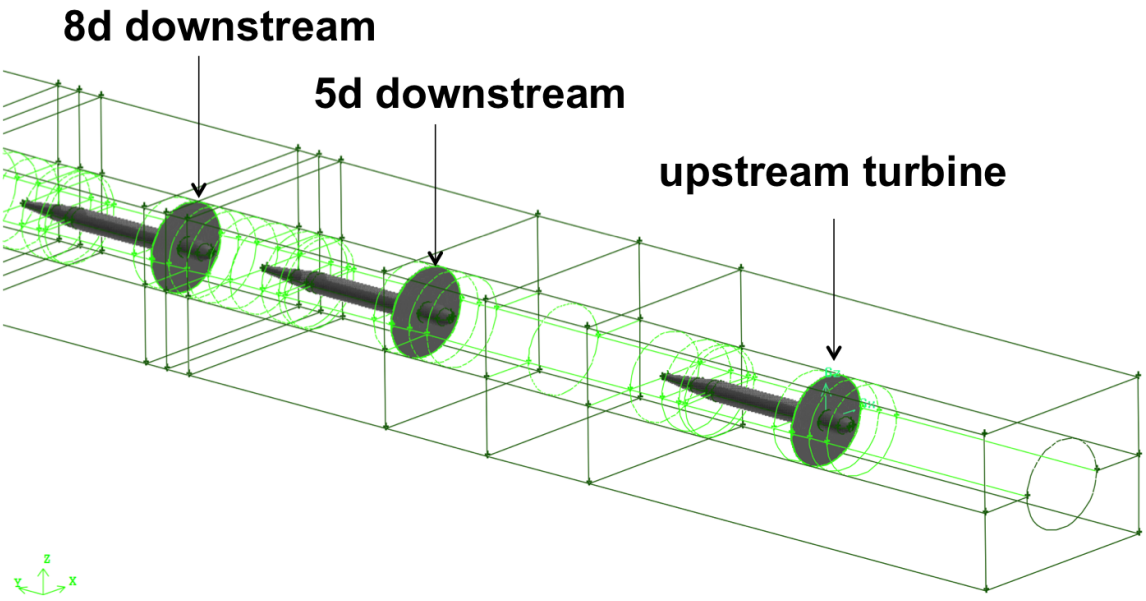

Figure 3.2: **Zoomed-in view of the computational domain for modeling different two-turbine coaxial arrays with different spacing.**

spacing for the two-turbine array can be modeled keeping the same mesh on the same computational domain.

Three Coaxial Turbines

Three coaxial turbines at 5D spacing between consecutive rows are modeled and compared against experimental results. The computational domain, boundary conditions, and mesh resolution for this simulation are set according to the study of the two-coaxial-turbine array presented above.

3.1.2 Experimental Setup

Experimental measurements of performance and wake velocity profiles in different HAHT array configurations were collected by a previous MSc student at the Univer-

sity of Washington's NNMREC [17]. Three different configurations were studied: 1) Two coaxial turbines with variable spacing (5D, 8D, 11D and 14D), 2) Three coaxial turbines with two different spacings, 5D and 7D, and 3) Three turbines with 0.25D lateral offset and two different downstream spacings (5D and 7D). The details of the experimental setup were presented in Section 2.2.1 of this thesis.

Two Coaxial Turbines at Different Downstream Spacing

Figure 3.3 shows a schematic of the four array configurations studied experimentally. The spacing between turbines is set at 5, 8, 11 or 14 turbine diameters to investigate the role of downstream distance on wake recovery and performance of the devices in a coaxial configuration. Rotational speed and torque on the turbine's shaft were experimentally measured. The resulting coefficient of power as a function of Tip Speed Ratio is compared with the simulation results. The wake velocity profile, measured by Particle Image Velocimetry (PIV) at different locations downstream of the turbines, are compared against that predicted by the RANS simulation.

Three Coaxial Turbines

A configuration with three coaxial turbines spaced by 5D and 7D between consecutive rows was also studied experimentally. PIV measurements of the velocity profile across the wakes and angular velocity and torque at the shaft of the three turbines were collected. The results from the 5D case are compared against the simulation results. The key concept to investigate in this study is effect of the two upstream devices on the performance of the third downstream device operating under a wide range of TSR values.

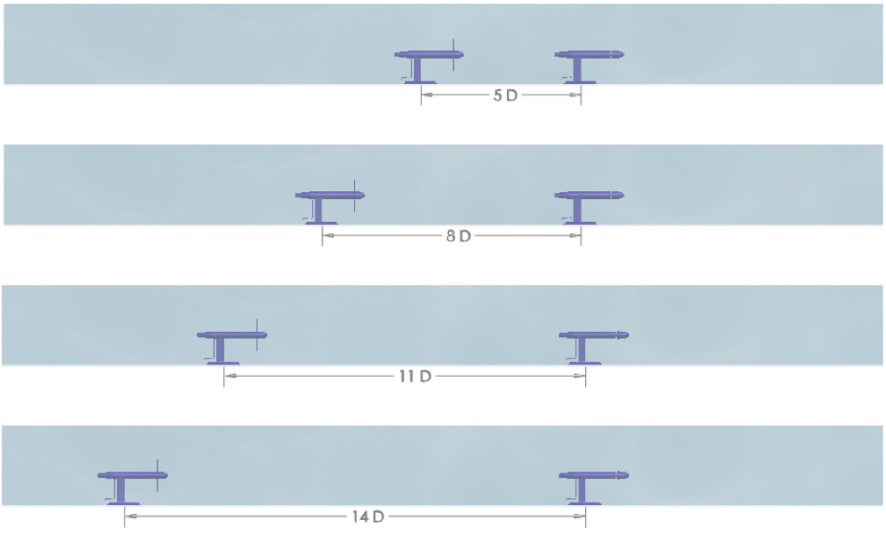

Figure 3.3: **Schematic of two coaxial turbines at different downstream spacing (5D, 8D, 11D and 14D).**

3.1.3 Results

Before the presentation of numerical and experimental results for turbines' performance in a turbine array, an important point regarding the methodology to match the turbines' Tip Speed Ratio (TSR) in the numerical simulations with the corresponding experimental value needs to be clarified: the angular velocity of each turbine in the experiment is set and kept approximately constant using a magnetic particle brake. The goal of the control process is that each turbine operates under a certain value of the TSR, measured a posteriori when the velocity profile upstream of the rotor is determined. The method to set the angular velocity in the current numerical simulations is necessarily different to match the TSR values for which experimental data is available. In the BEM, the value of turbine's angular velocity is a constant input into the model. Since the incoming velocity is unknown until the simulation runs for a significant number of iterations, the magnitude of the angular velocity of the downstream turbines needs to be tuned after the flow field has been shaped by a sufficient

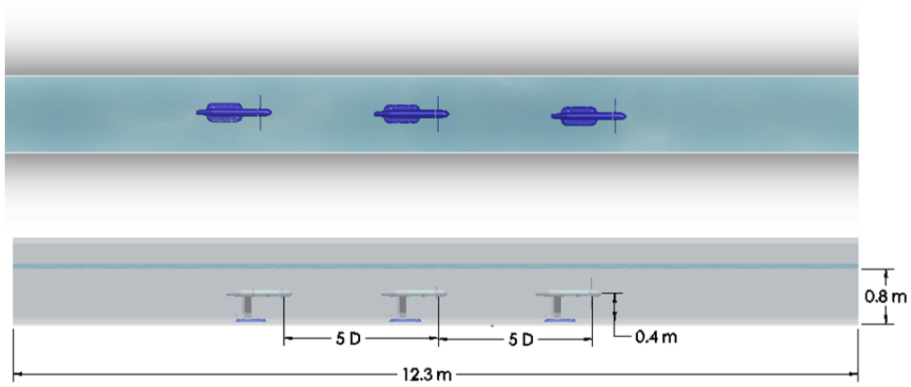

Figure 3.4: **Schematic of a three-turbine coaxial array. The three turbines are located coaxially and spaced at 5 turbine diameters between consecutive rows.**

number of iterations. This tuning process is necessary to respond to the evolution of the velocity distribution incoming into each turbine rotor, to match the TSR in the simulations with the corresponding experimental values. The velocity magnitude on a plane 2D upstream of the turbine rotor is averaged, and this value is used to find the desired angular velocity to match the experimental TSR. This process can be repeated one or two times until the value of the averaged velocity on the plane 2D upstream the turbine does not change anymore. Note that the distance of 2D upstream was determined as the minimum distance from the rotor plane where the induction effect of the turbine is not felt by the incoming free stream velocity.

Another important point to highlight here is the definition of the turbine efficiency used in both numerical and experimental results. In both analysis (numerical and experimental) the reported efficiency is defined as the ratio of predicted or measured turbine power to the available kinetic power in the unperturbed incoming flow at inlet

of the domain or flume. This consistency in the definition of the turbine efficiency values reported in experimental and numerical analysis solidifies the basis of the proceeding presented comparisons.

Arrays of Two Coaxial Turbines with Variable Spacing - TSR=7.16

Figure 3.5 shows the numerical simulation results for the performance of two coaxial turbines with different spacing (5D, 8D, 11D and 14D) operating under TSR of 7.16. This figure reveals that, at TSR of 7.16, the upstream turbine in this array has the highest efficiency value (filled blue circle) and the minimum value of performance corresponds to the turbine located at 5D spacing downstream (filled green circle). The reason for the relatively poor performance for the 5D downstream turbine is that this device is put directly in the wake of the upstream turbine with a short spacing of 5D (the minimum spacing in this study). This tight spacing does not allow the wake of upstream turbine to recover. Therefore, at this turbine station the momentum deficit is maximum and the available kinetic energy (incoming into the downstream device) is minimum. As a result of the difference between the incoming flow of these two turbines, and despite the fact that both up- and downstream turbines are operating under the same TSR, the downstream turbine performance is reduced by almost 50%. As the spacing between the two turbines is increased from 5D to 8D, 11D and 14D, the efficiency of the downstream turbine increases gradually.

The comparison between the numerical predictions of device performance and the experimental measurements, in an array of two coaxial turbines with different downstream spacing is presented in figure 3.6. The overall agreement between numerical and experimental results is satisfactory. The predicted trend for performance recovery (filled circles), as the spacing between the two turbines increases, is the same as the trend observed in the experimental data (hollow circles). The relative error between numerical and experimental results for performance of the upstream and downstream turbines is in the range of 1-11%.

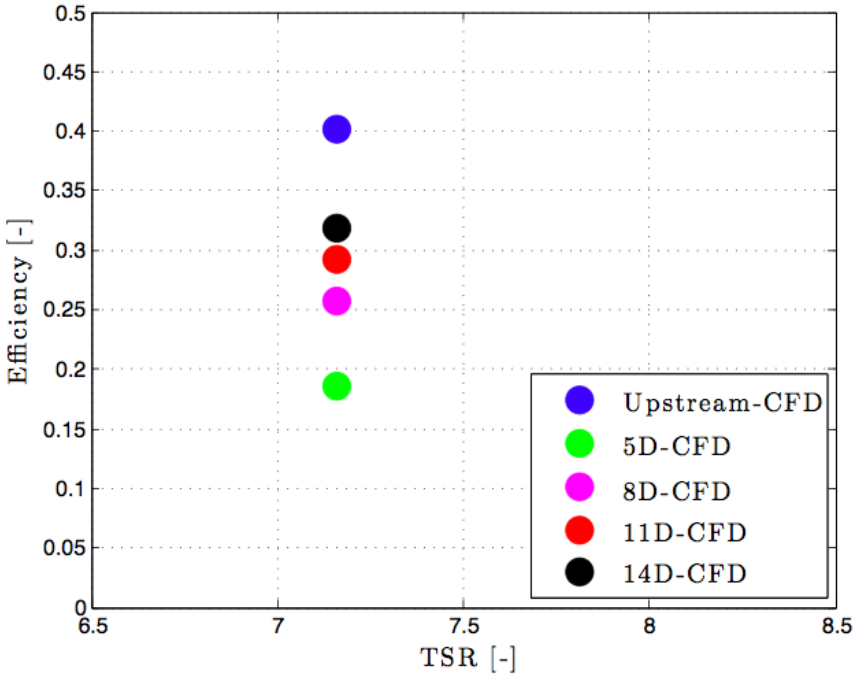

Figure 3.5: **CFD results for arrays of two coaxial turbines operating at TSR of 7.16 with various downstream separations (5D, 8D, 11D and 14D).**

The most significant disagreement between the numerical and experimental results presented in figure 3.6 occurs for downstream turbines with 5D (green circles) and 14D (black circles) spacings. As shown in figure 3.6 for the turbine with 5D spacing, the experimental values of TSR vary between 6.8 to 7.2. However, in the simulations the matched TSR value, as a common value for all turbines, is 7.16. The hypothesis to explain this discrepancy is that the difference in the value of the TSR between experiment and simulation causes the performance to differ between the two cases. To confirm this hypothesis, the array of two coaxial turbine with 5D spacing was simulated at a value of TSR equal to 6.92 (mean value of the experimental TSR range). Figure 3.7 shows the new data point as a green asterisk. This figure shows that, after matching the TSR in the simulation with the experimental value, the

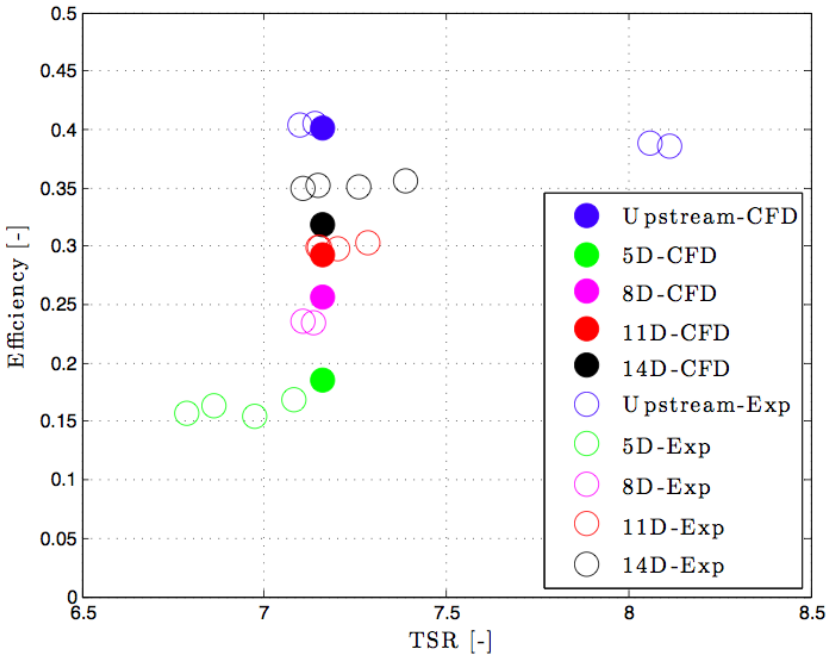

Figure 3.6: **Numerical versus experimental results for arrays of two coaxial turbines operating under TSR of 7.16 with various downstream spacings (5D, 8D, 11D and 14D).**

agreement between numerical and experimental results improved significantly and was comparable to the other cases .

For the case where the downstream turbine is at a 14D spacing, the relative error between the predicted and measured performance is about 10% . This is a large difference compared to the 2% relative error for the predicted performance of the downstream turbine at 8D downstream spacing. As discussed earlier, the BEM is accurate in the simulation of the far wake region. Therefore, it was expected that as the spacing between two turbine increases, the relative error between the measured and predicted results would decrease. The hypothesis to explain this counterintuitive trend is that the numerical simulations are limited in the modeling of the recovery of

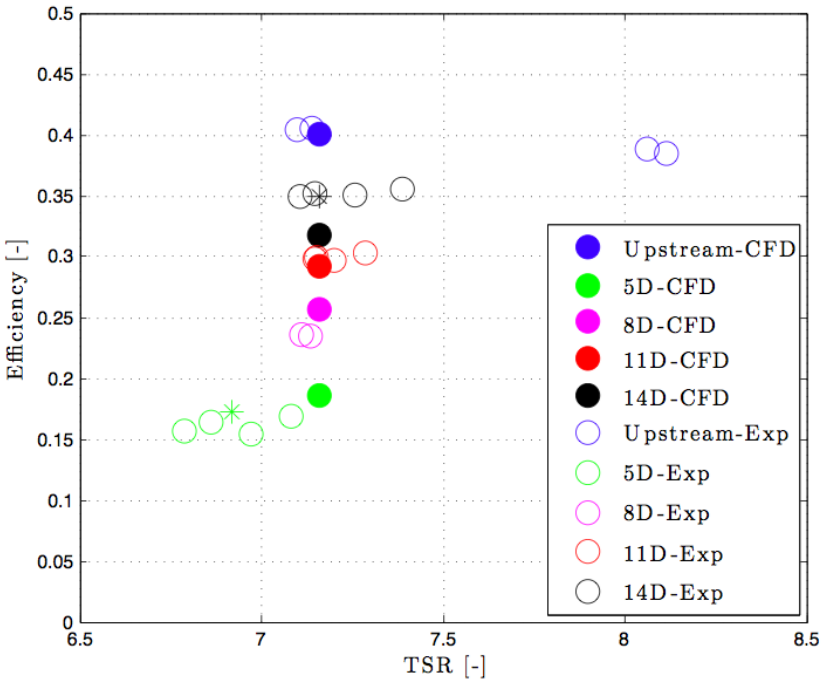

Figure 3.7: **CFD versus experimental results for arrays of two coaxial turbines with correction for 5D and 14D turbines.**

the far wake region in a confined geometry, such as the flume. The experimental velocity profile showed faster wake recovery than predicted by the simulations, specially after 11 diameters downstream of the front turbine. As a result of this inaccuracy, the TSR set for the downstream turbine at 14D spacing was based on the simulated incoming velocity and therefore did not represent well the conditions of the experiments against which it is compared. To confirm this hypothesis, the simulation for the array of two coaxial turbines with 14D spacing was rerun with the same angular velocity of the up- and down stream turbines. This matched values assumed that the far wake will recover to about 98% of the flow velocity at the inlet of the downstream turbine. Figure 3.7 shows the result of this simulation (black asterisk). The numerical and experimental results agree well under this operating conditions, giving credibility

to the explanation for the early differences. This limitation in the numerical simulation of the very far wake and potential should be taken into account when modeling turbine arrays, specially in the absence of experimental data.

Arrays of Two Coaxial Turbines with Variable Spacing - TSR=6.15

Figure 3.8 shows the comparison between the numerical and experimental results for turbines' performances in an array of two turbines placed coaxially with variable downstream spacings (5D, 8d, 11D and 14D). Similar to the results presented in figure 3.7, the trend predicted by the numerical simulations matches the experimental data. The upstream turbine has the highest performance value and the performance of the downstream turbine increases gradually as the downstream spacing increases (from 5D to 8D, 11D and 14D).

Another similarity with the results presented in figure 3.7 is the increase in relative error between the numerical and experimental performance values for the downstream turbine with 14D spacing. As discussed in the previous subsection, this increased discrepancy is caused by the limitation of the numerical simulation to accurately model the far wake recovery in confined spaces. The same procedure of matching the TSR of the up- and downstream turbines, assuming 98% wake recovery, was employed for this case. A large improvement in the accuracy of the predicted efficiency of 14d downstream turbine (shown by a black asterisk in figure 3.8) is again achieved with this improved matching of experimental conditions.

The most significant difference between the predicted efficiency for turbines operating at TSR of 6.15 and those at TSR of 7.16 is the level of agreement with the experimental results at the peak TSR value versus the lower TSR. Figure 3.8 shows that the predicted numerical values for performance of the downstream turbines operating at TSR of 6.17 does not reach the same level of coincidence with experimental results as the simulated values at TSR=7.16. It is hypothesized that the reason behind this difference is the dynamic stall delay observed during the operation of the

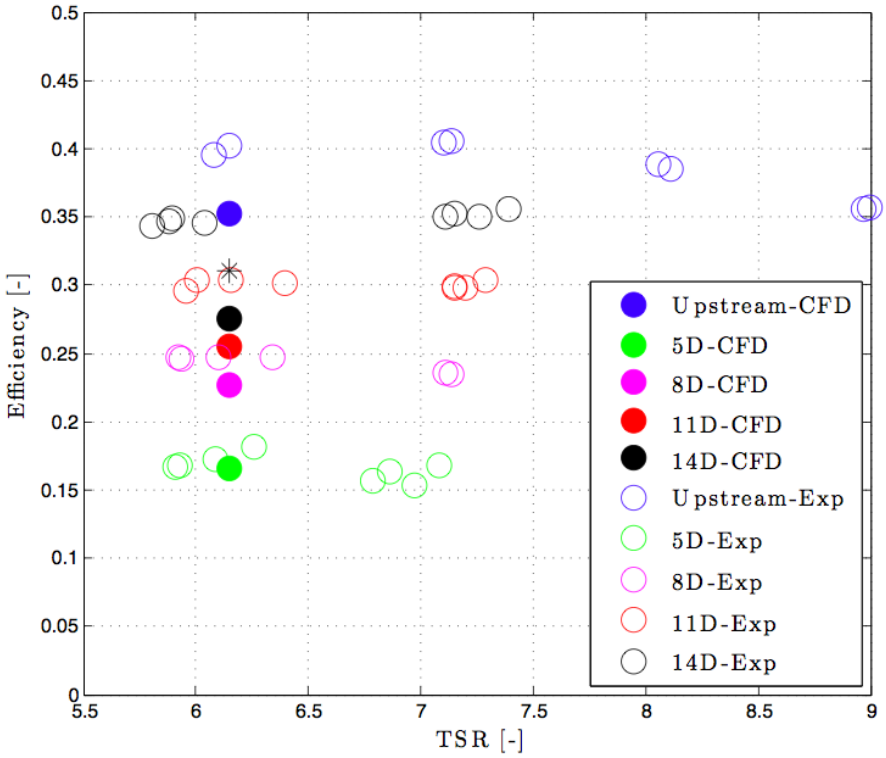

Figure 3.8: **Numerical versus experimental results for arrays of two coaxial turbines operating at TSR of 6.15 with various downstream spacings (5D, 8D, 11D and 14D).**

turbines in experiments at lower TSR values. As described in section 2.3.1, the angular velocity fluctuations that occur in the experiments at lower TSR values have the potential to postpone separation near the blade root, and potentially avoid stall along the blade span. This would explain that as the value of TSR is decreased in the experiments, the value of performance measured is almost constant. This dynamic effect however is not present in the numerical simulations. Due to the absence of this effect, the numerical model predicts the "theoretical" performance curve as a function of TSR, with a marked peak and a smooth decrease in C_p as the TSR is changed from the maximum location. Figure 3.9 presents a side-by-side comparison of numerical

and experimental results and reveals that the numerical simulation does predict the theoretically-predicted drop in the $C_p - TSR$ curve for all turbines. We hypothesize that this phenomenon is avoided during the experiment due to the fluctuations in angular velocity and the dynamic stall effect caused by the rapid change in the angle of attack in the blade sections near the root.

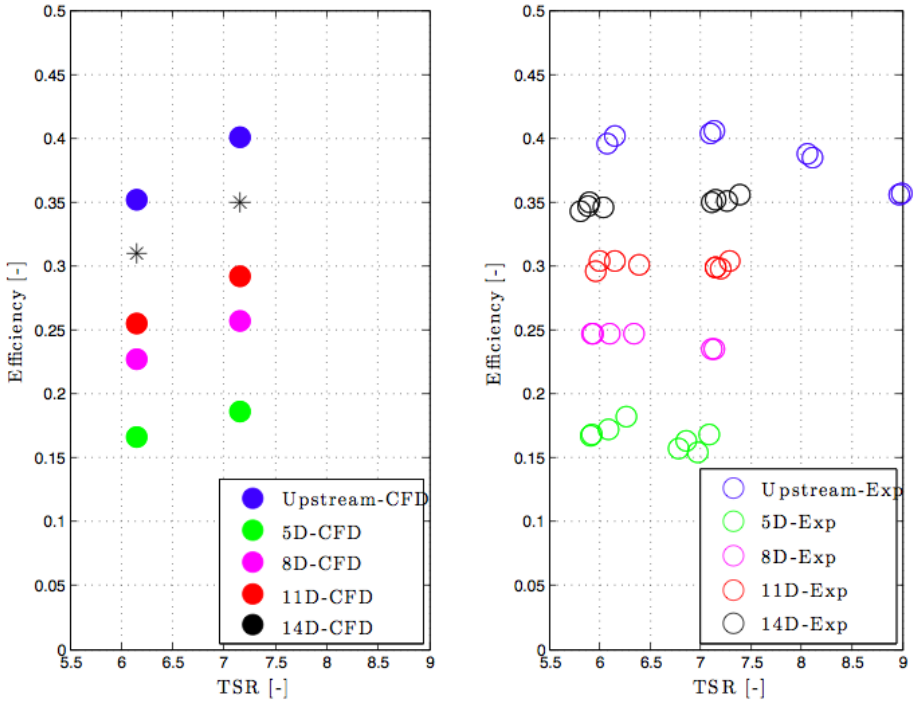

Figure 3.9: **Side by side comparison between CFD and experimental results for array of two coaxial turbines operating at TSR of 6.15 and 7.16 with various downstream spacings.**

To confirm the hypothesis above, we developed an alternative post-processing method for the turbine array experimental data, in parallel to the results presented in section 2.3.1 for a single turbine. In this analysis, the Root Mean Square (RMS) of the time series of the measurements of the normalized angular velocity for each down-

stream turbine at TSRs of 6.15 and 7.16 was calculated. Figure 3.10 presents the comparison of these RMS values. As shown in this figure, the RMS values of the angular velocity fluctuations for turbines operating at a TSR of 7.16 vary within a small range of 0.05-0.06. The corresponding RMS values for turbines operating at a TSR of 6.15 move in a wider range, between 0.06-0.09. This observation shows that the angular velocity fluctuations at a TSR of 6.15 are stronger, and have higher frequency content, than the fluctuations during TSR of 7.16. This supports the hypothesis that the large fluctuations lead to delaying separation near the turbine blade root, contributing to higher performance than would be expected if the angular velocity were held truly constant.

It should be highlighted that the discrepancy between the numerical and experimental values for turbine efficiency would not be a concern for full-scale turbines analysis. In the full-scale turbines, any type of unsteadiness during turbine operation, such as fluctuations in rotor angular velocity, is highly undesirable. Specifically, the fluctuations in rotor angular velocity are undesirable from both electrical and mechanical engineering points of view. These fluctuations would harm the generator and also lead to fatigue and structural failure of the turbine blades and structure. Therefore, the full-scale turbine control system are designed precisely to avoid any undesired unsteadiness and maintain a constant TSR. As a result of this strict control in full-scale turbines, dynamic effects on the flow over the blades are minimized and the performance of the turbine would not be affected by dynamic stall and match the theoretical shape of the $C_p - TSR$ curve closely. Hence, the CFD results can be considered good representations of the performance when constant angular velocity is imposed, and they should represent well full-scale conditions for which unfortunately experimental measurements are not available.

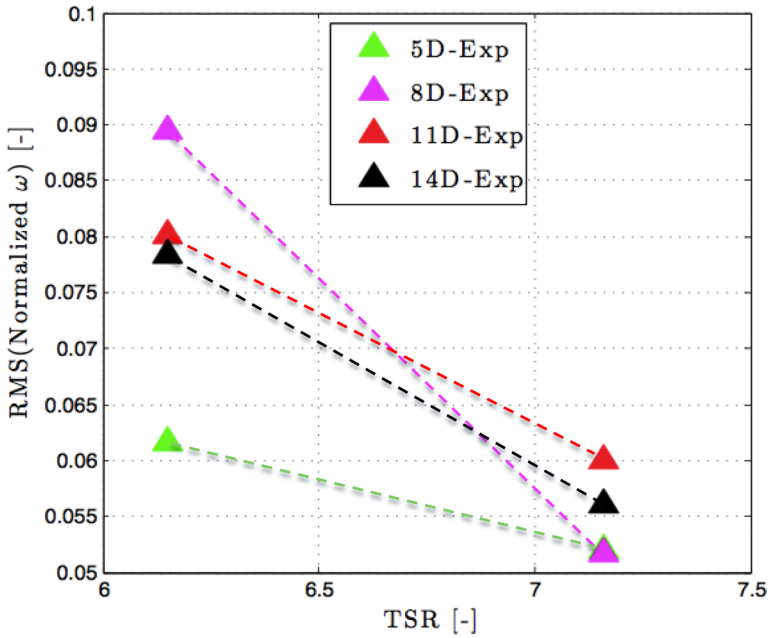

Figure 3.10: **Root Mean Square (RMS) of the normalized angular velocity with mean value for downstream turbines in arrays of two coaxial turbines with variable downstream spacing.**

Array of Three Coaxial Turbines with Fixed 5D Spacing

Figure 3.11 presents the comparison between numerical and experimental results for the array of three coaxial turbines operating under a range of TSRs from $\approx 5-7$. Similar to the previous results for arrays of two coaxial turbines shown in figure 3.9, the agreement between the numerical and experimental results are best at TSR values close to the optimum (≈ 7). An important point to notice in figure 3.11, is the deviation between the numerical and experimental results for the performance of the middle turbine, 5D downstream of the front turbine in this array ($\approx 37\%$). There is considerable uncertainty in the experiments: comparing the two experimental values of performance for the turbines located 5D downstream of the front turbine, one in a

two turbine array (figure 3.9) and the other the middle turbine in a three turbine array (3.11) reveals that the efficiency decreases by about 20%. The numerical value stays constant in both simulations. If an average value of the two experimental efficiencies measured is used, the error between the numerical and experimental results would be less than 10%, in line with other results.

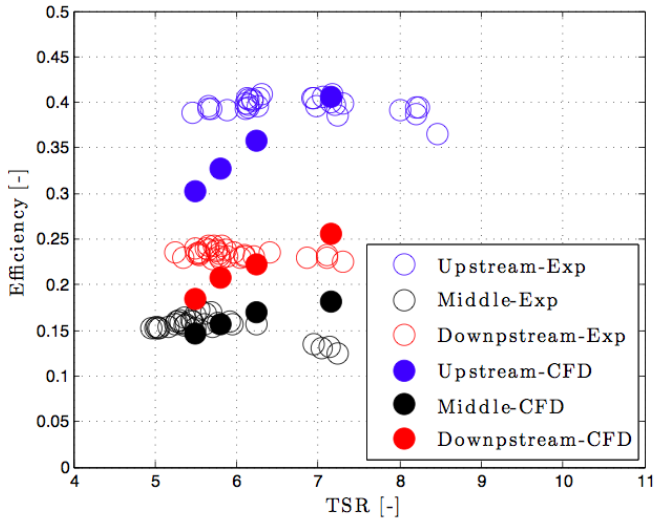

Figure 3.11: **Numerical versus experimental results for arrays of three coaxial turbines with 5D downstream spacing, operating under various TSR.**

As the TSR value moves away from the peak toward smaller values, the agreement between the numerical and experimental data decreases. As discussed previously, the reason behind this difference can be associated to a dynamic stall effect in the experiment, caused by rapid oscillations in the angle of attack of the sections near the root, induced by the unsteadiness in the turbine angular velocity. The experimental values show an almost constant performance for the turbine despite the reduction of the TSR value. In numerical results, however, there are no fluctuations in angular velocity of the turbine and no dynamic separation delay. The predicted $C_p - TSR$

curve, shown in figure 3.11, corresponds to the theory and the turbine efficiency decreases as the value of TSR decreases.

An important observation made in both simulations and experiments relates to the trend in turbine efficiency in the three turbine array. Figure 3.11 shows that the performance of the most downstream turbine is higher than that of the middle turbine. At first glance, this seems physically counterintuitive: The first two turbines are extracting energy from the flow, and so it is expected that the most downstream turbine would see a lower incoming kinetic energy flux than the other two turbines and have lower performance. To explain this trend, we hypothesize that the middle turbine extracts energy from the yet-unrecovered wake of the most-upstream device. The presence of the middle turbine introduces turbulent kinetic energy that mixes the wake with the surrounding free stream fluid, speeding up the recovery of the velocity profile behind the two turbines. This wake recovery enhancement results in an increase of the incoming flux of kinetic energy into the rotor plane of the most-downstream turbine. The most-downstream turbine, operating at the same TSR as the others in the array, extracts more energy from the flow than the middle turbine because it receives more incoming power.

To explore this hypothesis, the normalized velocity contours, with the free stream velocity at the inlet, is visualized in figure 3.12. These contours reveal that the inflow to the rotor zone of the most-downstream turbine has higher velocity magnitude (warmer colors) compared to the inflow of the middle turbine (colder colors). The calculated kinetic energy fluxes on planes two diameters upstream of the rotor for the middle and most-downstream turbines are 46.66 and 51.21 [W] respectively. This calculation shows that the value of incoming kinetic energy flux for the most-downstream turbine is about 10% larger than for the middle turbine. The experimental velocity profiles measured at two diameter upstream of the rotor for each turbine also show this trend and support this hypothesis [17].

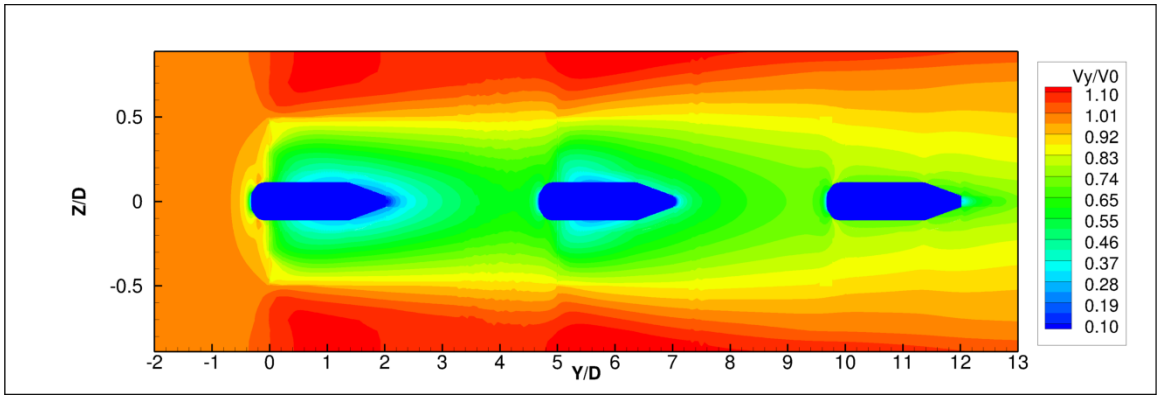

Figure 3.12: **Normalized velocity contours, with free stream velocity, in the array of three coaxial turbines with 5D spacing.**

3.2 Numerical Methodology Application to HAHT Array Optimization

3.2.1 Dominant Spacing Variables in Turbine Array Optimization

In the process of turbine array optimization in a tidal channel, the dominant spacing variables that have a major effect on the overall power extracted by the turbine array are the downstream spacing between rows, the lateral offset between columns, and the tip to tip distance between turbines in the same row. These three variables define the turbines' position with respect to each other, and they control the interaction of each turbine with the others' wakes, as well as the impact of the turbine on all others, therefore determining the overall power extracted by the turbine array.

Downstream Distance.

One of the most important spacing variables in the array optimization of hydrokinetic turbines is the distance between two rows of turbines in the array (the upstream and downstream turbines showed in figure 3.13). The upstream turbine extracts energy from the undisturbed incoming flow. This power extraction will create a velocity deficit and enhance turbulence inside the wake region. This wake becomes the inflow

for the downstream turbine. In order for the downstream turbine to extract the maximum power from this altered flow field (i.e. the wake), the downstream distance needs to be optimized. The larger the distance between the two rows of turbines, the better the momentum deficit will have recovered and the downstream turbines will have the unperturbed kinetic energy flux to work with. A large downstream spacing would reduce the number of rows that can be placed as part of the array in a given site. As site natural restrictions and permitting place a strong limit on the area where turbines can be installed, the optimization of a given turbine set in a given site needs to balance the number of turbines placable in the area available, with the energy production of each turbine, to maximize the total array power production.

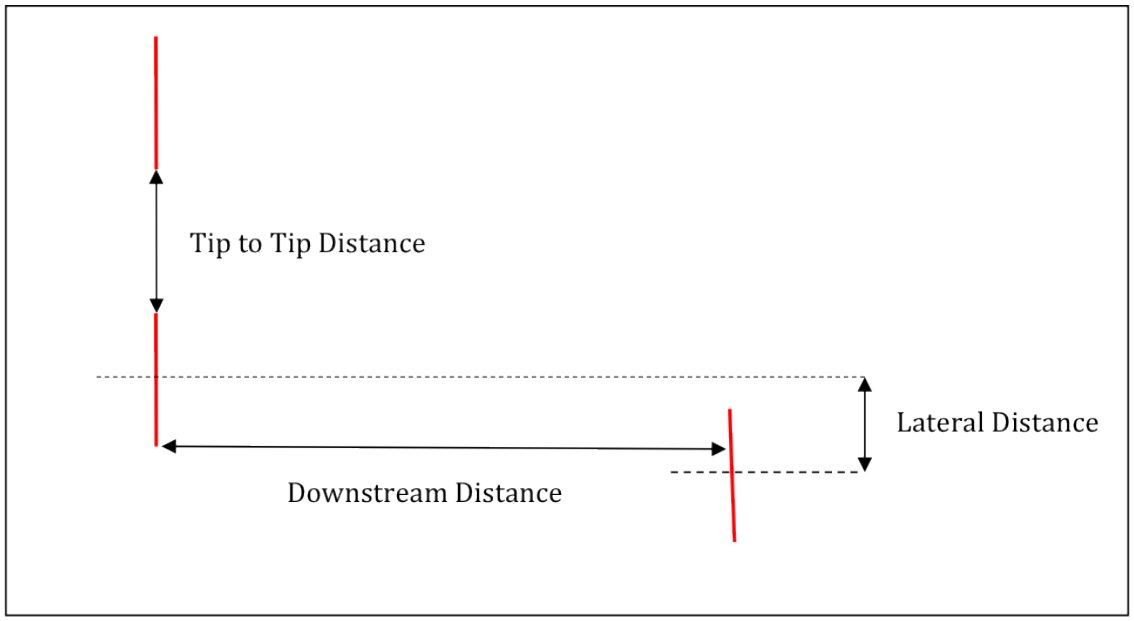

Figure 3.13: Schematic of the dominant spacing variables: downstream spacing, lateral offset and tip to tip distance in turbine array optimization. Solid red lines represent the turbines.

Lateral Distance.

This distance defines the lateral offset between the axis of rotation of two turbines, one placed downstream of the other, in two consecutive rows (figure 3.13). This space provides the opportunity for the downstream turbine to not be fully immersed in the wake of the upstream turbine. If two devices are placed coaxially (i.e. zero lateral offset) at a given downstream separation, then the effect of the upstream turbine wake on the downstream turbine will be maximum. Furthermore, having a tight lateral offset between two turbines would cause undesirable loading on the turbine blades and support structure, which might result in fatigue, fracture and failure of the device. Having a sufficient lateral distance guarantees the mixing of the wake with the undisturbed flow and, hence, a reduction of the velocity deficit incoming to the downstream turbine. The downstream turbine kinetic energy flux is increased and would operate more efficiently than a coaxial configuration. In summary, having a large lateral offset would allow the turbines to operate without inter-device penalties, but requires a large amount of space which would make inefficient use of tidal sites. A coaxial configuration, or a small lateral offset, would lead to strong turbine-wake interactions, with lower power production and high structural loading on the turbine.

Tip-to-Tip Distance.

This variable measures the distance between adjacent blade tips of two side-by-side turbines (figure 3.13). This distance is important with regards to two aspects. The first one is the effect of the turbines' rotation direction on each other. Based on the sense of rotation, high momentum free stream fluid can be induced into or out of the inflow of the neighboring turbine and this will affect the efficiency of that device. The second aspect to investigate is the interference of the tip vortices, generated by one turbine, on the operation of the neighboring turbine. This distance needs to be kept at a minimum with the limitations based on the severity of these potential effects of

the adjacent turbine interference.

3.2.2 Computational Domain.

In this section, the computational domain created to investigate the effect of the three array distances mentioned above is presented. The computational domain allows two of the spacing variables to be fixed, while the third variable is varied within a broad range and its effects investigated.

Figure 3.14 shows the top view of the computational domain used to investigate the effect of the spacing variables between turbines in an array configuration. Each dashed line represents one possible rotor location in the tidal channel. As mentioned previously, BEM allows these rotor zones to be enabled or disabled to explore different variables and array configurations.

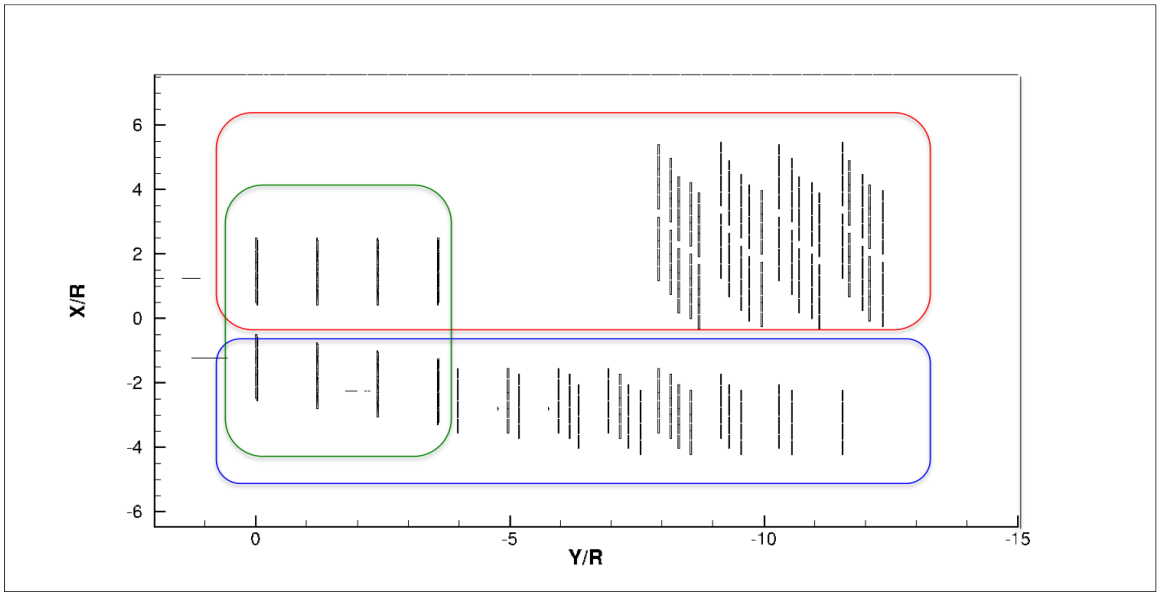

Figure 3.14: **Top view of the computational domain for investigating the effect of the dominant spacing variables in different turbine array configurations.**

The color boxes in figure 3.14 show the turbine configurations used to investigate the effect of the three spacing variables, downstream distance, lateral offset and tip-to-tip distance, in the turbine array optimization. The blue box highlights turbines configurations that combine an upstream turbine with one or more downstream turbines. The red box in figure 3.14 shows multiple downstream turbines at different lateral offsets from the upstream turbine operating in the far wake region of the upstream device. This provides the opportunity to investigate the effect of lateral offset on the efficiency of the downstream turbine. Finally, the green box covers multiple side-by-side turbines with various tip-to-tip distances.

As shown in figure 3.14, the space between the two possible downstream rotors is narrow compared to the turbine diameter. This small spacing causes high aspect ratio elements in the computational domain discretization (i.e. the meshing process) and will result in poor mesh quality. Therefore, the original domain was modeled with two different arrangements of turbines that are complementary. These two representations of the flow field, each with a different arrangement of the turbines, allow, when taken together, to study all possible combinations of spacing distances that were planned in the original domain. The differentiation enables the creation of high quality mesh elements with reasonable aspect ratios in the region between the rotor zones.

Figure 3.15 details the construction of the two computational domains. The flow direction is from left to right and the color corresponds to the position of the downstream turbines. For example, the green color in figure 3.15 highlights the two turbines downstream of the two most-upstream turbines, 1-RHS on the Right Hand Side and 1-LHS on the Left Hand Side. In naming the coaxial downstream turbines, the first number corresponds to the closest upstream turbine and the second number indicates the downstream distances from the first row. For example, $1-4R$ refers to a turbine four radii downstream of the first two turbines (1-RHS and 1-LHS). Alternatively, for the off-axis downstream turbines, the first number corresponds to the closest upstream turbine and the second number refers to the lateral offset. For example, $1+0.25R$

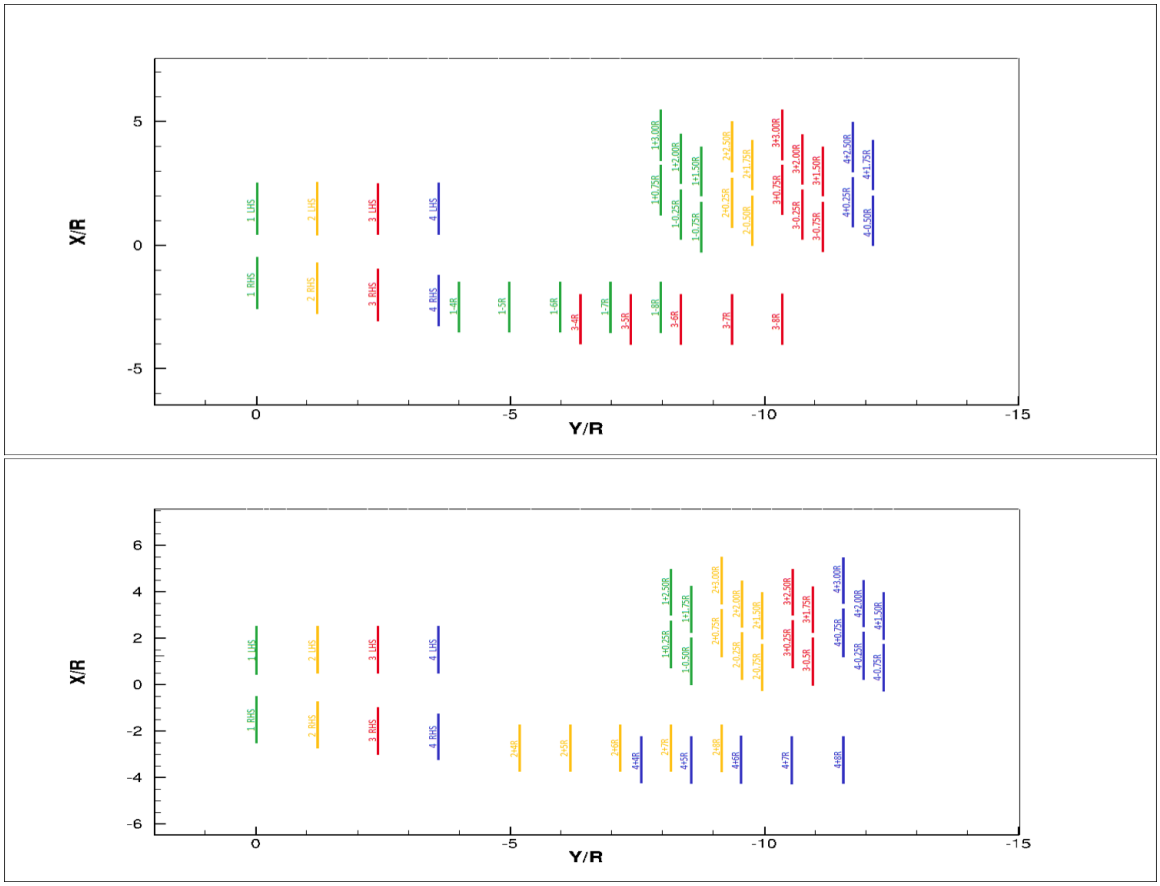

Figure 3.15: **Top view of the computational domains for the investigation of the effect of the spacing variables in different turbine array configurations.**

indicates a downstream turbine that is 0.25R off-axis from upstream turbine number 1.

3.3 Results

This section discuss the results from the investigation of the effects of the three spacing variables on array performance. The long term goal is to find a mathematical tool that considers the limitations and capabilities of the BEM and to propose a general numerical optimization methodology based on our investigations. This methodology

should be able to propose optimized HAHT turbine configurations with minimum computational time and cost.

CFD is used as a tool to numerically characterize the effect of each of the three spacing variables in the array optimization process. According to the discussion presented earlier in chapter 3, BEM is a good candidate CFD tool for turbine array optimization studies.

In order to develop a general numerical methodology to characterize the effect of the dominant spacing variables in the array optimization process, a previously calibrated RANS flow field solution around the NREL Phase VI turbine (modeled as a hydrokinetic turbine) was used. The reason behind the choice of the NREL Phase VI as a hydrokinetic turbine was that, at the time of this study, there were no publicly available data for an actual HAHT design such as the DOE RM1. The RANS model of the NREL Phase VI was developed [18] based on a general numerical methodology applicable to wind and MHK turbines [23], and validated based on published AMES wind tunnel test results [24] [48]. For a full overview of the validation and verification of the model, the references above contain the detailed methodology. Here, comparisons of the BEM-modeled flow field with two fundamental fluid mechanics theories are presented.

Figure 3.16 shows the decay of the centerline velocity modeled in the wake of NREL Phase VI turbine. After two radii downstream, the centerline velocity decays as $x^{-\frac{2}{3}}$, where x is the distance downstream of the turbine rotor plane. This centerline velocity decay trend matches the analytical self-similar solution of the velocity deficit decay in the turbulent wake of a blunt body [75]. It is also observed, in figure 3.17, that the momentum deficit in the wake normalized with the available momentum at the inlet of the channel is constant at different downstream distances. This shows that, for this high Reynolds number flow, the wake predicted by the RANS/BEM simulation satisfies conservation of momentum. These two comparisons, together with evidence in the literature, show that BEM is a suitable tool to develop a general computational

methodology for optimization of arrays of HAHTs.

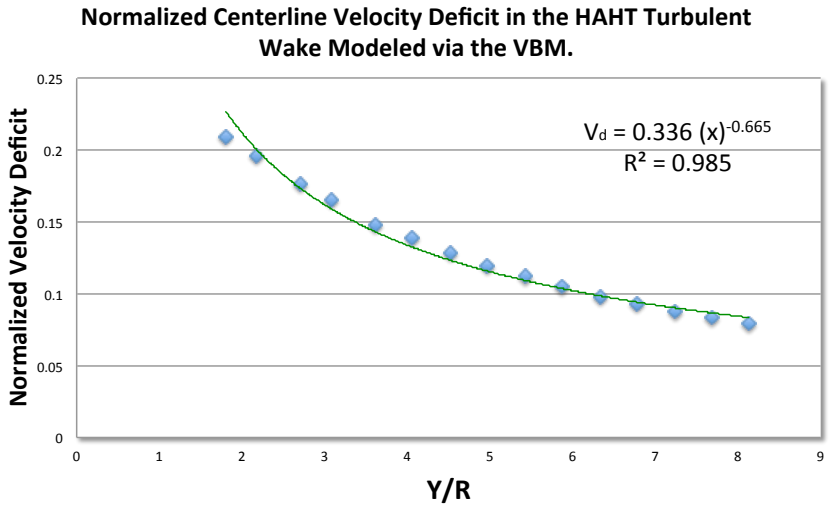

Figure 3.16: **Velocity deficit decay trend in the wake of an HAHT modeled via BEM.**

3.3.1 Downstream Distance

To investigate the effect of the downstream distance in the process of array optimization, the operation of a second row turbine that is located coaxially with one of the upstream row turbines, is analyzed for different downstream distances. The velocity deficit recovery in the wake of the relevant upstream turbine is analyzed in figure 3.18. The $x-$axis represents the normalized streamwise velocity and the $y-$axis shows the vertical coordinate, measured from the turbine hub and non-dimensionalized with the rotor radius. The velocity profiles at 5, 8, 10, 12 , 15 , 20, 25, 30 and 40 radii downstream are plotted to show the recovery of the wake with distance downstream. The velocity deficit predicted by BEM is axisymmetric and goes from a maximum at the rotor centerline to an overshoot, with accelerated flow with respect to the free stream velocity past the blade tips. This flow acceleration, necessary to maintain continuity,

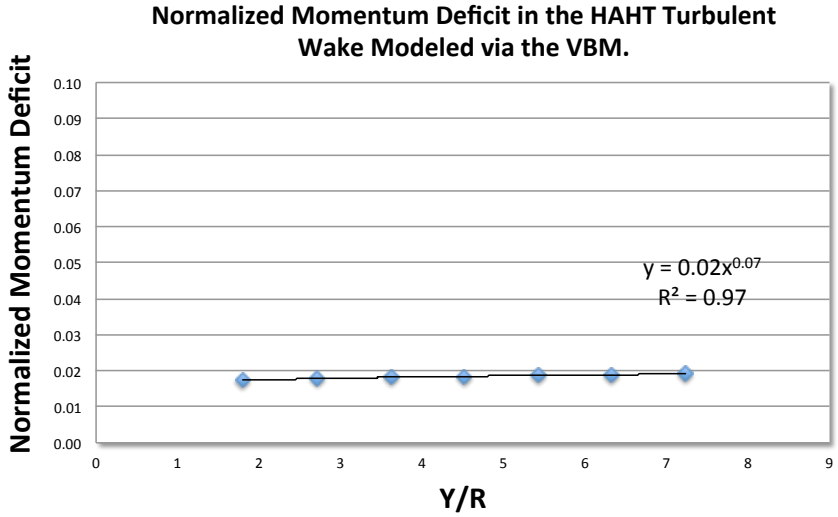

Figure 3.17: **Momentum deficit trend in the wake of an HAHT modeled via BEM.**

is grossly exaggerated by the blockage effect of the turbine in a very confined environment. According to figure 3.18, the velocity deficit has recovered to within about 80% of the free stream at the distance of 8R downstream and, thus, it represents an optimum trade-off between utilization of the tidal channel site and energy recovery by the downstream turbines in the array

3.3.2 Lateral Distance

For the investigation of the lateral offset in array optimization, the downstream location of the second row of turbines was fixed at 8R. The lateral offset of the downstream turbine with respect to one upstream turbine was varied in the computational domain shown in figure 3.15 and the power extracted by the second row turbines computed. Figure 3.19 shows the power extracted by each turbine normalized with the available power at the inlet, versus the lateral offset of the downstream turbine. In this analysis, the coaxial position is represented by a zero lateral offset. An offset that takes the

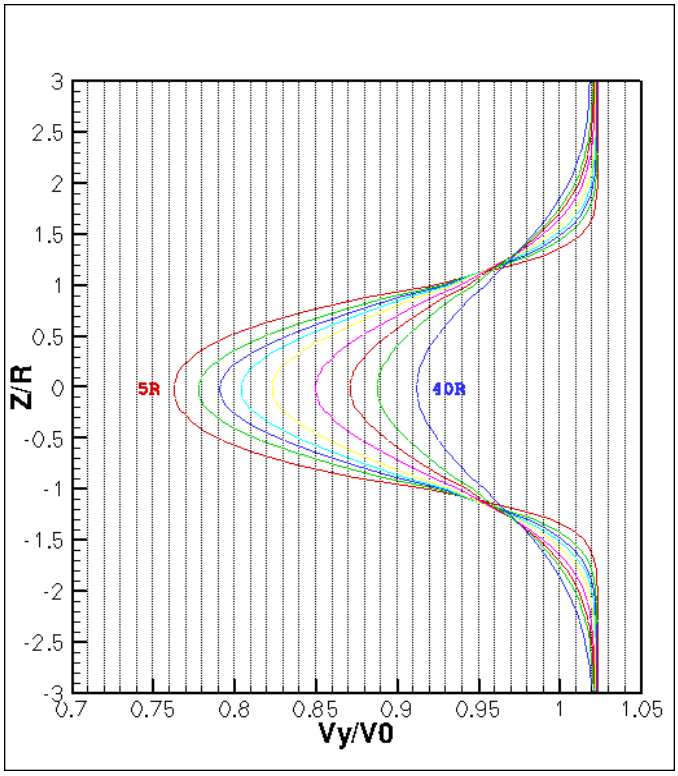

Figure 3.18: **Velocity deficit profile in the wake of an HAHT modeled via BEM (red: 5R, green: 8R, blue: 10R, cyan: 12R, yellow: 15R, magenta: 20R, dark red: 25R, dark green: 30R, and dark blue: 40R).**

downstream turbine towards the gap between the two upstream turbines is defined negative direction, see figure 3.19. The salient points in this figure are the fast recovery of the power with lateral offset and the symmetric relationship between extracted power and lateral offset. Increasing the absolute value of the lateral offset from the coaxial position increases the extracted power, with a linear dependency that does not depend on the sense of the offset (into or away from the front turbines tip-to-tip gap). The downstream turbine extracted power recovers to 100% at about 1.75R, showing that the entrainment of free stream fluid into the wake speed up recovery, and the wake expansion does not have a negative effect on the downstream turbine

power production. The front row turbines tip-to-tip distance was varied over a relatively large range and shown to not have significant effect on the extracted power by the downstream turbine.

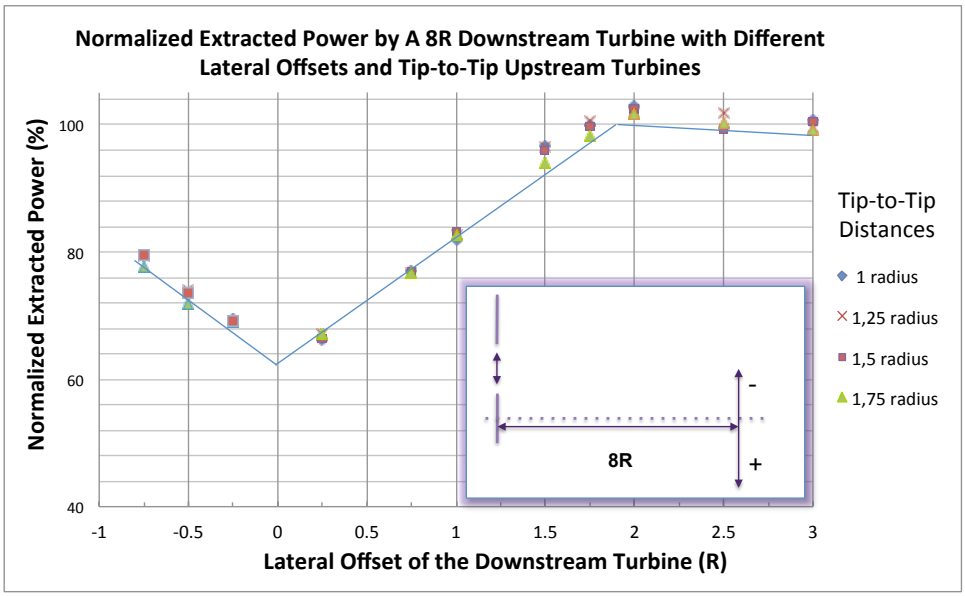

Figure 3.19: **The effect of lateral offset of the downstream turbine on performance. Different tip-to-tip distances in the upstream turbines were investigated.**

An important physical effect associated with the lateral offset is the resulting moment on the turbine blades due to the shear flow as part of the rotor is in the wake of an upstream turbine and part is in the free stream. This moment on the turbine blades can lead to fatigue and structural failure of the blades. Figure 3.20 shows the total moment on the rotor plane. The moment has a local minimum at the coaxial position (zero offset) and increases as the offset increase, exposing the downstream turbine to significant shear. The trend changes at a value of the lateral offset equal to the radius, where an increase in the lateral offset will result in more than 50% of the rotor swept area being outside the wake, therefore reducing the shear experienced by the blades

in their trajectory. The moment has an absolute maximum at that position, 1R, and then decreases monotonically as the lateral offset increases further.

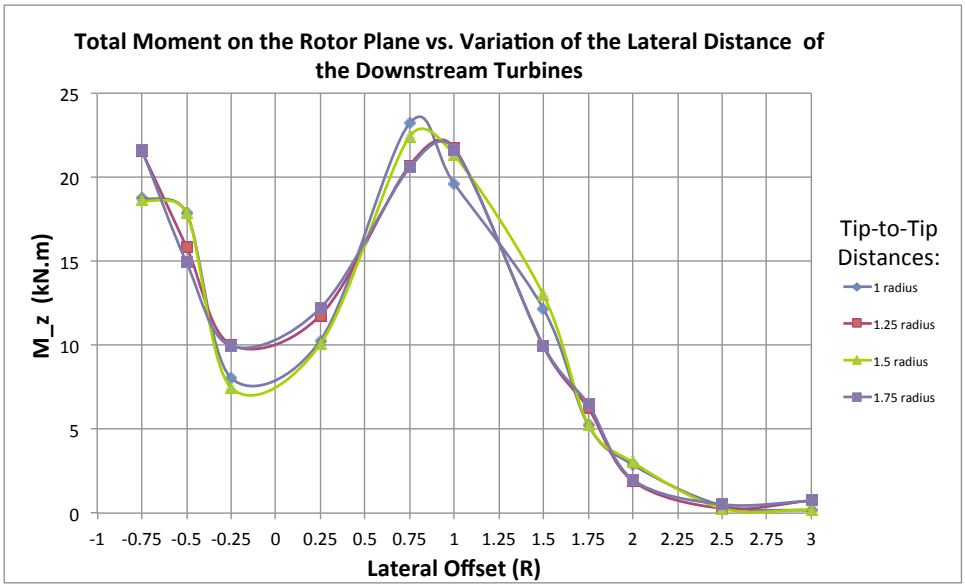

Figure 3.20: **Effect of lateral offset on the resultant moment on the downstream turbine rotor plane. Different tip-to-tip distances in the upstream turbines were investigated.**

3.3.3 Tip-to-Tip distance.

As discussed in the previous results, the tip-to-tip distance did not affect the power extracted by the downstream turbines, as long as the downstream distance was larger than a minimum value, 8R, which represented a trade-off in the packing of turbines in a given area without large sacrifices to the individual efficiency of turbines. The effect on the operation of the front row turbines was also studied during our investigations, where it was observed that different tip-to-tip distances above a minimum of 1R, do not play a significant role on the operation of the front row turbines. This is consistent with the the use of a reduced tip-to-tip distance, close to one radius, in

MCT's SeaGen twin-rotor design.

3.3.4 The Cumulative Effect of the Dominant Variable Distances

The analyses in this section have concentrated on the comparison of the efficiency of a downstream turbine against the unperturbed case, as the three spacing distances were individually varied. The efficiency in the array positioning was defined as the power extracted by the turbine in a certain array position, normalized by the power available in the undisturbed flow at the inlet of the channel:

$$\eta = \frac{P_{extracted}}{\frac{1}{2}\rho V_{\infty}^{3} A}. \tag{3.1}$$

To consider the cumulative effect of multiple spacing variables varied at once, the classical definition of the efficiency is not useful. The important aspect of the efficiency in the array optimization process is how much kinetic energy flux is going through a given position (array placement efficiency) and how efficiently each device in the array extracts energy from the available kinetic energy at that position (the turbine "local efficiency"). The local efficiency definition requires the quantification of the incoming kinetic energy flux into each turbine rotor plane (P_{avail}). This flux is based on the velocity averaged on the projection of the rotor swept area on a plane two radii upstream of the turbine (V_{local}). Figure 3.21 shows the ratio of the velocity averaged on the projection of the rotor swept area at different distances upstream, to the velocity at the inlet of the channel. This incoming velocity to unperturbed velocity ratio approaches 1 at about 2R-2.5R upstream of the turbine, quantifying the minimum separation needed for the turbine induction effect to vanish. This data supports the choice of 2R in the definition of the local efficiency for each turbine.

$$\eta_{local} = \frac{P_{extracted}}{\frac{1}{2}\rho V_{local}^{3} A}. \tag{3.2}$$

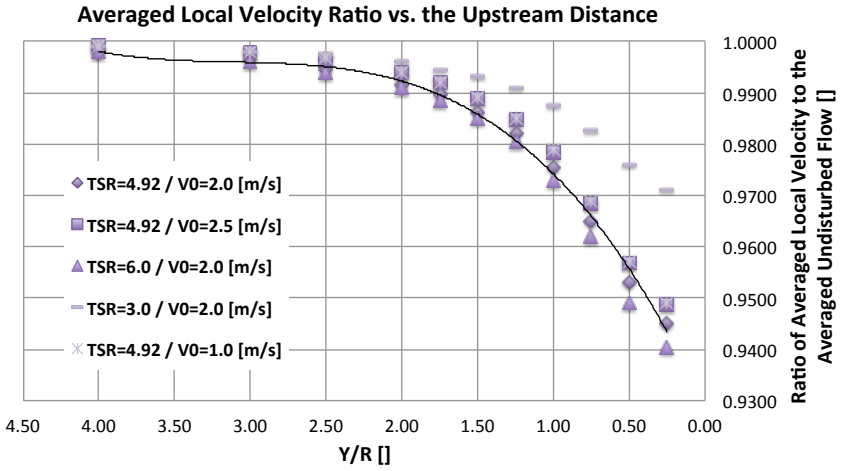

Figure 3.21: **Local velocity averaged over the rotor swept area projected on a plane upstream of the turbine, normalized with the undisturbed free stream velocity.**

Figure 3.22 shows data from sixty different simulations using various turbine configuration to investigate the effect of spacing variables on turbine performance. The power extracted by the turbine depends linearly with the local kinetic energy flux. All the data falls along the same slope, which is equivalent to the local efficiency of all turbines being constant, regardless of their position in the array. The value of this local efficiency for the turbine studied is equal to 22%. It should be noted that this simplified mathematical trend is obtained with the limitations of the BEM, as discussed earlier in chapters 2 and 3. This result is not fully physical, but it provides a significant reduction in the computational cost of evaluating a wide range of turbine array configurations with this simulation method. The constant local efficiency approximation provides a very fast estimate, without multiple computations for different turbine locations, to evaluate all possible positions of turbines in a given row, based only on the flow field behind the upstream rows. As a benchmark for the computational expediency of this method, the SRF model is limited to simulate coaxial arrays

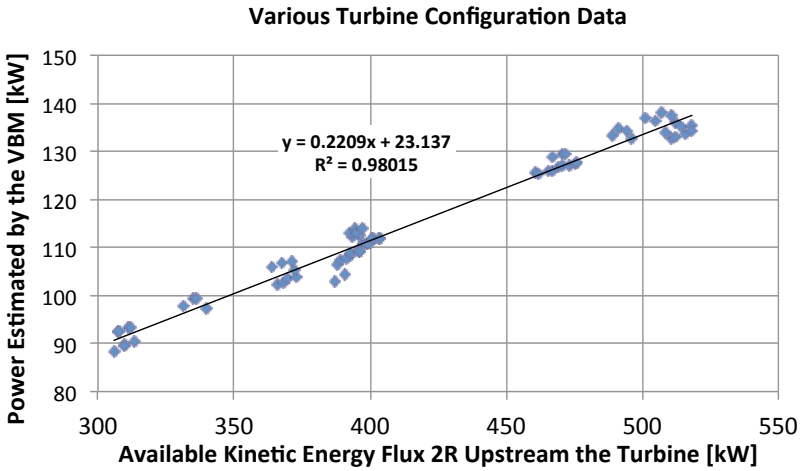

Figure 3.22: **Power extracted by a HAHT as a function of the available kinetic energy flux, defined at 2R upstream of the turbine. The slope defined by the data represents that the local efficiency of the turbines in the array.**

and its simulation run time for small arrays will be in order of couple of weeks. The sliding mesh model is capable of simulating turbines with a lateral offset but would take few months to compute even a small array. BEM simulations for array with multiple rows of turbines take less than 10 hours. Once a few array configurations are proposed based on this estimation method, they can be investigated thoroughly by more sophisticated and accurate models.

3.4 The General Numerical Methodology for the Turbine Array Optimization Process.

A general numerical methodology for array optimization of HAHT is proposed based on the simplification introduced by the constant local efficiency feature of the BEM simulations observed in the parameter range studied in the previous section. The

goal of this methodology is to narrow down the wide range of turbine array configurations, reducing the cost of optimization and focusing on estimating best turbine arrangements in a limited number of rows and columns. The proposed configurations can then be trimmed with more detailed simulations from fidelity numerical models further in the optimization process.

The numerical methodology for array optimization process is presented with an example: Consider a permitted region of a tidal channel, as shown in figure 3.23 by red dash line. There are eight turbines that need to be placed in that constrained area, optimizing their relative position to maximize power extraction and potentially minimize other constraints such as infrastructure cost. Due to the permitted area width (i.e. 10R) and minimum tip-to-tip clearance (i.e. 1R), at most three turbines can be placed in each row, along the width of the channel.

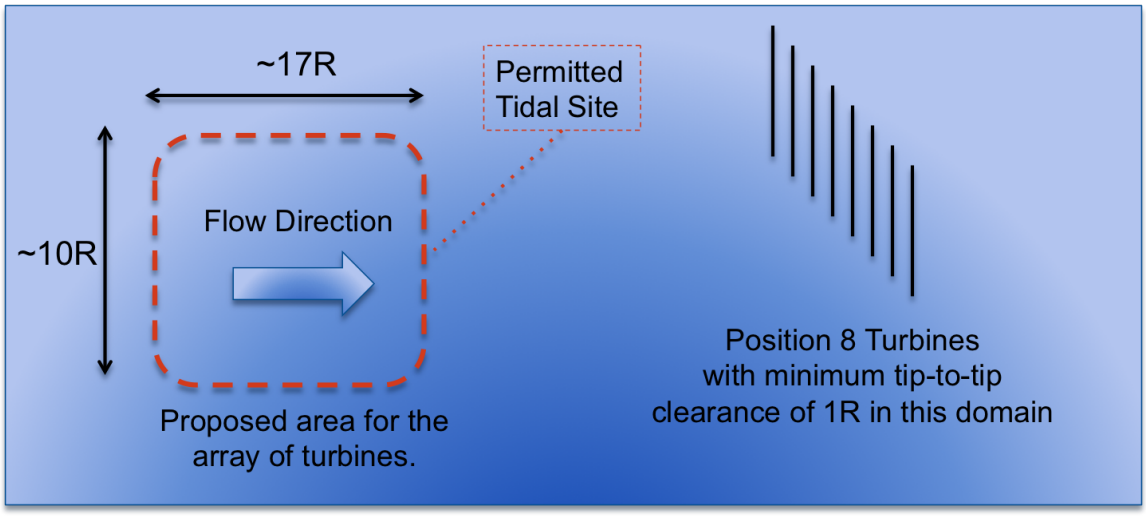

Figure 3.23: **Schematic of a constrained permitted turbine siting area for an array optimization problem.**

The first, obvious, step is to place three turbines side-by-side in a row, as close as possible to the inlet of the channel, as shown in figure 3.24. The computational

domain with these three turbines is created and one RANS simulation performed to model the flow field in the wake of these three devices.

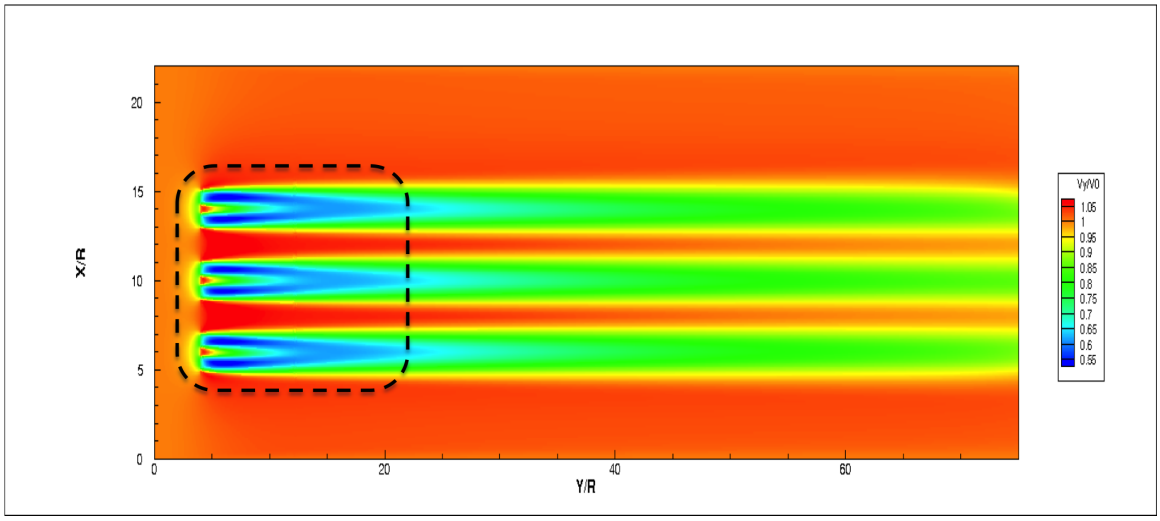

Figure 3.24: **Schematic of first turbine row in the tidal channel.**

The linear relationship between the available kinetic energy flux upstream each turbine and the estimated power extractable by a turbine in the channel (figure 3.22) provides, via simple post-processing, the extracted power map at any point in the domain, based solely on the flow field behind the first row. Based on this map, the locations of the turbines in the second row can be set (see figure 3.25).

At this stage, the location of first two rows of turbines, containing 6 turbines are set and another computational simulations for this turbine arrangement is executed. The flow field on the wake of these devices yields the flow field in which the remaining third row of turbines will operate. Taking advantage of the simplification given by the constant local efficiency, the location of the turbines in the last row is determine to maximize the array power production (see figure 3.26). At this stage the estimated array power via BEM was compared against the predicted array power based on the assumption of constant local efficiency. It was showed that the array power produced

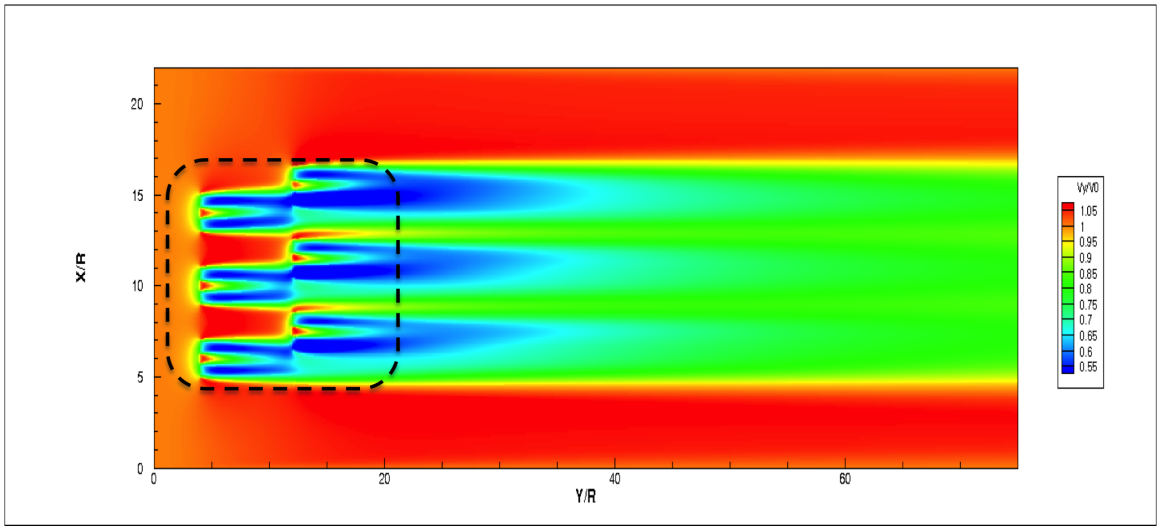

Figure 3.25: **Schematic of the second turbine row in the tidal channel.**

by these eight turbines estimated by the BEM was about 781.11 [kW]. The corresponding predicted array power, based on the constant local efficiency assumption, using the above-explained methodology was 784.18 [kW]. The relative error of less than 1% between these two reported values and other similar case studies confirmed the potentials and capabilities of this numerical methodology to propose an optimized turbine configuration with minimal computational cost and time.

It can be argued that the proposed optimized array of turbines is minimally affected when tides are reverses. Consider the proposed optimized array shown in figure 3.26 and the fact that the tide direction will be reversed so that the flow direction will be from right to left. In this case, the third-row turbines would operate efficiently, since their intake flow is undisturbed. The distance downstream for the two middle-row turbines was optimized initially with respect to the first row turbines. The downstream spacing between middle third row device and two middle row turbines would be suboptimal. It should be highlighted that the core of velocity deficit in the wake of the middle front-row turbine will pass through the spacing of the middle

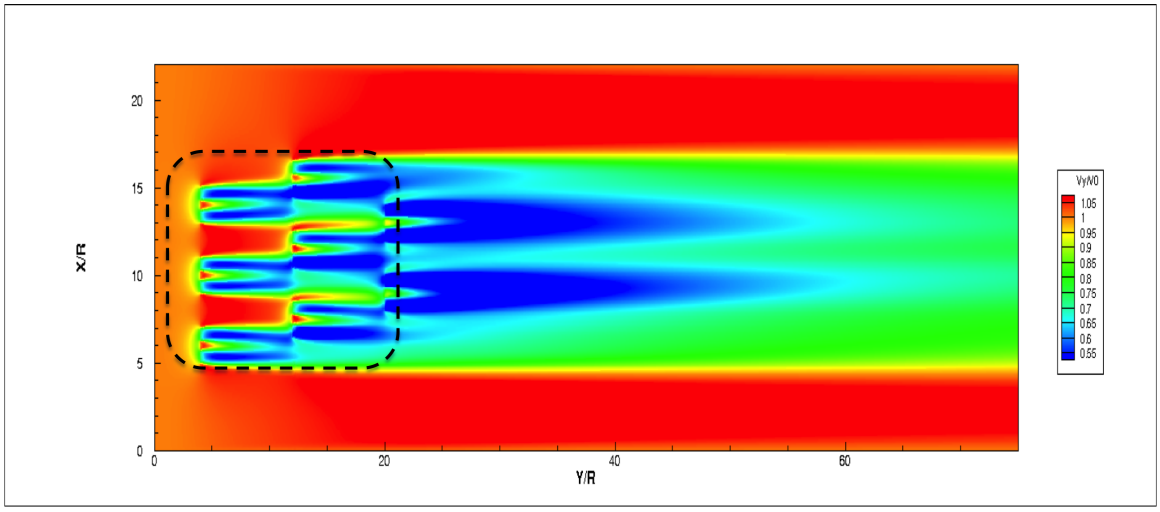

Figure 3.26: **Schematic of the third turbine row in the tidal channel.**

row turbines. Therefore, this velocity deficit won't significantly affect the operation of the downstream turbines. Furthermore, the downstream distance between middle row and the first devices is optimized as the flow reverses because the lateral offset effects are symmetric. The proposed array would still operate efficiently when the tide reverses. Additional constraints associated with flow reversal, such as asymmetry in the ebb and flood directions and strengths could be included in the optimization algorithm without any changes to it.

Given a site bathymetry and the number of turbines that can be placed in the channel, the numerical methodology described can be used to propose optimized turbine configuration with minimal computational cost and time. For this sample problem, the optimized configuration was obtained with only two computational meshes and two sets of RANS simulations, with post-processing of the numerical results at each step. However, it should be noted that, in order to obtain the mathematical relation and provide a general understating of the specified turbine design, a computational domain with multiple possible turbine configurations needs to be developed and a large number of simulations run. These simulations develop a "training set" to ob-

tain the simplified constant local efficiency, as the ratio between the available kinetic energy flux and power extractable by the turbine. As mentioned above, this numerical methodology have some limitations similar to other CFD tools, but previous work have shown its adequacy for this problem. Furthermore, in this work it has been shown that this model is a powerful CFD tool to narrow down the complex problem of tidal turbine array optimization process to a small number of possible cases and simulations to finalize the optimization. This work also provides a set of guidelines to propose an optimized array configuration based on site constraints and turbine design.

Chapter 4

SEDIMENTATION IN THE FLOW FIELD OF HORIZONTAL AXIS HYDROKINETIC TURBINES: STUDY OF A POTENTIAL ENVIRONMENTAL EFFECT

One of the main concerns regarding the deployment of hydrokinetic turbines in a tidal site is their potential environmental effects. To understand the importance and uncertainty of the multiple interactions between the MHK installation and the environment, it can be useful to analyze the different aspects with the classification presented by Polagye et al. in [33]. In this framework, every aspect of the presence of a hydrokinetic turbine (i.e. rotating blades, device structure, chemical, acoustics, electromagnetic field, etc.) is defined as a "stressor", and the part of the environment that a hydrokinetic turbine might have an effect on (i.e. near or far wake, habitat, fish and etc.) is defined as a "receptor". Figure 4.1 shows how the correlations between stressors and receptors are categorized in the form of a matrix [33]. In this matrix, the colors represent the level of significance, while the suggested level of uncertainty, is denoted by number and color of the triangles. As an example, a red square with three red triangles inside suggests that the effect of a specific stressor on that receptor might be elevated and its determination has a high level of uncertainty. Therefore, the analysis of this stressor-receptor pair is worth going through a series of in-depth studies. The goal of this investigation would be the examination of the proposed hypothesis about the significance level of a HAHT's potential environmental effect and reduce its degree of uncertainty.

Figure 4.2 shows the stressor-receptor relations for a commercial project. In this figure more than two-third of the matrix cells have a red and yellow background color

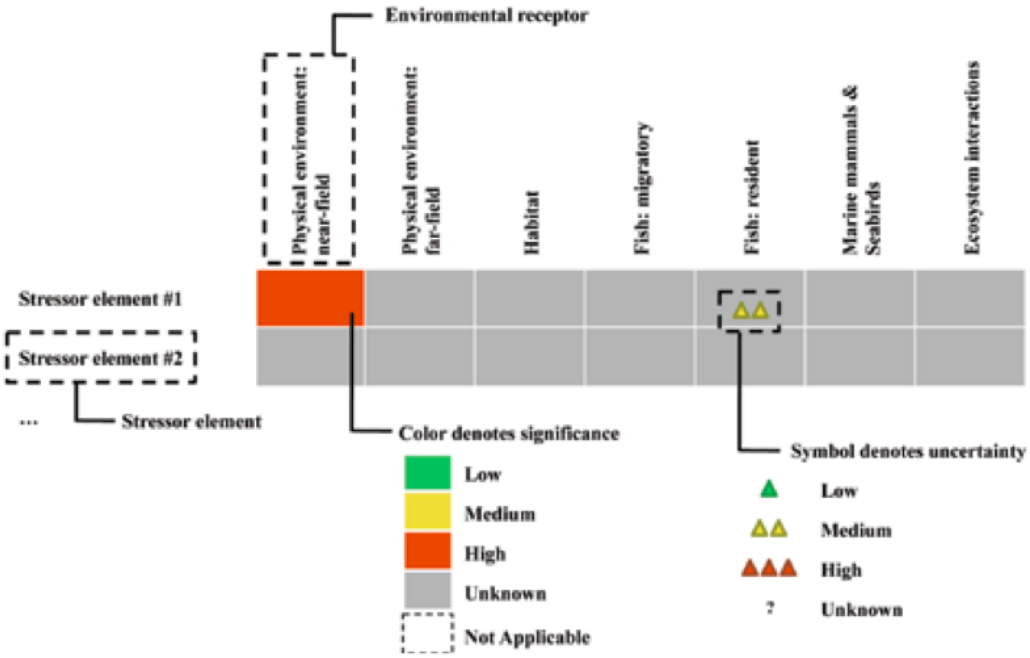

Figure 4.1: **Sample stressor matrix components.**

with red and yellow triangles inside them. This means most of these interactions are important and, due to their high level of uncertainty, they need to be investigated prior to device deployment.

More specifically, figure 4.2 indicates that the static and dynamic effects of the turbine on both the near and far field regions have a moderate to high level of significance and uncertainty. Hence, these relations become important enough to be addressed and investigated. The effects of the turbine structure presence (static effect), and the rotor motion and associated flow field (dynamic effect) on the sedimentation process of suspended particles in the near and far field are good examples of the stressor-receptor interactions. The velocity deficit in the wake of a turbine, due to the energy extraction by the rotor and the presence of the device structure, can potentially enhance the sedimentation process of large particles or affect the dispersion process of smaller suspended particles in a tidal channel. In addition, since hydrokinetic

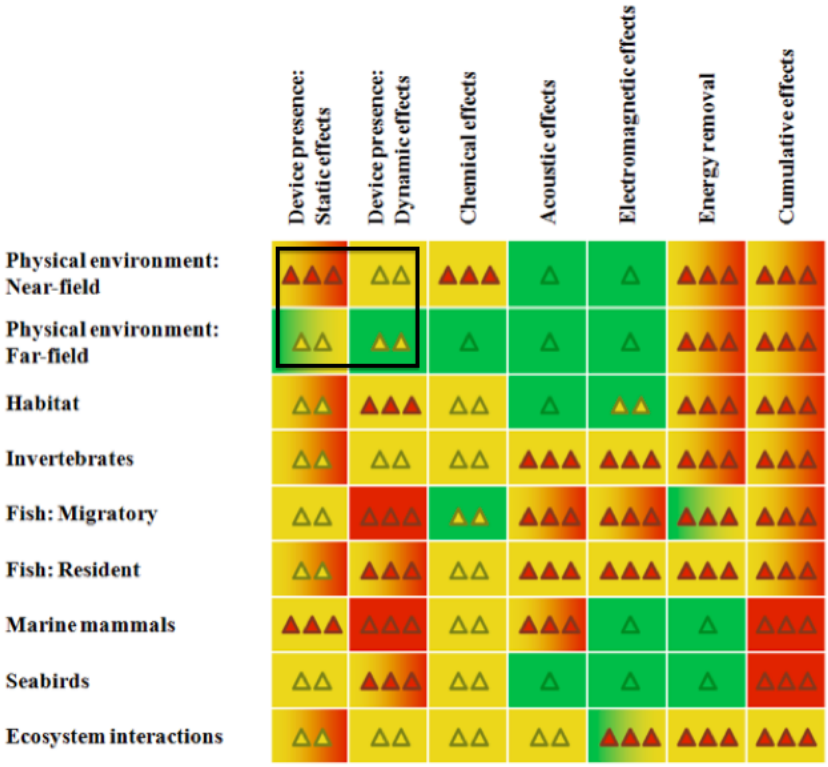

Figure 4.2: **Commercial-scale deployment generalized stressor/receptor significance (on a gradient green = low, red = high) and uncertainty (one green triangle = low uncertainty, two yellow triangles = moderate uncertainty, three red triangles = high uncertainty) [33].**

turbines will operate over decades, the consistency of the velocity deficit effect on sedimentation process of relatively small size particles can result in net bathymetry changes. Additionally, the clearance flow induced between the rotor in the lowest part of its trajectory and the tidal channel bottom can result in long-term scouring by re-suspension of relatively small size particles.

The uncertainty in the evaluation of this potential environmental effect is an open question on the path of permitting for installation hydrokinetic turbines. Therefore, in

this study we will use the numerical methodology we have developed to investigate the HAHT-sediment interaction. In this chapter, we first present the theory and describe the uncertainty in the numerical model for particle dispersion in a tidal channel. We then introduce a general calibration methodology for the model used to compute the particle paths. This calibration is designed in response to significant overprediction of particle dispersion in the model, reported in the literature. The model calibration is validated with classical experiments in the literature and shown to match particle dispersion in the homogeneous isotropic turbulence region in the tidal channel without turbines. Using the calibrated model, we investigate the effect of the operation of a hydrokinetic turbines on sedimentation and the dispersion process of particles with different Stokes numbers.

4.1 Numerical Model Review

Particle motion in turbulent flows has extensive applications in environmental and industrial fluid mechanics. Sediment transport and deposition in meandering rivers [79] and tidal channels, particle sedimentation, and solids separation in sewer detention tanks or sewer overflow chambers [51, 52], particle dispersion in turbulent boundary layers or turbulent multiphase mixing layers [40, 46], and particle dispersion in stirred reactors or fluidized bed gasifier [50, 65], are just a few examples of applications where the fluid mechanics of particle-laden turbulent flows dominate the physical behaviour of the system. As a result of this wide range of applications, there is significant interest in understanding and modeling particle dispersion mechanisms in various types of turbulent flow fields.

During the last four decades, different computational models for simulation of the particle dispersion mechanism in turbulent flows have been developed. The majority of these models are based on either Eulerian or Lagrangian approaches for the dispersed phase. In Eulerian models, the continuity and momentum equations for each phase, or for the particulate phase and for the overall fluid mixture, are con-

sidered. Terms that account for the interfacial mass and momentum transfer, need to be implemented. Particle dispersion coefficients are calculated based on a local equilibrium between the fluid and particle dynamics. These models typically require empirical factors to compute interfacial effects, and to improve the accuracy of the calculations [41, 54, 55]. On the other side of the spectrum, in models based on the Lagrangian approach, particle dispersion is modeled by using the equation of motion for an individual particle in the flow, and averaging the behavior of the entire population. Particle trajectory is predicted by integrating the force balance on each particle at each time step during the particle residence time in the flow. This direct calculation of particle trajectory in the flow makes these type of models more accurate and less dependent on empirical constants and corrections [45, 57, 60, 63, 73, 81], although numerically more costly, as the number of degrees of freedom skyrockets with particle volume fraction (count).

Within this Lagrangian approach to particle motion, one of the most widely used models to simulate particle dispersion in a turbulent flow is the Discrete Random Walk (DRW) model. The DRW is a stochastic model first proposed by Hutchinson et al. [60]. Dukowicz [63] developed statistical averaging for the DRW to model liquid droplet dispersion in a turbulent flow. Later on, the DRW was developed into its current form by Gosman and Ioannides [57], who modeled the particle-eddy interaction based on an approach different to Dukowicz: in this new approach, the flow field solution is obtained from a $k-\epsilon$ RANS simulation and the particle trajectories are predicted by modeling their interaction with randomly-generated eddies that fit the statistics of the turbulence, velocity component Root Mean Square (RMS) and lifetimes, as predicted by the turbulence model. Once the relative velocity between the particle and the fluid is computed based on the appropriate eddy velocity and time scale, the dynamics of the particle are integrated based on the hydrodynamic forces (drag, lift, added mass, etc.) that result from the particle-fluid relative velocity and acceleration[69].

The characteristic eddy time scale, used to simulate particle dispersion in a turbulent flow, depends on the value of a constant coefficient that needs to be set, within a wide range. While some guidelines based on experimental data exist, there is no process to set this constant value rigorously. In a comprehensive review of the DRW model history, Milojević states, regarding the choice of the constant time scale coefficient, that: "All of the above mentioned researchers reported good agreement of their predictions [their results from the DRW model] with available experimental data, even though they used different values of the coefficient C_T [constant time scale coefficient]. This can lead to a wrong conclusion that this coefficient does not have a significant influence on the particle dispersion. The influence of C_T is very strong and results from the basic theory given by the dispersion equation" [49]. This highlights the importance of the choice of the value for the time scale coefficient in the DRW model, and the wide range of values that need to be used to adequately represent dispersion in different turbulent flows of varying characteristics.

Previous work that proposed different versions of the DRW model [45, 57, 73, 81] calibrated the value of the constant time scale coefficient C_T against specific experimental datasets by Snyder and Lumley [82], Wells and Stock [87] and Arnason [55]. These calibration processes led to different time scale constants, C_T, within a range between 0.135 to 0.41. In some recent studies, the time scale coefficient was tuned based on a direct comparison between experimental and numerical results of the same case study [40, 84], although this information is typically not available in applications where CFD seeks to complement experiments, in a parameter range not overlapping with them. Typical default values of the time scale coefficient in commercial CFD packages is $C_T = 0.3$ *. While this value lies in the above-mentioned range, it has led to multiple observations of overestimation and uncertainty in dispersion of particles

*In ANSYS FLUENT the constant time scale coefficient is denoted by C_L. Based on FLUENT formulation of the DRW model, the equivalent value of C_T would be $2 * C_L$. Therefore, the value recommended by FLUENT's manual of $C_L = 0.15$ is equivalent to a value of 0.3 for C_T.

in a turbulent flows [40, 46, 51, 52, 74, 79]. As a result, it has become clear in the literature from studies of dispersion using the DRW model that particle-eddy interactions, and therefore particle dispersion in a turbulent flow, depends too critically on the value of the constant time scale coefficient C_T chosen. Using the default value based on a specific previous work, that contains different characteristics of the carrier turbulence, leads to poor dispersion results with large overestimations of the effect of turbulent diffusion, particularly for cases in which the particulate phase has little inertia and crossing trajectories (small Stokes numbers and terminal velocity ratios) and their trajectories are dominated by the interactions with the eddies in the carrier flow.

The use of DRW for particle dispersion calculations based on flow fields computed from the solution of the RANS equations, requires a method to set the time scale coefficient C_T to a value that is sensitive to the properties of the turbulence in the carrier flow as modeled by the specific RANS solution under study. This variable affects the modeled dispersion results in a disproportionate way, and has hindered the use of this model in real world applications. The calibration process needed to set this value for a specific application conditions can, and should, be based on experimental data to compare with the simulated dispersion. But in many real-world applications, experimental data many not be available, or may only be available for small scale (low Reynolds numbers) and simplified geometry cases. In these cases, where the characteristics of the turbulence can be assumed to approach homogeneous, isotropic turbulence, we propose that the calibration to find the right value of the eddy time scale coefficient can be performed against a fundamental theoretical relationship for fluid particle dispersion, G.I. Taylor's dispersion theory [56]. This will help improve the accuracy of the DRW model dispersion predictions, by overcoming the uncertainty in the choice of value for this critical time scale coefficient, C_T.

4.2 Discrete Random Walk (DRW) Model Theory

The Discrete Random Walk (DRW) model is a stochastic numerical scheme used to simulate particle dispersion in a turbulent flow. This model is based on the Lagrangian approach where individual particles are tracked based on their equations of motion under fluid and other external forces. A fundamental assumption made in this model is that particles interact with the fluid, but not with each other (one or two-way coupling) [53]. This assumption is generally valid in the low volume (and mass) fraction limit for the particulate phase, where inter-particle distances are much larger than the diameter and collisions are statistically insignificant. The implementation of the DRW model relies on hydrodynamic forces calculated along the particle trajectories (at the center of mass of each particle in the commonly-used point particle approximation). This requires a statistical description of the carrier flow turbulent field as modeled, for example, by solving the RANS equations with a turbulence closure.
The equation of motion of a particle equates the particle inertia with the hydrodynamic, and other external, forces acting on the particle as follows:

$$\frac{d\vec{V_p}}{dt} = \vec{F_D}\ ((\bar{\vec{V}} + \vec{V'}(t)) - \vec{V_p}) + \frac{\vec{g}(\rho_p - \rho)}{\rho_p} + \vec{F_x}. \tag{4.1}$$

In eq. 4.1 the variables with the "p" subscript refer to the particle variables and those without subscript refer to the variables of the carrier flow. Here, $\bar{\vec{V}} + \vec{V'}(t)$ are the mean velocity plus the velocity fluctuations, ρ is the density and $\vec{g}$ is the gravitational acceleration. In this equation, the first term on the right hand side of the equation is the drag force per unit particle mass, the second one is the gravitational force and the third term accounts for additional forces in the flow (i.e. added mass, Basset history, Saffman's lift, phoretic forces, etc.). The DRW model predicts the turbulent dispersion of particles using the instantaneous fluid velocity $\bar{\vec{V}} + \vec{V'}(t)$, along the particle path during the integration of the forces on the particle. In this formulation,

the fluctuating velocity components are discrete piecewise-constant functions of time:

$$u' = \gamma_1 \sqrt{\overline{u'^2}}, \qquad v' = \gamma_2 \sqrt{\overline{v'^2}}, \qquad w' = \gamma_3 \sqrt{\overline{w'^2}}. \tag{4.2}$$

Here, it is assumed that the fluctuating velocity components obey a Gaussian probability distribution, where "γ_x" are zero-mean, unit-variance, normally-distributed, random numbers. The values of γ_x are computed from a random number generator, and kept constant over an interval of time given by the interaction time scale (our subject of investigation). The other terms on the right hand side of the above equations are the local Root Mean Square (RMS) values of the velocity fluctuations in x, y and z directions, respectively. Assuming that the turbulence flow is isotropic and knowing the kinetic energy of turbulence at each point in the flow, RMS values can either evaluated directly when the Reynolds Stress turbulence model is used or can be defined as:

$$\sqrt{\overline{u'^2}} = \sqrt{\overline{v'^2}} = \sqrt{\overline{w'^2}} = \sqrt{2k/3}. \tag{4.3}$$

The main challenge for obtaining accurate results in this standard implementation of the DRW model is the adequate calculation of the eddy lifetime, that is, the frequency with which the velocity fluctuation components are updated as particles move in the turbulent flow field. This time scale is defined based on two possible particle-eddy interaction scenarios: a) the particle interacts with a given eddy till that eddy diffuses away (after its lifetime, a random variable with mean (τ_e), has passed). At that point, the particle will start interacting with a new eddy (randomly generated in terms of both its strength and lifetime) and the flow velocity fluctuations the particle experiences change. This eddy-particle interaction time, which corresponds to the eddy Lagrangian correlation time, is computed in the DRW model as:

$$\tau_e \approx C_T \frac{k}{\epsilon}. \tag{4.4}$$

where C_T is the constant time scale coefficient at the heart of the problem investigated here, k is the turbulent kinetic energy and ϵ is the turbulent dissipation rate. The

alternative particle-eddy interaction time, scenario b), represents interactions in which the particle crosses, due to inertia or gravitational pull, through an eddy in a time $t_{cross}(< \tau_e)$. The particle will then encounter another eddy and experience different velocity fluctuations. This particle-eddy interaction time scale can be computed as:

$$t_{cross} = -\tau_p \; ln[1 - (\frac{L_e}{\tau \; |\vec{V} - \vec{V_p}|})], \tag{4.5}$$

where τ_p is the particle relaxation time, L_e is the eddy length scale, and $|\vec{V} - \vec{V_p}|$ is the magnitude of the relative velocity, given by the gravitational settling velocity in the case of the crossing trajectories effect.

Based on this phenomenology, the particle-eddy interaction time is the minimum of two times: the eddy life time (τ_e) and the eddy crossing time (t_{cross}) [43]. For low inertia particles, the eddy-crossing time is typically long and, therefore, the value of the eddy life time (influenced by the coefficient C_T) plays a dominant role in computing dispersion. Inaccurate values of this constant will lead to gross under- or overestimation of particles dispersion process, as reported widely by practitioners, [40, 46, 51, 52, 74, 79]. Hence, C_T needs to be fine-tuned based on experimental comparison or theoretical considerations, for the actual turbulent carrier flow under study.

4.3 Discrete Random Walk (DRW) Model and Uncertainty Reported in the Literature

Preliminary research on the dispersion of sediment particles in a large scale tidal channel ($Re \approx 40 \; 10^6$) confirms the phenomenon of overestimation of dispersion, reported in 4.1. As an example of the difficulties that arise from the use of default parameters in the DRW model, the simplest possible case of particle dispersion in a square cross-section turbulent channel was modeled using the DRW model coupled with RANS simulation. Fluid elements are injected at a point source at the inlet of the channel with a streamwise flow. Figure 4.3 shows the trajectories for 500 independent

realizations of fluid elements injected at a certain point. As shown in figure 4.3 by the

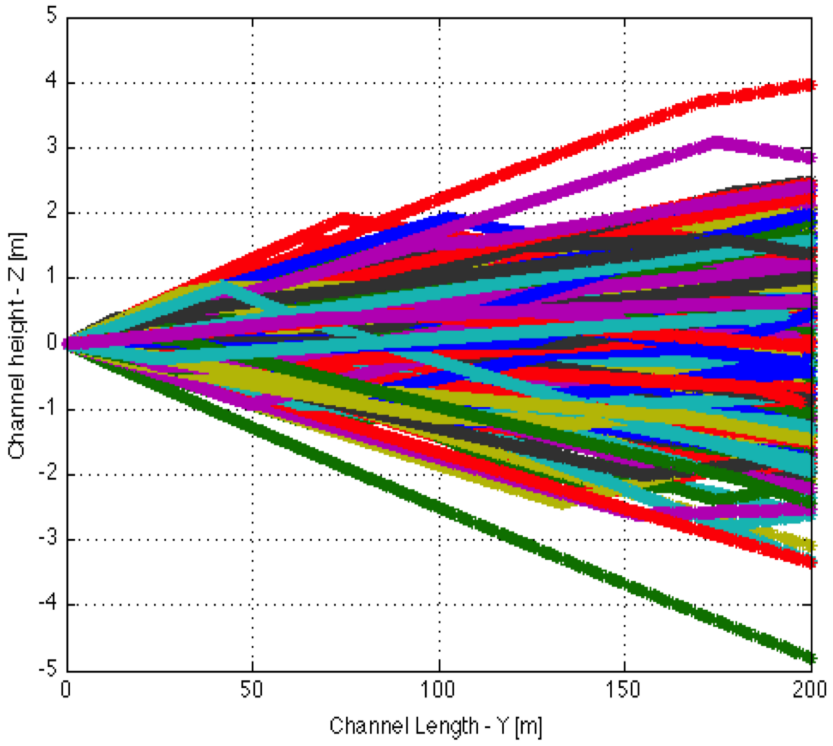

Figure 4.3: **Trajectories in 500 realizations of fluid element dispersion in a turbulent channel. The DRW model was used to compute the particle-eddy interactions, with the default recommended time scale constant** $C_T = 0.3$**.**

different color paths, in most realizations, particles interact with a single eddy for their entire residence time in the 200-m long channel. The trajectories show persistence in their slopes well beyond what would be expected in a turbulence flow with no mean vertical velocity. As an example, if we focus our attention on the dark green line that ends at the bottom right, we can see that it started its trajectory interacting with an eddy (that happens to have a relatively high negative vertical velocity) and continues

to interact with the same eddy for about 100 s. In other words, the fluid elements are being "shot-out" from the injection point by individual eddies, instead of being continuously dispersed in the flow field by the ensemble action of the turbulence. The Lagrangian autocorrelation time scale, as seen by the particles, is defined as:

$$I = \lim_{t\to\infty} \int_0^t \mathrm{R}_\zeta \, \mathrm{d}\zeta. \tag{4.6}$$

and can be computed from the RANS solution. In this equation, R_ζ defines the correlation function between the value of fluid velocity fluctuation at the particle location at any instant time t and the value of velocity at the particle location after an interval of time ζ

$$R(\zeta) = < u(t)u(t+\zeta) > / < u(t)^2 > . \tag{4.7}$$

Figure 4.4 shows the autocorrelation function based on the modeled velocity fluctuations via the DRW model (using the default timescale coefficient, $C_T = 0.3$). The decay of the autocorrelation in this case does not correspond to the values in previous experimental and theoretical analysis [75].

The calculations show that the particle-eddy interaction time, τ_{DRW}, averaged for all realizations is 41.04 s. However, the integral of the Lagrangian velocity autocorrelation function (eq. 4.6) is 19.63 s. Therefore, the default value of the timescale parameter, $C_T = 0.3$, yields an averaged time scale for the DRW particle analysis that is about two times the theoretical one. The basic assumptions behind the model and the use of the eddy time, based on turbulent kinetic energy and dissipation rates related by C_T, for particle dispersion are not satisfied.

Clearly, the use of the default value of the time constant, although well within the wide range obtained by calibration against a few classical laboratory experiments in the literature, produces non-physical results in terms of both the dispersion of particles, even fluid elements, and in the Lagrangian correlation time of the turbulent velocity. Hence, the value of this model parameter, C_T, can not be assigned blindly

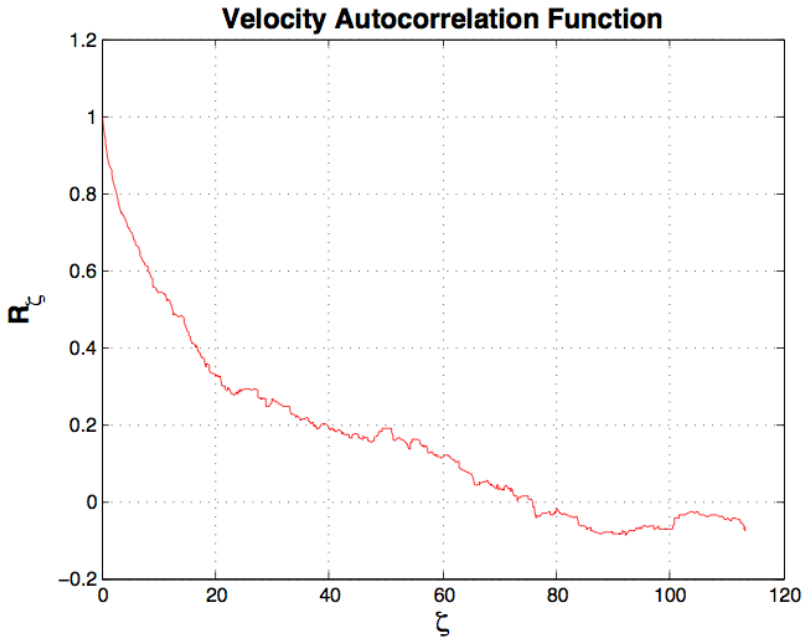

Figure 4.4: **Lagragian autocorrelation function from the DRW model with the default timescale coefficient $C_T = 0.3$.**

based on some lower Reynolds number data that may not share critical features with the flow field under study. It needs to be set according to the specific characteristics of the actual turbulent flow investigated.

4.4 Discrete Random Walk (DRW) Model Calibration Methodology

Ideally, experimental data on the flow of interest would be available for calibration, but the reality is that this is seldom the case. A calibration procedure is proposed based on classical theoretical results for high Reynolds number flows where diffusion in homogeneous isotropic turbulence is the dominant effect controlling the dispersion of particles.

To compute an adequate value of the time-scale coefficient, the dispersion of fluid

particles in a turbulent flow is numerically simulated. A large number of realizations of particle trajectories, sufficient for statistical convergence, are computed with the DRW model, and this process is repeated using different values of the particle-eddy interaction time scale constant (C_T). The statistics of the position of particles, particle and fluid velocities and time scale (minimum value between the eddy lifetime and eddy crossing time) experienced by the particle at the each time step, are stored. The numerical values of the particle-eddy interaction time, τ_{DRW}, are averaged over all realizations in the DRW model (for each value of C_T used) to calculate the characteristic time scale for the turbulent flow of interest. Using the particle-sampled fluid velocity data, the Lagrangian integral correlation time scale, T, can also be calculated from its definition, equation 4.6. Comparison between these values of time scales, numerical and theoretical, for various choices of time scale constant (C_T) will provide a basis for the appropriate range of values for C_T. The C_T values that minimize the difference between the predicted numerical correlation time scale and theoretical correlation time scale are the candidates for the appropriate time scale constant for the turbulent flow of interest. Further, the root mean square of the particle displacements simulated by the DRW model provides a measure of particle dispersion. This quantity, or its components in the x, y, and z directions, can also be calculated from Taylor's dispersion theory [56] based only on the turbulence intensity, known a priori at the inlet of computational domain and computed by the RANS closure at each location in the flow field:

$$\sqrt{[X^2]} = \sqrt{2 * I * t} * \sqrt{[u^2]} = \sqrt{2 * I * t} * (T.I. * \bar{U}). \tag{4.8}$$

This prediction from Taylor's theory for the dispersion in particle paths is proportional to the square root of the Lagrangian velocity correlation time (T), to the square root of the particle residence time (t) and to the RMS of particle velocity fluctuations [56]. This approximation is valid for large residence times, when the initial effect of the turbulence right after injection (large dispersion that grows linearly with time) has

ended and yielded to long term effects. Comparison between the numerical and theoretical results for the averaged particle dispersion predicted by the DRW model, by iteration between the candidate values of time scale constants (C_T) obtained from previous step, and calculated using Taylor's theory allows for the fine-selection of the value for the time scale constant C_T for the turbulent flow of interest. In other words, an optimum value of the DRW parameter C_T is identified when the difference between the time scales, T and τ_{DRW} is minimal and the differences in the average particle dispersion predicted by the model and the theory are also minimum.

It should be emphasized that the goal of this calibration methodology is to reduce the significant uncertainty that currently exists for the choice of the time scale constant (C_T) for large scale flows with very high Reynolds number when no experimental data is available to select this constant. As discussed earlier in Section 4.1, the value of C_T is known only for small scale turbulent flows for which well-established experimental data is available. However, for large scale high Reynolds number flows, in the absence of experimental data, the default time scale constant (C_T) might result in to poor numerical predictions. This methodology sets a base value of C_T for the DRW model under a fundamental turbulent flow related to the one of interest, by guaranteeing that the model predicted dispersion would match Taylor's theory. This would significantly reduce existing errors in numerical particle dispersion in complicated flow fields, that lead to the common occurrence of overprediction of turbulent dispersion by the DRW model coupled with RANS simulations.

4.5 Experimental Validation of DRW Model Calibration Methodology

To demonstrate the validity of the calibration methodology for the DRW model described in section 4.4, a comparison with experimental measurements is presented in this section. In order to apply the methodology and compare results, the turbulent flow field in the test section of the experimental wind tunnel is numerically simulated by solving RANS equations, with the SST k-ω turbulence closure model,

under the conditions described by the authors. The geometry, mesh resolution and boundary conditions of the computational domain in the RANS simulation were created to match the experiment flow field, based on the methodology by Rybalko et al. [77]. Values of turbulent kinetic energy, k, and turbulent frequency, ω, at the inflow of the computational domain, not provided explicitly in the paper, were chosen as $k = 0.35\frac{m^2}{s^2}$ and $\omega = 425\frac{m^2}{s^3}$ in order to provide the closest match to the profiles of turbulent kinetic energy and dissipation rates inside the wind tunnel. Figure 4.5 shows comparisons between the numerical (red) and experimental (blue) decay of turbulent kinetic energy, k, and dissipation rate, ϵ, on the centerline of the domain along the channel length. In these plots, the channel length is normalized by the turbulence-generating grid spacing (M). As shown in these two plots, except for a slight disagreement between the measured and predicted turbulent dissipation rate for $\frac{x}{M}$= 60 to 80, the overall experimental and numerical results show good agreement.

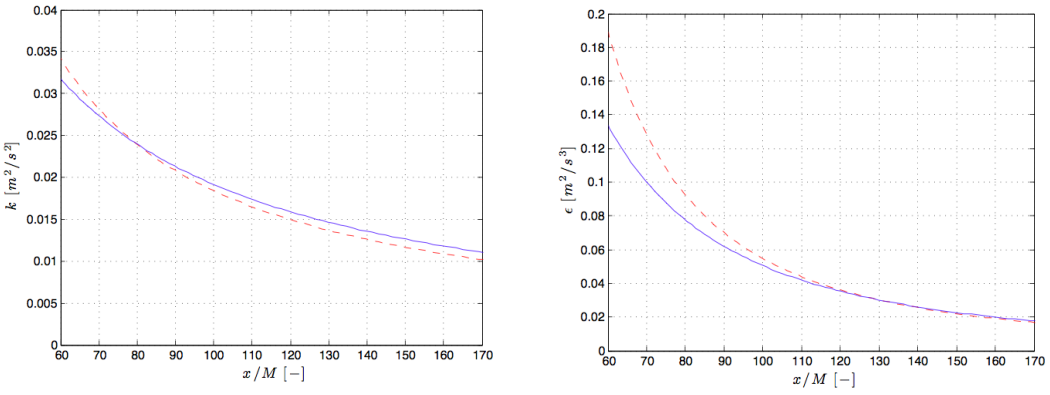

Figure 4.5: **Comparison between the numerical (blue) and experimental (red) results for the decay of turbulent kinetic energy k (right) and turbulent dissipation rate ϵ (left) on the centerline along the length of test section normalized by the turbulence-generating grid spacing (M).**

Once the turbulent flow field of the experiment has been successfully modeled using RANS simulation, the particle dispersion measurements were compared to the DRW model predictions. Among the different particles used in the experiments, the two ends of particle inertia, hollow glass particles (close to flow tracers) and solid copper particles, were chosen for this experimental comparison. The injection condition in the experiment was matched in the simulation. The DRW model with default time scale constant parameter, $C_T = 0.3$, was used to simulate particle dispersion of hollow glass and copper particles. Figure 4.6 presents a comparison between the experimental (black symbols) and numerical results (red) for hollow glass spheres and solid copper. As particles' Stokes number increases, from hollow glass to solid copper, the RMS of particle lateral dispersion decreases. As shown in figure 4.6 for both particles, the DRW model with default time scale constant does over-predict the particle dispersion compared to the corresponding experimental values. This confirms our previous hypothesis that a default time-parameter value can not be a good one-size-fits-all solution for dispersion problems. Even for these conditions, relatively close to the ones used to set the default value, the results are underwhelming. When the turbulent characterization of the flow, Reynolds number and eddy length scale, changes by orders of magnitude from those lab conditions used to set the default value, the predictions using it drift significantly more, as shown in the previous discussion on the uncertainty of the DRW model to simulate particle dispersion in a large scale channel flow with very large Reynolds number (see section 4.3), making the calibration process for the model parameter even more critical. In the absence of experimental data, the method proposed here, based on Taylor's turbulent dispersion is a theory-supported alternative.

At this stage, the calibration methodology explained in section 4.4 is applied to the DRW model used to simulate the Snyder-Lumley experiment. Using the simulation data, the numerical correlation time scale (τ_{DRW}), averaged over all realizations, and the theoretical Lagrangian integral correlation time I (eq. 4.6) is calculated. Values

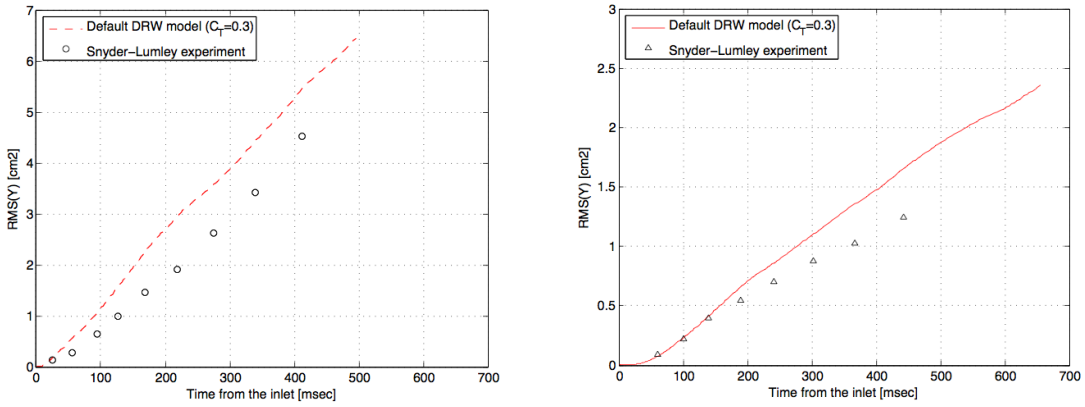

Figure 4.6: **Comparison between the experimental (black symbols) and numerical (red line) results from default DRW model for RMS of particle lateral dispersion of the hollow glass (right) and solid copper (left).**

of these two time scales for different values of C_T are presented in table 4.1. A comparison between these values indicates that a suitable range for C_T is in the interval of 0.15-0.3. The averaged particle dispersion computed with C_T values between 0.15 and 0.3 is compared to Taylor's prediction in figure 4.7.

Plots in figure 4.7 show the comparison between the RMS of fluid element displacement predicted by Taylor's theory (in red) and the DRW model (in blue) using different values of time scale constant, C_T. The abscissa represents the fluid element residence time after injection into the domain and the ordinate shows the RMS displacement with respect to the freestream "laminar" trajectory. A value of $C_T = 0.2$ for the time scale coefficient was selected to minimize differences between the predictions of particle dispersion (shown in top right plot of figure 4.7).

The two plots in figure 4.8 show the comparison between calibrated DRW results and the Snyder-Lumley experimental results for the RMS of lateral dispersion of hollow glass and copper particles. Comparison between plots (a) of figures 4.6 and 4.8

C_T	τ_{DRW}	I
0.60	0.071	0.047
0.30	0.037	0.016
0.2	0.025	0.015
0.15	0.020	0.009
0.075	0.027	0.008

Table 4.1: **Comparison between values of the estimated averaged eddy-particle interaction time scale with DRW (τ_{DRW}) and the calculated integral time scale from velocity correlation values (I).**

reveals that the methodology for calibration of the value of the time-scale coefficient C_T leads to a excellent agreement between DRW prediction and corresponding experimental data, much better than for the default value of the coefficient. The effect of time scale constant calibration for copper solid particles was very similar to the hollow glass particles. Since in this case the Stokes number of particles was increased, particles inertia played a more important role on their dynamics, leading to lower particle dispersion and a small overestimation of particle dispersion by the model based on tracer particles.

Since the default value of the DRW time-sale constant, $C_T = 0.3$, was originally based on lab-scale experimental data, including Snyder & Lumley's, the optimum value of the time scale constant changed significantly but modestly, $\approx 30\%$. However, this confirms the fact that, even for this experimental data, part of the database used to set the default value for C_T, the calibration procedure has ample room to reduce the error in the numerical modeling of dispersion. For larger scale, high Reynolds number turbulent flows, the application of calibration methodology leads to changes of the time-scale values of an order of magnitude (up to $\approx 94\%$).

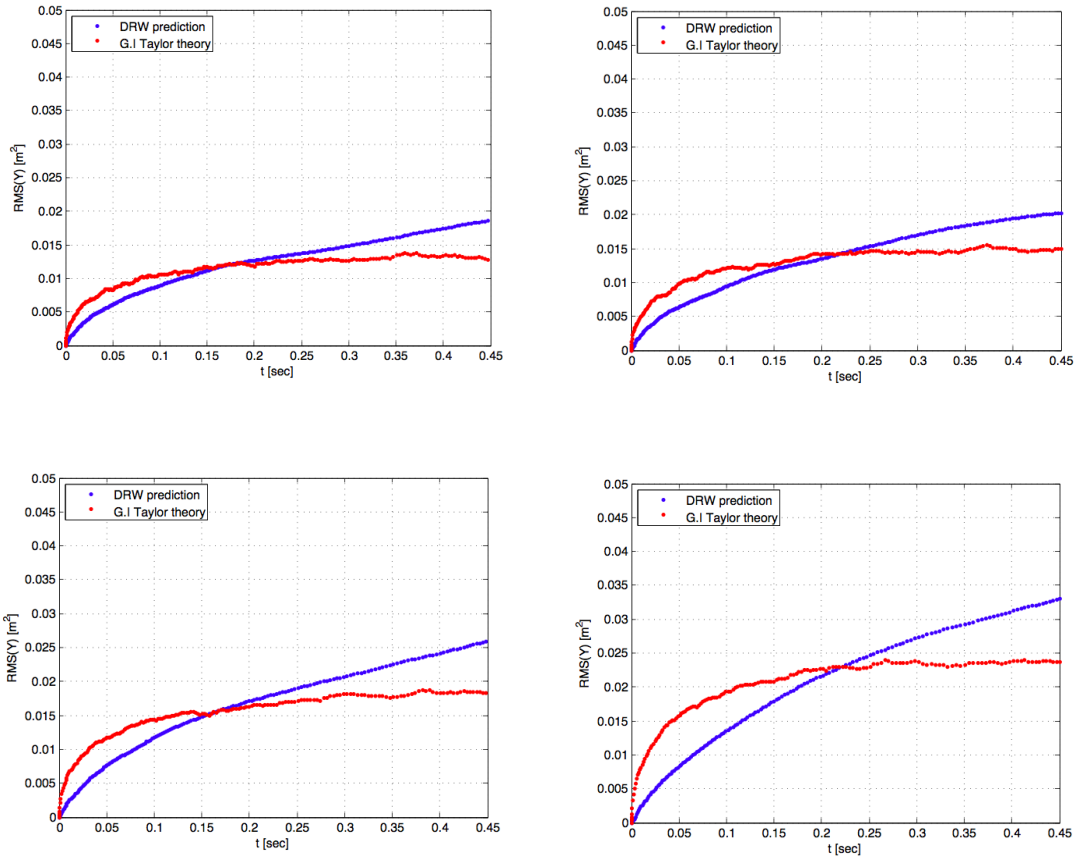

Figure 4.7: **Comparison of fluid element displacement RMS, in the lateral direction, from Taylor's dispersion theory (red) and the DRW model (blue), using the different value of the eddy life time constant C_T=0.15 (top left) , 0.2 (top right) , 0.3 (bottom left) and 0.6 (bottom right).**

4.6 DRW Model Calibration Methodology Application to Particle Dispersion Simulation in a Large Scale Tidal Channel.

As discussed earlier, an application of the calibrated DRW model is the study of the interaction of HAHTs and sediment in a tidal channel where no detailed experimental data is available to compare against. An example of the calibration process for the

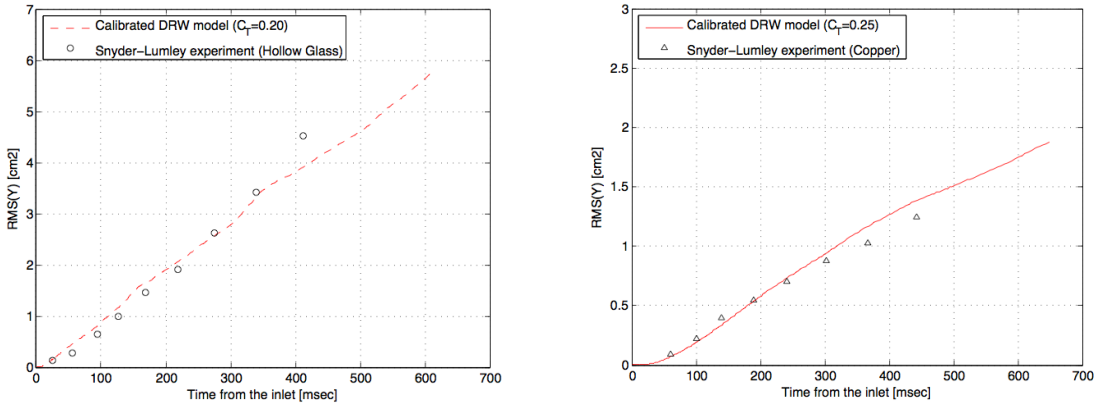

Figure 4.8: **Comparison between the experimental (black symbols) and numerical (red line) results from calibrated DRW model for RMS of particle lateral dispersion of the hollow glass (right) and solid copper (left).**

DRW model application is in the investigation of particle dispersion in a large scale tidal channel. To numerically model the particle dispersion accurately in a turbulent channel flow, the DRW model is coupled with the RANS-simulated flow field inside the channel. In addition to the discussion presented in Section 4.3, to highlight the need for calibration of the DRW model in this specific application, the mean dispersion of the fluid elements modeled by DRW are compared against and that calculated based on Taylor's dispersion theory. Figures 4.9 - 4.11 show the comparison of mean particle dispersion predicted by Taylor's theory (in red) and results from the DRW model (in blue). The horizontal axes represent the fluid element residence time after injection and the vertical axes show the RMS displacement with respect to the freestream "laminar" trajectory, in all three directions along the channel. The comparison between the plots in figures 4.9 - 4.11 reveals a significant overestimation of the dispersion process when it is simulated by the DRW model using the default value of the eddy time scale constant ($C_T = 0.3$). This observation confirms the relevance

to the tidal channel environmental assessment of the discussion in Sections 4.1 and 4.3 on the difficulties of the DRW model to compute dispersion in highly turbulent flow field regimes. To overcome this problem, the DRW model needs to be calibrated for this application.

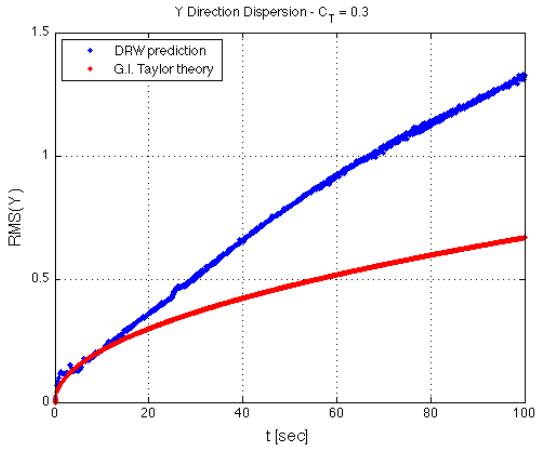

Figure 4.9: **Comparisons of estimated averaged particle dispersion path in Y-direction via the DRW model with time scale constant $C_T = 0.3$ (blue) with predicted particle path based on Taylor's dispersion theory (red).**

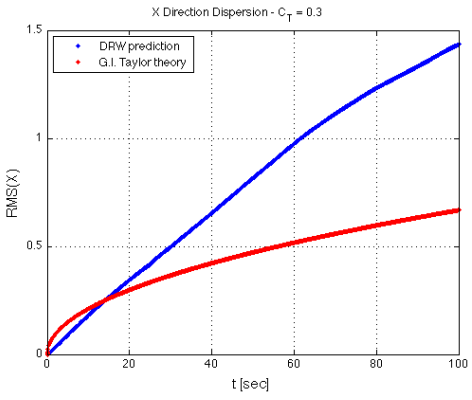

Figure 4.10: **X-direction dispersion.**

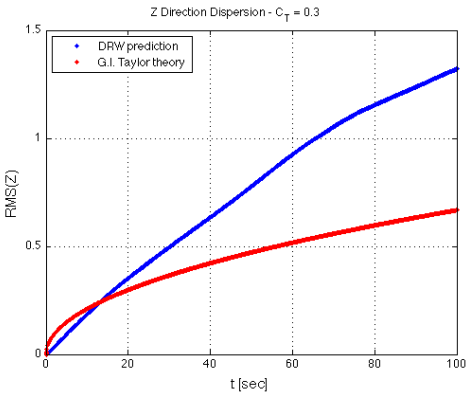

Figure 4.11: **Z-direction dispersion.**

To apply the calibration methodology to this case of particle dispersion in large scale turbulent channel flow, the numerical and theoretical time scale constants were calculated for different choices of C_T, as described in Section 4.4. Table 4.2 compares the numerical and theoretical values of time scale for different C_T values. This comparison shows that a C_T value in the interval between 0.01 and 0.03 would minimize the difference between the two time scales (τ_{DRW} and I).

C_T	τ_{DRW}	I
0.30	41.04	19.63
0.20	28.63	16.24
0.10	6.83	15.35
0.03	4.72	3.24
0.02	3.76	3.14

Table 4.2: **Comparison between values of the average eddy-particle interaction time scale with DRW (τ_{DRW}) and the calculated integral time scale from velocity correlation values (I).**

Figure 4.12 shows the velocity autocorrelation function for a value of the time-scale parameter $C_T = 0.02$. The integral Lagrangian time scale from this function (I) is equal to 3.76 s, while the average eddy-particle interaction from the ensemble of particle trajectories in the simulation for that value of the parameter is $\tau_{DRW} = 3.14$ s. The comparison with figure 4.4 shows the enormous modification in the shape of the autocorrelation function as further qualitative evidence of the important overprediction in the eddy interaction time when using default values, and the need for the calibration procedure proposed here for the DRW. More consistent values of the eddy interaction time scale, chosen to match theoretical results under idealized but close-to-application conditions, greatly improve the prediction of particle dispersion

in complex flows simulated with a combination of RANS solver and DRW particle dynamics.

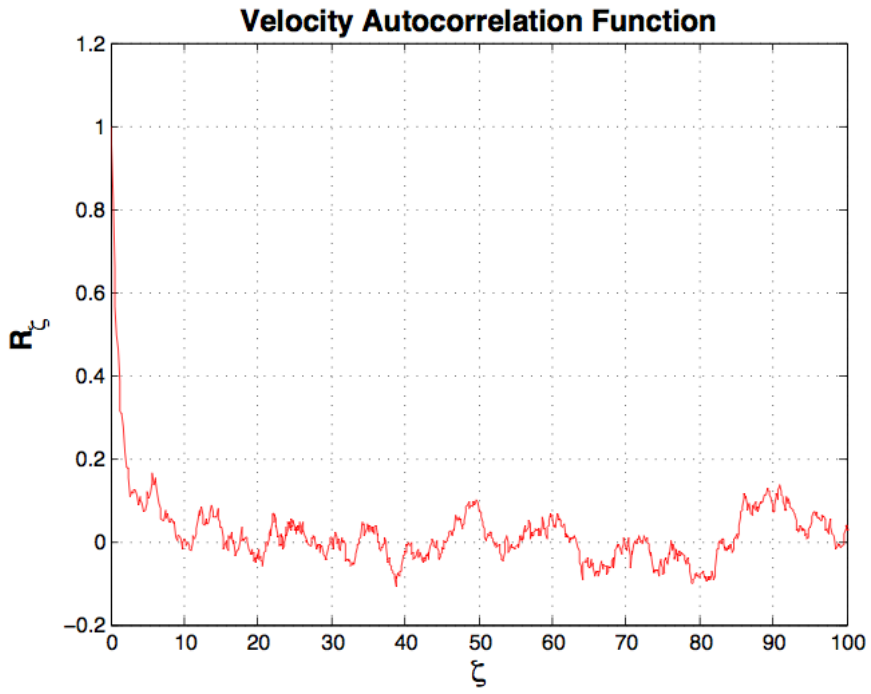

Figure 4.12: **Estimated autocorrelation function via the DRW model with the recommended time scale constant** $C_T = 0.02$**.**

Figure 4.13 shows the dispersion process is accurately predicted by the DRW with the optimum value of the eddy time scale constant of $C_T = 0.02$. A brief note must be made to the implementation of the method for very short times, in the direction of the free stream velocity (the Y-axis in our frame of reference), where a small but noticeable error is present due to overestimation of the slip velocity in the interaction with the first eddy. This short term effect, which comes from a known bug in the commercial code and is purely numerical, does not affect the long time dispersion used as a benchmark in the calibration.

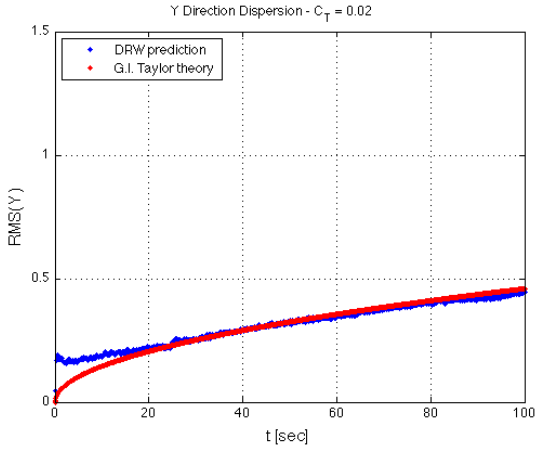

Figure 4.13: **Comparisons of estimated averaged particle dispersion path in Y-direction via the DRW model with time scale constant $C_T = 0.3$ (blue) with predicted particle path based on Taylor's dispersion theory (red).**

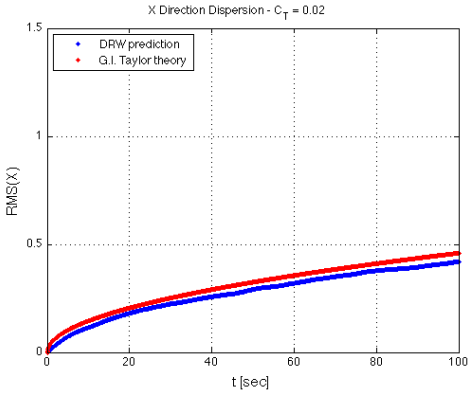

Figure 4.14: **X-direction dispersion.**

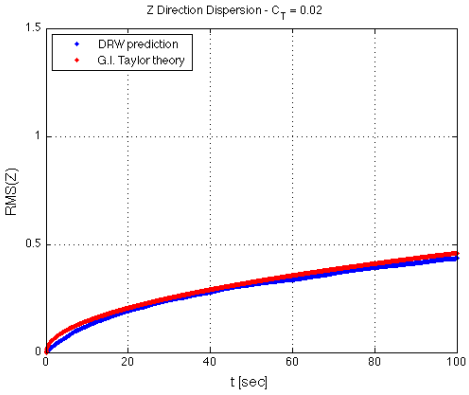

Figure 4.15: **Z-direction dispersion.**

Particle trajectories injected at a point and dispersed by turbulence are shown in figure 4.16 for the calibrated value of the DRW time scale parameter $C_T = 0.02$. As opposed to the equivalent result with the default time scale parameter value ($C_T = 0.3$), shown in figure 4.3, the particle-eddy interactions now last for a few seconds, up

to tens of second, producing a continuous diffusion process of the trajectory of each individual particle. The ensemble effect is a more gradual, moderate, effect without the high persistence, high sloped, extreme trajectories that result from the particles interacting with the same large eddy for their entire residence time in the flow. As a result, the square root dependency on turbulence intensity, integral time scale and residence time are recovered. This consistency is confirmed by the results from the Lagrangian velocity autocorrelation function obtained with the calibrated DRW time parameter.

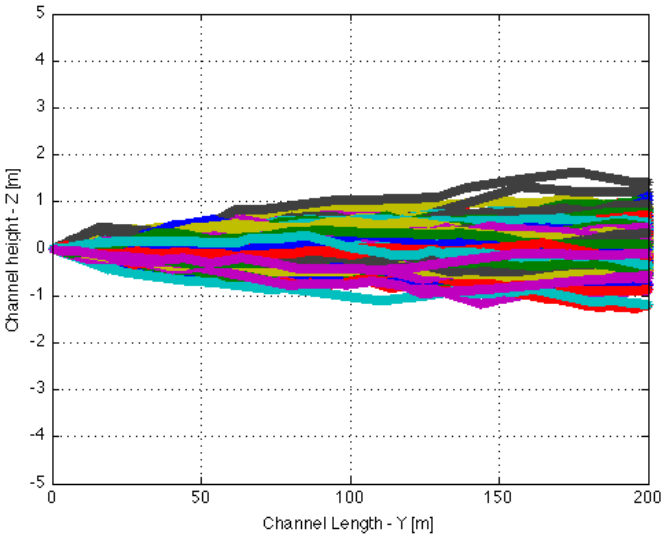

Figure 4.16: **Simulated 500 realizations of fluid element dispersion in a tidal channel (no MHK turbine operating). DRW was used with the recommended time scale constant** $C_T = 0.02$**.**

4.7 Numerical Methodology for HAHT-Sediment Interaction

4.7.1 Fundamental Tools and Assumptions for the Methodology Development

At this stage, the calibrated DRW model is coupled with the RANS model, which provides the simulated flow field around and in the wake of the HAHT in the channel. The DRW model uses the RANS velocity field and turbulence variables (κ, ϵ) to simulate the trajectory of particles in the flow field. The goal of this modeling is to understand the effect of the HAHT wake on the sedimentation process of suspended particles in the tidal channel. Since the sedimentation is not an instantaneous effect, but rather depends on the average effect of the velocity deficit on the particle trajectories, the VBM turbine implementation is a good candidate for the simulation of HAHT flow field for sedimentation analysis. Based on our previous studies, the VBM simulates the majority of the turbulent wake, excluding the nearest area one to two radii away from the turbine, with a very good level of approximation [23] [18]. The VBM is much less computational expensive than the SRF model and can thus be used with much larger domains where the cumulative effect of multiple turbines can be studied. Furthermore, the VBM does not have any restrictions on applying boundary conditions and can model asymmetric domains such as the channel bottom effect. As a result, VBM is used in this study to model the particles' sedimentation process.

Suspended particles are considered to have spherical shape, with different Stokes numbers representing different particle sizes and density ratios. The Stokes number is defined as the ratio of the characteristic viscous relaxation time of a particle in a uniform flow to the characteristic time of changes in the flow. Particles with large Stokes number behave follow ballistic trajectories, whereas particles with very small Stokes numbers behave like flow traces. The values of Stokes number considered in this study are 0.01, 0.1, 1 and 10 which correspond approximately to sand ($\rho_p/\rho_f = 2.5$) particles with diameters equal to 0.4, 1, 4 and 12 mm respectively. These particles are injected

in a 20 by 20 injection grid located at the inlet of the tidal channel (figure 4.17). The injection plane dimensions are such that it covers the swept area of the turbine

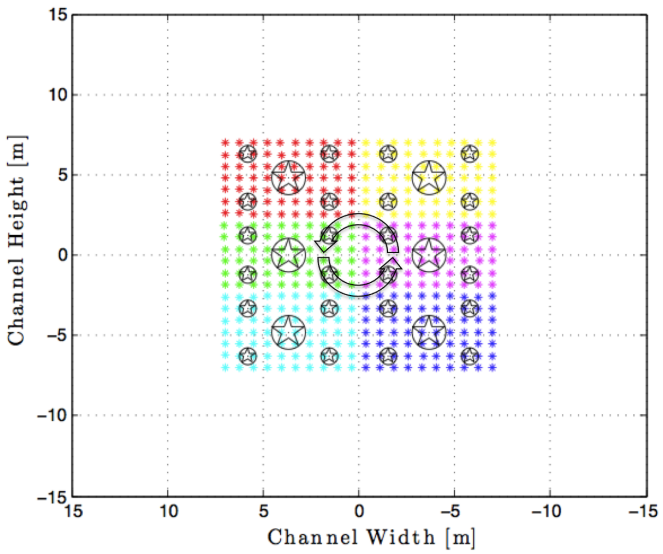

Figure 4.17: **Particle injection plane at the inlet of the tidal channel. Colors show the injection coordinate. Stars and circles show each cloud's center of mass (large symbols) and standard deviation (small symbols) in the tidal channel, with and without turbine respectively. The arrows show the turbine rotation direction. Flow direction is into the plane.**

and a small region in its surroundings. In order to provide the basis for a statistical analysis of the turbine wake effect on particle sedimentation, the DRW model is run ten times, so that the statistics are computed from the trajectories obtained from ten particles injected each initial position (equation 4.2). These injected particles travel along the channel and interact with the velocity deficit in the turbine wake and the accelerated flow around the blades. The decelerated and accelerated flows affect the particle paths and the overall sedimentation process. In order to investigate the effect of the turbine wake on the sedimentation of the modeled particles, each of the

particles is tracked from their initial injection position at the inlet as it is convected and sediments towards the bottom of the tidal channel. Figure 4.17 shows the center of mass of each particle cloud with a large circle or star, and the area where 68% (i.e. plus/minus one standard deviation in a normal distribution of locations) of particles in the cloud sediment is shown by smaller stars and circles. Stars are used to represent the settling location of particles with the turbine in the channel, whereas circles shows the location of particles without the turbine.

4.7.2 Results

The effect of HAHT wakes on sedimentation of suspended particles in a tidal channel is studied in the flow field around the NREL Phase VI turbine modeled with the RANS equations coupled with the VBM turbine implementation and a SST k-ω closure. The choice of the NREL Phase VI as the reference hydrokinetic turbine for this study was motivated by the lack of publicly available data on the DOE Ref 1 at the time of this study. The RANS simulation for this device was calibrated [18] based on a validated numerical methodology [23] and experiments available from the literature. The methodology for sediment analysis is general and can be applied to any HAHT design. In this section, the results of the NREL Phase VI turbine wake interacting with particles with Stokes numbers equal to 0.01, 0.1, 1 and 10. This will provide a general understanding of the physics of this problem and this type of multiphase flow behavior.

$Stokes = 10$

Particles with Stokes number equal to 10 were injected and their trajectories calculated with the calibrated DRW model. Figure 4.18 shows the sedimented particles on the bottom of the tidal channel without turbine (on the left) and with turbine operating in the center of the channel (on the right). The position of the particles is shown in top view, with the $x-$axis as the streamwise coordinate down the channel, and

the $y-$axis as the channel width. Sedimented particles are represented with different colors corresponding to the particle's initial injected position, as shown in figure 4.17. The sedimented particle map is superimposed with the center of mass (large stars and circles) of the particle cloud and the area delimited by two (plus/minus one) standard deviations from the particles center of mass (small stars and circles), containing 68% of the particles in the cloud.

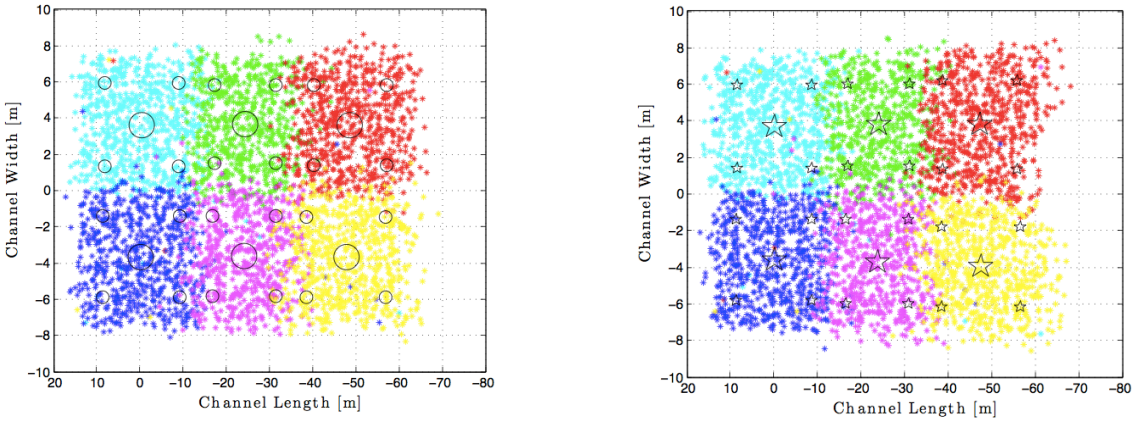

Figure 4.18: **Sedimented particles (St=10) on the bottom of the tidal channel without the turbine (left) and with the turbine (right). Superimposed with center of mass (large stars and circles) of each particle cloud and one standard deviation of particles distribution (small stars and circles) in that cloud. Flow direction is from left to right.**

As observed in this figure 4.18, large Stokes number particles sediment with a pattern similar to their initial injection. Those particles that were injected closer to the bottom of the channel, blue and cyan, sediment earlier. Particles injected farther from the bottom of the channel, red and yellow, sediment at the farthest location from the channel inlet. Due to the effect of turbulence in the flow field, particles disperse randomly, but these small random motions exist in both channels with and

without turbine and are not due to turbine operation in the channel. An interesting observation from the sedimentation of these large particles is the weak divergence of the sedimented particle clouds, which is the signature of turbine wake expansion.
To present a more quantitative comparison between the particle sedimentation in the channel without turbine effect and the channel with turbine effect, figure 4.19 shows a zoomed-in view of center of mass of the particle clouds and the area containing 68% of the sedimented particles (plus/minus one standard deviation from the center). In this figure, large symbols represent the center of mass of each particle cloud and the small symbols represent the limits of the area where most (68%) of the particles sediment in the tidal channel. For these large particles, the center of mass and standard deviation of particle clouds with and without turbine lie on top of each other. However, there exist a slight movement of the center of mass and sedimenting area towards the channels walls when the turbine is in operation. This effect becomes more significant for the particle clouds injected at the top (red and yellow). This is the signature of turbine wake expansion.

$Stokes = 1$

To understand the behaviour of particles that interact more with the turbulent flow, Stokes number was reduced by an order of magnitude to $St = 1$. These particles are more representative of the sediment naturally found in suspension in tidal channels. Injection was at the same locations as particles with $St = 10$, and the trajectories were equally computed with the DRW model using identical settings. Figure 4.20 shows the location of the particles sedimented on the bottom of the tidal channel without (left) and with turbine (right). As shown in this figure, particles with Stokes number equal to one sediment farther in the channel than particles with $St = 10$. Despite these longer trajectories, the inertia of the particles is still the dominant force in their sedimentation process. The comparison of the particles sedimentation in the channel with and without turbine, shows particle clouds on the bottom that are very similar.

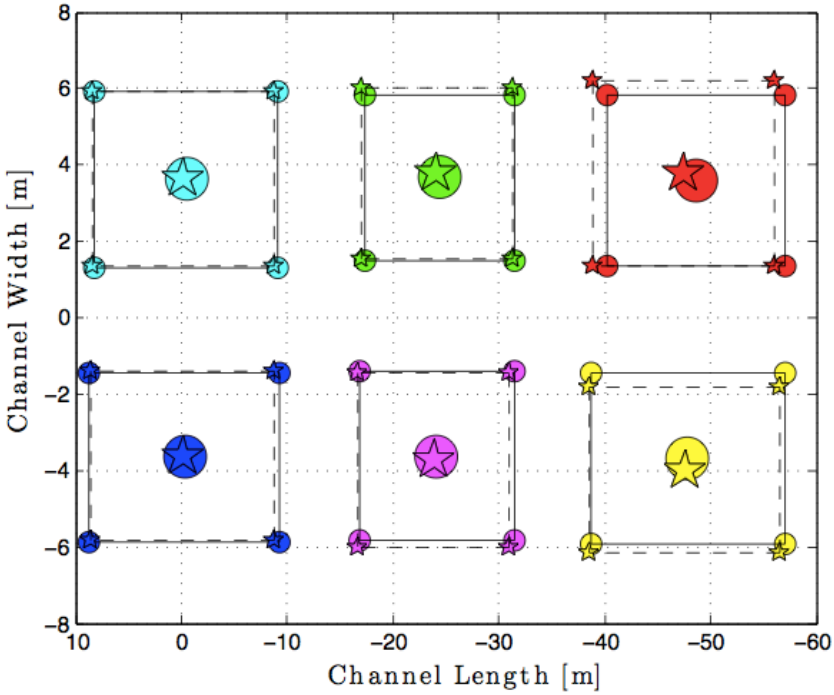

Figure 4.19: **Comparison of the distribution of sedimented St=10 particles in the channel with and without turbine. Stars and circles show each cloud sedimentation in the tidal channel with and without turbine respectively.**

There are a few minor differences within the sedimentation of the top-injected particle clouds, colored red and yellow in the figures, that are worthy of being investigated.

Figure 4.21 shows the zoomed-in view of particle cloud center of mass and sedimenting area. The bottom two particle clouds, cyan and blue, are hardly affected by the turbine effect. The particles injected near the hub height of the turbine, green and magenta, are slightly affected by turbine operation. Turbine operation pushes each particle cloud sideways, towards the channel walls, as can be seen in the displacement of the center of mass and particle sedimenting area for these two particle clouds. An interesting point is highlighted by the influence of turbine operation on the top two

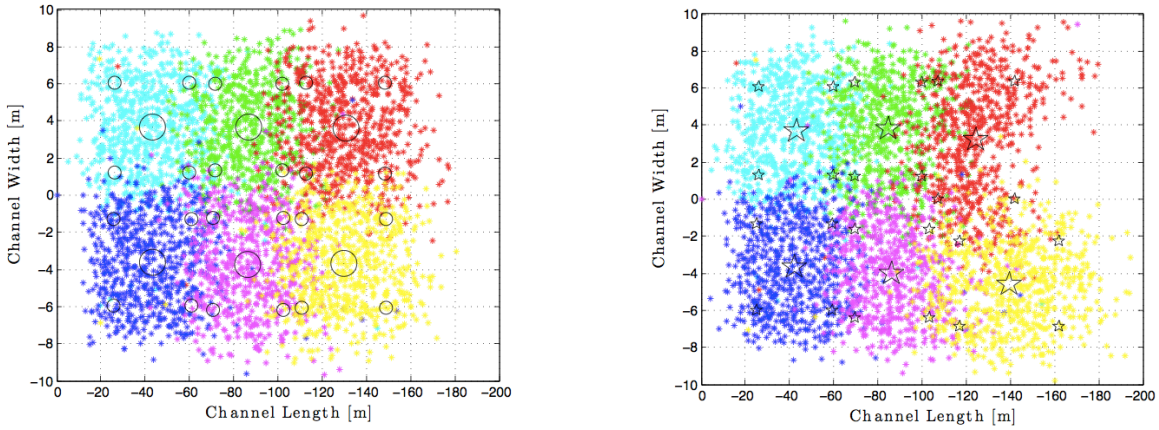

Figure 4.20: **Sedimented particles (St=1) on the bottom of the tidal channel without the turbine (left) and with the turbine (right). Superimposed with center of mass (large stars and circles) of each particle cloud and one standard deviation of particles distribution (small stars and circles) in that cloud. Flow direction is left to right.**

injected particle clouds, red and yellow. The sedimented area for these clouds were reduced by about 28% and 20% in length, due to the wake of the turbine. The signature of the turbine rotation also becomes visible for particles with $St = 1$. The center of mass of the red particle cloud is pushed toward the center of the channel, while the center of mass of the yellow particle cloud is pushed toward the channel walls. Considering turbine sense of rotation is counter clockwise from an observer point of view standing at the channel inlet, this motion of the centers of mass is assumed to be caused by the rotation in the turbine wake.

$Stokes = 0.1$

The investigation of the interaction between the turbine wake and sediment suspended in the tidal channel continues by reducing the particles Stokes number by an order

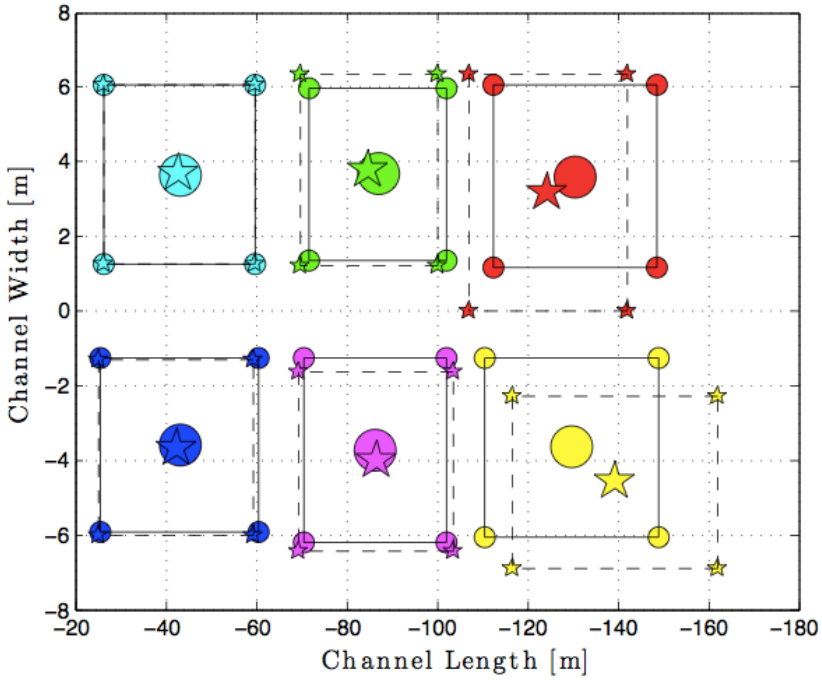

Figure 4.21: **Comparison of the sedimented particles (St=1) distribution in the channel with and without turbine. Stars and circles show each cloud location in the tidal channel with and without turbine respectively.**

of magnitude once again. The effect of turbine wake on the particle sedimentation process for particles with $St = 0.1$ is discussed. The particle tracking and post-processing of the numerical data was done in the same way as for particles with $St = 10$ and $St = 1$.

Figure 4.22 shows the centers of mass and the sedimenting area (where 68% of the particles touch the bottom) of the particle clouds on the channel bottom without turbine (left) and with turbine (right). Similar to the particles with $St = 1$, reducing the Stokes number resulted in particles being affected by the turbulence more, and being convected for longer distances along the channel. The farthest traveled distance

by these particles is slightly more than two times the farthest distance traveled by particles with $St = 1$ (i.e. from 200 m to 450 m downstream the turbine), as opposed to a 10-fold increase in travelled distance as the reduction in laminar settling velocity would predict ($V_z = \tau_p \cdot g$). The right panel of the figure shows that particles injected in different initial locations, and over widely different initial heights (green and red clouds, and magenta and yellow clouds) end up sedimenting in the same region due to significant mixing and enhancement of the settling velocity.

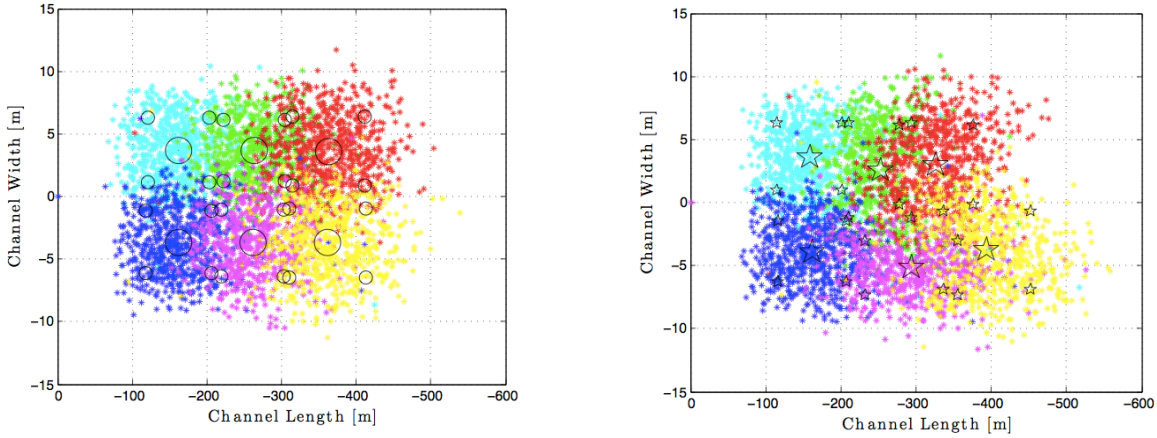

Figure 4.22: **Sedimented particles (St=0.1) on the bottom of the tidal channel without the turbine (left) and with the turbine (right).Superimposed with center of mass (large stars and circles) of each particle cloud and one standard deviation of particles distribution (small stars and circles) in that cloud. Flow direction is from left to right.**

Figure 4.23 shows the zoomed-in view of the particle cloud centers of mass and sedimenting areas. Stars and circles represent the centers of mass and limits of the sedimenting area of each particle cloud in the channel with and without the turbine respectively.The bottom two particle clouds, blue and cyan, are not significantly affected by the turbine operation. The sedimenting of particle clouds in the channel

with and without the turbine lie on top of each other. Particle clouds injected near the hub height, green and magenta, were strongly affected by turbine operation. Similar to the behavior of the top-injected particles (red and yellow) with $St = 1$, turbine rotation strongly affect the sedimentation with motion of the center of mass of the left (green) particle cloud towards the center and the inlet of the channel, and center of mass of the right (magenta) particle cloud towards the wall and the outlet of the channel. The sedimenting area (occupied by 68% of the particles) in the left (green) cloud was widened by about 52%. For the right (magenta) cloud, this value was only 19%. The top particle clouds, red and yellow, were also significantly affected by the turbine rotation. The center of mass of the left (red) cloud moved toward the center and the inlet of the channel, while the center of mass of the right (yellow) particle cloud moved toward the wall and the outlet of the channel. The sedimentation areas were widened by 28% and 8% respectively. The turbine blades are rotating counter clockwise (for an observer looking downstream from the inlet of the channel). As a result of this motion, there exists a downward lift on the particles suspended in the left half plane that results in enhancement of the particle sedimentation. For the particles in the right half-plane, there is a relative motion upwards and that tends to move the centers of mass of the particle clouds suspended in this region towards the channel outlet. One more interesting observation to make is that the combination of the sedimentation enhancement and the relative motion towards the centerline or channel walls due to wake rotation, results in a crest moon shape of the sedimenting area (figure 4.25), which may become a significant feature of sedimentation effects for MHK turbines, and needs to be considered carefully in array design.

$Stokes = 0.01$

The final calculations of the turbine wake-sediment interaction is done for particles with $St = 0.01$. Particles smaller than this are not representative of any realistic particles in a tidal channels and would be expected to follow fluid trajectories based

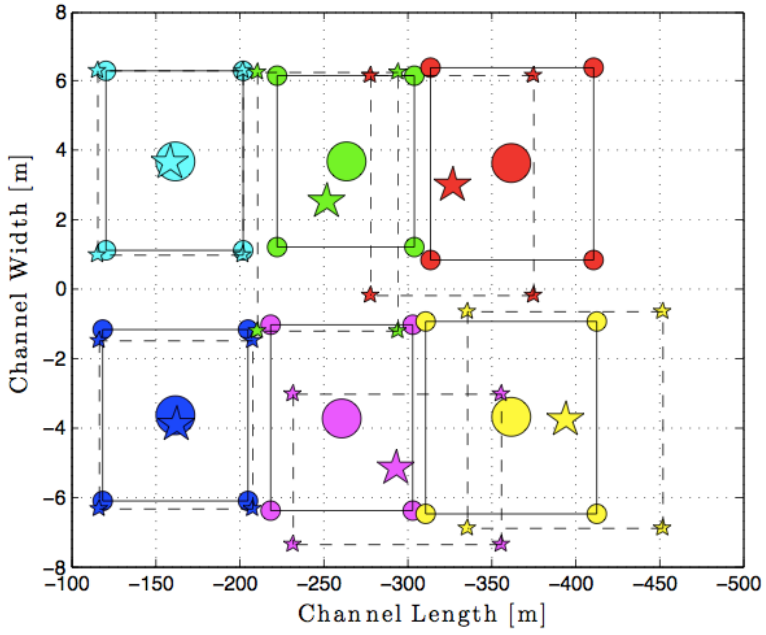

Figure 4.23: **Comparison of the sedimented particles (St=0.1) distribution in the channel with and without turbine. Stars and circles show each cloud sedimentation distribution on the tidal channel bottom, with and without turbine respectively.**

on simple theoretical considerations. It should be noted the post-processing of these smallest particles is little different than for the previous cases: Reduction of the Stokes number of the particles (equivalent to reducing the size/density ratio) further to 0.01, delayed the sedimentation process so that few particles, only from the lower injected clouds, reached the bottom of the channel by the end of the simulation. The rest of the particles were convected along the channel and reached the channel outlet before settling to the bottom.

Figure 4.24 shows particle locations as they reached the outlet of the channel on a vertical plane, across the channel section. This is the same plane shown for

the particle initial injection locations. The right panel of figure 4.24 shows, for the channel without turbine, the particle dispersion and mixing due to the turbulence and a small settling component due to the effect of gravity. When compared to the right panel results, the left hand side of the figure clearly highlights that the particle trajectories are heavily affected by the turbine rotation, but the mean sedimentation is not enhanced.

Figure 4.25 shows the centers of mass and 68%-location of particles at the outlet of the channel. The position of the centers of mass is strongly affected by rotation in the wake, tracking the counter-clockwise motion, but the overall settling is unaffected, the increase on the left hand-side balanced out by the upward motion in the right hand-side. The impact of the turbulence is clear in the spread of the particle clouds. All the squares indicating the position of the majority (68%) of the particles are significantly widened by the presence of the turbine. As discussed for the $St = 0.1$ particles, the effect of rotation and the coupling with the changes in sedimentation, even if they even out when averaged over all the suspended particles, can can lead to a strong crest moon pattern of deposition, that would not be cancelled by some particles in the flow seeing a reduction in settling. This pattern formation needs to be studied carefully in regions where sediment suspension is an issue and where additive effects from bathymetry or arrays can lead to significant non-linear resonance.

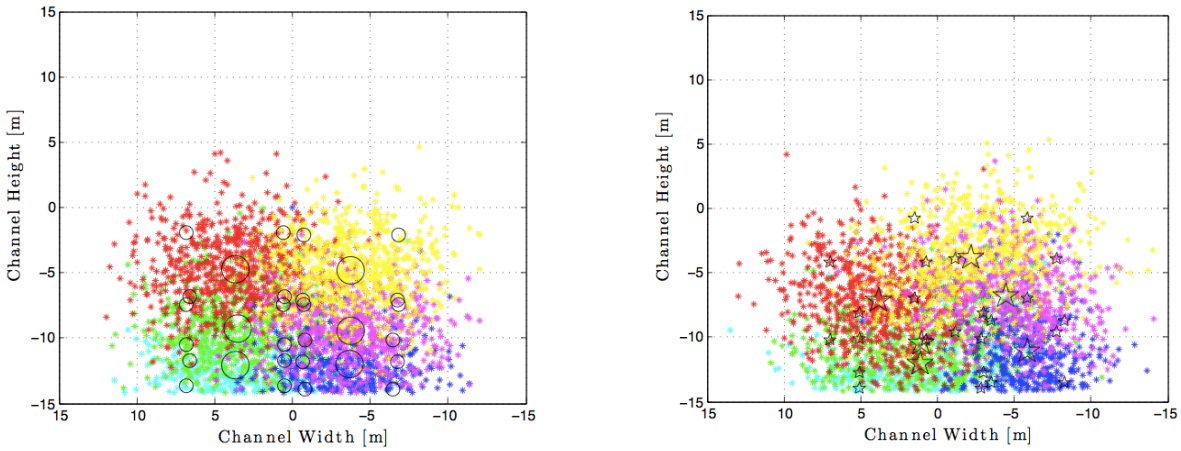

Figure 4.24: **Sedimented particles (St=0.01) on the outlet of the tidal channel without (left) and with turbine (right). Superimposed are centers of mass (large stars and circles) of each particle cloud and one standard deviation sedimenting particle locations (small stars and circles). Flow direction is from left to right.**

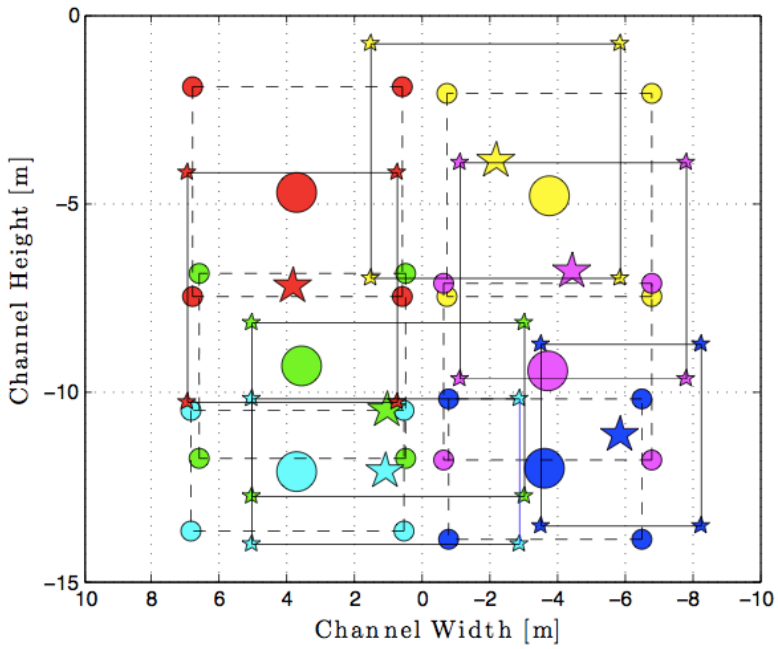

Figure 4.25: **Comparison of the sedimented particle (St=0.01) distribution at the outlet of the channel with and without turbine. Stars and squares show particle locations in a channel without turbine. Circles and triangles show particle locations in a channel with turbine.**

Chapter 5

SUMMARY AND CONCLUSIONS

The conclusions from the research conducted in this thesis are presented. For each of the previous chapters, a brief summary of the research is outlined to provide background and justification for the conclusions.

5.1 Conclusions for the simulation of a single MHK turbine. Chapter 2

In chapter 2 the theory of two numerical models, Single Rotating Reference Frame (SRF) and Blade Element Model (BEM), used to simulate the dynamics of the flow around a Horizontal Axis Hydrokinetic Turbine (HAHT) were presented. Furthermore, the methodology to calculate the 3D lift and drag coefficients along the turbine blade span, using the SRF model, were explained.

The two models, SRF and BEM, were used to simulate the performance and flow field of a laboratory scale and also a full-scale HAHT turbine. The computational domains, boundary conditions, mesh resolution and the techniques used for discretization of the computational domain (meshing) for the two models were discussed. The SRF and BEM results for both cases, lab.-scale and full-scale, were compared against corresponding experimental results (for the lab.-scale device) and other publicly available numerical results (for the full-scale device). The similarities and differences between these results were addressed. The reasons and hypotheses, for these similarities and differences, were investigated and discussed respectively.

In the simulations of the scaled model turbine, comparison between the numerical and experimental results revealed good agreement between measured and predicted turbine efficiency, at TSR values close to the optimum value (≈ 7.5). At these TSR

values, the SRF model with the actual blade geometry showed closer agreement with experimental results. However, the BEM slightly overpredicted the turbine's performance. At the highest TSR (≈ 10), the BEM underpredicted the turbine performance significantly, while the SRF still showed close agreement with the experimental data. Over- and underprediction by BEM are due to the simplifications and idealizations of the flow over the turbine, implicit in this model.

At lower TSR values (5-7) numerical results predicted a reduction in turbine efficiency, due to the increase in angle of attack near the blade root and the formation of a separation region. The experimentally measured efficiency, however, was almost constant. The hypothesis for this disagreement was that the dynamical effect present in the experiment, caused by the fluctuations in the turbine's rotational speed, would result in stall-delay in the region near the blade root, due to delay in the separation at high angles of attack reached at high rate-of-change of the angle of attack. Therefore, the turbine maintains its efficiency in the experiment at low TSR. However, in numerical results, the absence of these dynamical effects causes the turbine performance to decrease as the value of TSR decreases. Numerical and experimental evidence for this hypothesis was presented and discussed in detail.

The measured and modeled velocity and momentum deficit profiles at four different stations, 2, 3, 5 and 7 turbine diameters, downstream of the turbine, were compared against each other. SRF and BEM results showed good agreement, except for a noticeable difference in the very near-wake region (2D downstream). This difference was due to the BEM simplification and hence the lack of ability to model the inhomogeneous near-wake of the turbine, specially right behind the nacelle. In the comparison with experimental data, it was concluded that due to the limitations in capturing the turbulent boundary layer close to the turbine's nacelle, the momentum deficit recovery was underpredicted by both SRF and BEM. The effect of the nacelle's wake enhanced the turbulent mixing with the free stream flow and contributed to the wake recovery in the experiment. SRF and BEM showed limitations to capture this phys-

ical phenomena accurately. The overall trend in these results, however, were very similar and the maximum relative error for the predicted momentum deficit in the wake was of the order of 10%.

In the simulation of a full-scale turbine, the same numerical models, SRF and BEM, were applied toward the modeling of the DOE Reference Model 1 (DOE RM 1) turbine. The results of these simulation were presented and discussed in the last section of chapter 2. The observed flow field dynamics in these simulations were similar to the general physics observed in the scale-model simulations and experiments. These numerical simulations were compared against publicly available results by Lawson et. al. from NREL [11]. The predicted turbine torque (and therefore efficiency since the turbine angular velocity and fluid free stream velocity are the same) in this work was in good agreement with Lawson et. al. results (less than 2% relative error). This agreement provided a benchmark for the full-scale model simulations in this thesis, and showed success in the application of the methodology developed in the course of this research to simulate the performance and wake of a full-scale HAHT, which was the main goal of this part of the study.

5.2 Conclusions for the simulation of an array of MHK and the development of an optimization algorithm. Chapter 3

In chapter 3, the Blade Element Model (BEM) was used to develop a numerical methodology for the performance and wake characterization of HAHTs in an array. The methodology development and validation was done by simulating the experiments performed on various array configuration of scaled-model HAHTs by a previous researcher at UW-NNMREC [17]. Once the methodology was validated, it was applied toward the study of the fluid dynamics in an array of full-scale HAHTs.

In the simulations of experimental analysis, the performance, turbulent wake evolution and interaction of multiple HAHTs was investigated. The experimental measurements were combined with different RANS-based computational simulations that

model the turbines' operation with BEM. The influence of array spacing and TSR on performance and wake velocity structure was investigated in two different array configurations: Two coaxial turbines at different downstream spacing (5D to 14D) and Three coaxial turbines with 5D downstream spacing.

In the simulations for array of two coaxial turbines, the comparison between numerical and experimental devices' performance showed a general good agreement at TSRs close to the optimum TSR (≈ 7.5). It was confirmed that increasing the spacing between two turbines will lead to increase in performance of the downstream turbine. For lower TSR values (≈ 6), a noticeable disagreement between the predicted and measured performance was observed. The numerical results predict lower performance for lower TSR values, while experimental results showed almost no changes in the value of turbines' performance at lower TSR values. This observation was similar to the results for a single device performance. To understand this discrepancy, the stall-delay mechanism, due to the rapid change of angle of attack in the experiments was again proposed. Numerical and experimental results that show a large increase in angular velocity fluctuations in the experiments as the value of TSR decreases below 7 (the peak efficiency value) were presented. This experimental validation process highlighted the influence of spacing and TSR variation on computational predictions of array performance and the characteristics of the flow field inside the arrays, establishing the strengths and limitations of BEM for use in industrially-relevant settings.

In the simulations of an array of three coaxial turbines with fixed spacing (5D), similar behavior for turbines' performance values (compared to turbines' performance trend in the array of two coaxial turbines) were observed. The numerical and experimental values for turbines' efficiency showed good agreement at TRSs close to the optimum value. However, the agreement degraded at lower TSR values. In these simulations, BEM confirmed the experimental observation that in the array of three coaxial turbines, the downstream-most turbine has higher efficiency than the middle

turbine. The hypothesis behind this physical phenomenon was that the existence of the middle turbine would enhance the turbulent mixing in the flow field, extracts relatively small amount of momentum from the flow and therefore enhances the recovery of the wake. In this situation, the downstream-most turbine receives higher incoming kinetic energy flux into its rotor plane (15% more than the middle turbine) and operates more efficiently at a constant TSR.

In the last section of chapter 3, the numerical methodology was applied toward the development of a methodology to study the role of different spacing variables such as downstream row spacing, lateral offset and tip-to-tip distances between turbines. BEM predictions suggested an almost linear relation between the predicted extracted power by turbine and the available kinetic energy flux two radii (2R) upstream the rotor plane. Using this finding, a general numerical methodology was developed to provide minimize the computational cost of array optimization based on the BEM model, and a set of guidelines to propose an optimized array of HAHTs based on spacing and operating conditions constraints.

5.3 Conclusions on Sediment Transport Modeling in MHK sites. Chapter 4

The Discrete Random Walk (DRW) model was used to simulate particle motion in turbulent channel flows. It was shown that the DRW model, as commonly applied, depends strongly on model parameters that have no clear relationship to the physics and, therefore, has a high level of uncertainty for the simulation of particle motion in large-scale, highly turbulent flows. A simple methodology for calibration of the DRW model for turbulent dispersion in flows that can be assumed to behave as, or where particle dispersion is governed predominantly by, homogeneous isotropic turbulence was presented. This methodology made use of G.I. Taylor's dispersion theory to adjust the key non-dimensional parameter that controls the Lagrangian correlation time in the turbulence, thus setting the particle-eddy interaction time statistics in the

particle trajectory.

An experimental validation of the proposed calibration methodology was presented. The numerically-modeled particle dispersion was compared against Snyder and Lumley's experimental data and confirmed the improvement in the results with the DRW model after calibration. It was shown that the proposed calibration methodology, that uses the fundamental Taylor's dispersion theory as a baseline, produced a narrow interval for the values of the time-scale constant C_T, with high confidence. The optimized C_T values varied from the default value by 30%, even with this canonical lab-scale experiment. It was also shown that the calibration method developed in this thesis requires only a few additional simulation tests with particles in a simplified environment. The ability to set a value, or narrow range of values, for the time scale coefficient, C_T in the DRW model that matches theoretical predictions in the same simplified flow improves predictions of the DRW-simulated particle dispersion in similar but more complicated turbulent flows like flow in a tidal channel with an operating HAHT.

In the second part of chapter 4, the calibrated DRW model was used to develop a general numerical methodology for modeling HAHT wake effects on sedimentation of particles of different sizes. This investigation provided a general understanding of particle behavior after interacting with the turbine wake during their sedimentation process. Sedimentation of the particles with large Stokes numbers (St=10) were not significantly affected by the turbine operation. Due to the large Stokes number (i.e. large, heavy particles), the inertia of these particles was the dominant force in their sedimentation process. Therefore, particles follow ballistic trajectories. The only effect of the turbine wake on particle sedimentation was a slight widening of the distribution of particle sedimentation location, following the signature of the turbine wake. Reduction of the Stokes number from 10 to 1, led to particles being convected by the flow field farther along the channel. The sedimentation process for the majority of particles with $St = 1$ was not significantly affected by turbine operation. The only

exception was for the particles that went through the core of the wake, where it was observed that the sedimentation suffered a downward lift due to the turbine sense of rotation. Sedimentation of these particles was enhanced (center of mass moved towards the inlet) and the rotation imparted a motion towards the channel center. The effect is reversed for particles on the opposite side of the turbine, where sedimentation was hindered by an upward lift and the particles moved toward the channel's wall. The net effect, however, was to increase the sedimentation of all particles by a few percent. Particles with Stokes number equal to 0.1 were significantly affected by turbine operation. Particle sedimentation was increased significantly. The rotation of the turbine led to significant lateral motion. The coupling of these two effects led to a crescent moon shaped sedimentation pattern that can produce artificial bathymetry features over long term operation of MHK turbines. Particles with $St = 0.01$ mostly followed the flow field and acted as flow traces. A strong mixing of particle clouds due to the turbulence, with and without the turbine, was observed in our investigation. Due to the blade rotation some particles saw the settling enhanced, while others saw it hindered. While these two effects even out, and the overall mean is not affected, these local changes in the suspended particle dynamics can induce sedimentation patterns, similar to the crescent moon shape found for particles with $St = 0.1$.

Appendix A

MATLAB SCRIPTS FOR CALCULATION OF 3D ANGLE OF ATTACK, LIFT AND DRAG COEFFICIENTS ALONG A HAHT'S BLADE SPAN

A.1 3D Angle of Attack, Lift and Drag Coefficient Calculation for Scaled Model HAHT (Revised DOE RM1)

The MATLAB script to calculate 3D angle of attack, lift and drag coefficients along the scaled model HAHT blade span is provided in this section. This script takes the blade geometry specifications for the design of interest (e.g. scaled model HAHT turbine) in text format. In this input the blade span is discretized into small elements. The radial position (from turbine center), twist angle, chord length and chord thickness of each blade section is provided. A sample of this input file for the scaled model HAHT is provided in this section after the MATLAB script. The other two inputs for this script are integrated the forces on each of the blade sections in the streamwise (F_y) and perpendicular to the streamwise (F_x) directions respectively. These integral values are the output from RANS solver (e.g. SRF model implemented ANSYS FLUENT). The latest version of this MATLAB script and the corresponding input files can be accessed, download and edited at https://github.com/teymourj/scaled-model-MHK.

The MATLAB script takes the above-mentioned three input files in text format along with predefined turbine's operating conditions at the top of the script. It calculates and report the 3D angle of attack, lift and drag coefficients along the blade span using the presented methodology in section 2.1.4 of this thesis. This script also reports the integral variables (i.e. torque, thrust and efficiency) for the turbine. These results can be used toward performance characterization of the turbine and also to generate the

input lift and drag coefficients look-up tables for the Blade Element Theory (BET) based models and simulations (i.e. BEM, Harp-Opt and WT-Perf).

A.1.1 MATLAB Scripts for Scaled Model HAHT

```
% 3D lift and drag coefficients calculation for the scaled model MHK
% turbine (revised DOE RM1). Force data exctrated from SRF simulations
% in ANSYS FLUENT.

clc;
clear all;
close all;

%=====Inputs=================%
%Operating conditions
roh=1000;         %Fluid density [kg/m^3]
v_inf=1.13;       %Free stream velocity [m/sec]
v_local=0.85;     %Unaffected upstream velocity by blade induction [m/sec]
omega=35.96;      %Turbine rotational velocity [rad/sec]

%Blade geometry specifications
pitch_angle=0;

file_geometry='scaled_model_MHK_geometry_sections1.txt';
fid_geometry=fopen(file_geometry,'r');

for j=1
    fgetl(fid_geometry);
end

C_geometry = textscan(fid_geometry, '%f %f %f %f');
fclose(fid_geometry);
```

```
radius=C_geometry{1};
twist=C_geometry{2};
chord=C_geometry{3};
pitch(1:size(radius),1)=pitch_angle;
thickness=C_geometry{4};
%=====Inputs End==============%


%===== Reading/Sorting Streamwise and Perpendicular Forces========%
%=====  on Each Blade Section Extracted from ANSYS FLUENT ========%
line_to_skip=41;

file='scaled_MHK_fx_TSR7p16_SST_KW_final.txt';
fid=fopen(file,'r');

for j=1:line_to_skip
    fgetl(fid);
end
C_x = textscan(fid, '%s %f %f %f %f %f %f');
fclose(fid);
temp_x=C_x{2};

file='scaled_MHK_fy_TSR7p16_SST_KW_final.txt';
fid=fopen(file,'r');

for j=1:line_to_skip
    fgetl(fid);
end
C_y = textscan(fid, '%s %f %f %f %f %f %f');
fclose(fid);
temp_y=C_y{2};
```

```
F_x=temp_x;
F_y=temp_y;

clear temp_x temp_y;
%=====End Reading ANSYS FLUENT Outputs====================

%=====Lift/Drag Coefficiect and Turbine Integral Variable Calculation=====%

beta=atan(v_local./(radius*omega));   %Angle of relative wind in [rad]
v_rel=(v_local^2.+(radius*omega).^2); %Square of relativ velocity in [m/s]
AOA=(beta.*(180/pi))-twist-pitch;     %Angle of Attack

lift_force=F_y.*cos(beta)+F_x.*sin(beta);  %in [N]
drag_force=F_y.*sin(beta)-F_x.*cos(beta);  %in [N]

lift_coeff=lift_force./(0.5*roh*0.007*chord.*v_rel);
drag_coeff=drag_force./(0.5*roh*0.007*chord.*v_rel);

dT=lift_force.*cos(beta)+drag_force.*sin(beta);
thrust=sum(dT)*2                           %in [N]

torque=F_x(2:29,1).*radius(2:29,1);        %in [N-m]

power=2*sum(torque)*omega                  %in [Watt]

efficiency=(power)/(0.5*roh*v_inf^3*pi*(.225^2))

%=====Plot/Report Results=====%
figure(1)
ax1 = gca;
hold on
plot(radius(2:29,1),AOA(2:29,1),'b*-')
hold on
```

```
xlabel('Radius [m]','interpreter','latex','FontSize',12)
ylabel('AOA [-]','interpreter','Latex','FontSize',12)
ax2 = axes('Position',get(ax1,'Position'),...
       'YAxisLocation','right',...
       'Color','none');
ylabel('$C_{L}$ and $C_{D}$ [-]','interpreter','Latex','FontSize',12)
linkaxes([ax1 ax2],'x');
hold on

plot(radius(2:29,1),lift_coeff(2:29,1),'g*--')
hold on

plot(radius(2:29,1),drag_coeff(2:29,1),'r*--')
hold on
grid on



fprintf('min AOA')
disp(AOA(29,1))
fprintf('max AOA')
disp(AOA(2,1))

fprintf('min C_{L}')
disp(lift_coeff(29,1))
fprintf('max C_{L}')
disp(lift_coeff(2,1))



fprintf('min C_{D}')
disp(drag_coeff(29,1))
fprintf('max C_{D}')
disp(drag_coeff(2,1))
%=====End Plot Results=====%
```

—

A.1.2 Blade Geometry of Scaled Model HAHT

Radius	Pre-Twist	Chord	Thickness
0.032	20.07	0.050	0.008
0.038	16.38	0.045	0.007
0.045	13.86	0.041	0.006
0.051	11.98	0.038	0.006
0.058	10.51	0.035	0.005
0.065	9.33	0.033	0.005
0.071	8.35	0.032	0.005
0.078	7.53	0.030	0.005
0.084	6.83	0.029	0.004
0.091	6.24	0.027	0.004
0.097	5.72	0.026	0.004
0.104	5.27	0.025	0.004
0.110	4.88	0.025	0.004
0.117	4.52	0.024	0.004
0.124	4.20	0.023	0.003
0.130	3.91	0.022	0.003
0.137	3.65	0.021	0.003
0.143	3.40	0.021	0.003
0.150	3.16	0.020	0.003
0.156	2.94	0.019	0.003
0.163	2.72	0.019	0.003
0.169	2.51	0.018	0.003
0.176	2.30	0.017	0.003
0.182	2.09	0.017	0.002
0.189	1.87	0.016	0.002
0.196	1.65	0.015	0.002
0.202	1.43	0.014	0.002

```
0.209   1.19    0.014   0.002
0.215   0.95    0.013   0.002
0.222   0.69    0.012   0.002
```

—

A.2 3D Angle of Attack, Lift and Drag Coefficient Calculation for Full-Scale Model HAHT (DOE RM1)

The provided MATLAB script in this section is very similar to the previous script provided in section A.1. This script was written based on the same methodology to calculate 3D lift and drag coefficients and angle of attack along the blade span of the DOE RM1 turbine. This script takes the blade geometry specifications for the design of interest (e.g. DOE RM1) in text format. In this input the blade span is discretized into small elements. The radial position (from turbine center), twist angle, chord length and chord thickness of each blade section is provided. A sample of this input file for the DOE RM1 is provided in this section after the MATLAB script. The other three inputs for this script are integrated the forces on each of the blade sections in the streamwise (F_y) and perpendicular to the streamwise (F_x) directions respectively and the calculated center of pressure for each blade section. These values are the output from RANS solver (e.g. SRF model implemented ANSYS FLUENT). The latest version of this MATLAB script and the corresponding input files can be accessed, download and edited at https://github.com/teymourj/scaled-model-MHK.git. The MATLAB script takes the above-mentioned four input files in text format along with predefined turbine's operating conditions at the top of the script. It calculates and report the 3D angle of attack, lift and drag coefficients along the blade span using the presented methodology in section 2.1.4 of this thesis. This script also reports the integral variables (i.e. torque, thrust and efficiency) for the turbine. These results can be used toward performance characterization of the turbine and also to generate the input lift and drag coefficients look-up tables for the Blade Element Theory (BET)

based models and simulations (i.e. BEM, Harp-Opt and WT-Perf).

A.2.1 MATLAB Scripts for the DOE RM1

```
% 3D lift and drag coefficients calculation for the full-scale model MHK
% turbine (DOE RM1). Force data exctrated from SRF simulations
% in ANSYS FLUENT.

clc;
clear all;
close all;

%=====User Inputs==============
%Operating conditions
roh=1025;      %Density in [kg/m^3]
v_inf=1.9;     %Free stream velocity in [m/sec]
v_local=1.4;   %1D Upstream velocity in [m/sec]
omega=1.2;     %Turbine Anguler velocity in [rad/sec]

%Blade geometry specifications
pitch_angle=0;

file_geometry='DOE_ref_model1_geometry_28sections.txt';
fid_geometry=fopen(file_geometry,'r');

for j=1
    fgetl(fid_geometry);
end
C_geometry = textscan(fid_geometry, '%f %f %f %f %f');
fclose(fid_geometry);

radius=C_geometry{1};
```

```
twist=C_geometry{2};
chord=C_geometry{3};
pitch(1:size(radius),1)=pitch_angle;
thickness=C_geometry{5};

line_to_skip=39;
line_to_skip_center_of_pressure=4;
%=====End User Inputs==============


%===== Reading/Sorting Streamwise and Perpendicular Forces========%
%=====  on Each Blade Section Extracted from ANSYS FLUENT ========%

%=====Forces in the streamwise direction==============
file='fy_seawater_KW.txt';
fid=fopen(file,'r');

for j=1:line_to_skip
    fgetl(fid);
end
C_y = textscan(fid, '%s %f %f %f %f %f %f');
fclose(fid);
temp_y=C_y{4};

%Data rearrangment from root to the tip of the blade
F_y(1:2,1)=temp_y(1:2,1);       %blade0 and 1
F_y(3,1)=temp_y(13,1);          %blade2
F_y(4:10,1)=temp_y(22:28,1);    %blade3  to 9
F_y(11:20,1)=temp_y(3:12,1);    %blade10 to 19
F_y(21:28,1)=temp_y(14:21,1);   %blade20 to 27
clear temp_x temp_y;

%=====Forces perpendicular to streamwise direction==============
```

```
file='fx_seawater_KW.txt';
fid=fopen(file,'r');

for j=1:line_to_skip
    fgetl(fid);
end
C_x = textscan(fid, '%s %f %f %f %f %f %f');
fclose(fid);
temp_x=C_x{4};

%Data rearrangment from root to the tip of the blade
F_x(1:2,1)=temp_x(1:2,1);       %blade0 and 1
F_x(3,1)=temp_x(13,1);          %blade2
F_x(4:10,1)=temp_x(22:28,1);    %blade3  to 9
F_x(11:20,1)=temp_x(3:12,1);    %blade10 to 19
F_x(21:28,1)=temp_x(14:21,1);   %blade20 to 27

%=====Center of presure along the blad span sections==============
file='center_of_pressure_seawater_kw.txt';
fid=fopen(file,'r');

for j=1:line_to_skip_center_of_pressure
    fgetl(fid);
end
C_x = textscan(fid, '%s %f %f');
fclose(fid);
temp_Z_p=C_x{3};

%Data rearrangment from root to the tip of the blade
Z_p(1:2,1)=temp_Z_p(1:2,1);       %blade0 and 1
Z_p(3,1)=temp_Z_p(13,1);          %blade2
Z_p(4:10,1)=temp_Z_p(22:28,1);    %blade3 to 9
Z_p(11:20,1)=temp_Z_p(3:12,1);    %blade10 to 19
```

```
Z_p(21:28,1)=temp_Z_p(14:21,1);   %blade20 to 27
clear temp_Z_p;

%=====End Reading ANSYS FLUENT Outputs====================

%=====Lift/Drag Coefficiect and Turbine Integral Variable Calculation=====%
beta=atan(v_local./(radius.*omega));   %Angle of relative wind in [rad]
v_rel=(v_local^2.+(radius.*omega).^2); %Square of relativ velocity in [m/s]
AOA=(beta.*(180/pi))-twist-pitch;

lift_force=F_y.*cos(beta)+F_x.*sin(beta);  %in [N]
drag_force=F_y.*sin(beta)-F_x.*cos(beta);  %in [N]

lift_coeff=lift_force./(0.5*roh*0.3*chord.*v_rel);
drag_coeff=drag_force./(0.5*roh*0.3*chord.*v_rel);

torque=F_x.*Z_p;

%===== Calculating Integral variables=====%
power=2*sum(torque)*omega/1000  %in [kW]
power_section=torque.*omega/(mean(thickness)*1000);   %in [kW/m]
efficiency=(power*1000)/(0.5*roh*v_inf^3*pi*(10^2-2.8^2))



figure(1)
plot(radius,power_section,'*-')
hleg2=title('Sectional power along span of one turbine blade');
set(hleg2,'interpreter','Latex','FontSize',12);
xlabel('Radius [m]','interpreter','latex','FontSize',12)
ylabel('Sectional Power [kW/m]','interpreter','Latex','FontSize',12)
grid on

figure(2)
```

```
ax1 = gca;
hold on
plot(radius,AOA,'k*-')
hold on
xlabel('Radius [m]','interpreter','latex','FontSize',12)
ylabel('AOA [-]','interpreter','Latex','FontSize',12)
ax2 = axes('Position',get(ax1,'Position'),...
       'YAxisLocation','right',...
       'Color','none');
ylabel('$C_{L}$ and $C_{D}$ [-]','interpreter','Latex','FontSize',12)
linkaxes([ax1 ax2],'x');
hold on
plot(radius,lift_coeff,'g*-')
plot(radius,drag_coeff,'r*-')
hleg2 = legend('Lift Coefficient','Drag Coefficient','Angle of Attack');
set(hleg2,'Location','NorthEast','interpreter','Latex','FontSize',12)
grid on
```

—

A.2.2 Blade Geometry of DOE RM1

local radiuses (m)		Pre-twist averaged	Chord (m)	Blade pitch	Thickness (m)
1.86	12.86	1.118	0	0.703	
2.05	12.86	1.386	0	0.615	
2.35	12.86	1.610	0	0.530	
2.65	12.86	1.704	0	0.470	
2.95	10.99	1.662	0	0.433	
3.25	9.97	1.619	0	0.400	
3.55	9.105	1.577	0	0.378	
3.85	8.365	1.534	0	0.368	
4.15	7.725	1.492	0	0.358	
4.45	7.17	1.45	0	0.348	
4.75	6.68	1.407	0	0.338	
5.05	6.245	1.365	0	0.328	
5.35	5.86	1.322	0	0.317	
5.65	5.515	1.279	0	0.307	
5.95	5.200	1.235	0	0.296	
6.25	4.91	1.192	0	0.286	
6.55	4.64	1.148	0	0.276	
6.85	4.385	1.103	0	0.265	
7.15	4.145	1.058	0	0.254	
7.45	3.915	1.012	0	0.243	
7.75	3.685	0.966	0	0.232	
8.05	3.46	0.92	0	0.221	
8.35	3.24	0.872	0	0.209	
8.65	3.015	0.824	0	0.198	
8.95	2.785	0.776	0	0.186	
9.25	2.55	0.726	0	0.174	
9.55	2.305	0.676	0	0.162	
9.85	2.18	0.626	0	0.15	

—

Appendix B

MATLAB SCRIPT FOR THE DRW MODEL CALIBRATION VIA G.I. TAYLOR'S DISPERSION THEORY

https://github.com/teymourj/Discrete-Random-Walk-Model-Calibration-Script.git

```
% DRW model calibration - Matching the numerical Lagrangian time scale
% coefficient from DRW model with theoretical result from G.I. Taylor
% dispersion theory

clc;
close all;
clear all;

%===========User inputs==========%
Turbulent_intensity_at_inlet=0.01;  %in [-]
Velocity_at_inlet=2;                %in [m/sec]
CL=0.01;                            %in [-]

TI=Turbulent_intensity_at_inlet;
U_ave=Velocity_at_inlet;
%=======End User inputs==========%

%===Loading DRW Data (Extracted data from RANS Solver [ANSYS FLUENT])===%
n_data_drw=10; %Number of data columns
file='calibration_inert_withoutturbine_DRW_500try_allvelprim_TL_Le0point5_CL0point01
fid=fopen(file,'r');
```

```
[data,count]=fscanf(fid,'%f',[n_data_drw inf]);
fclose(fid);

X_drw_all(:,1)=data(1,:);
Y_drw_all(:,1)=abs(data(2,:)-50); %Inlet center coordinate is (0,50,0)
Z_drw_all(:,1)=data(3,:);

v_drw_all(:,1)=data(4,:);
u_prim_drw_all(:,1)=data(5,:);
v_prim_drw_all(:,1)=data(6,:);
w_prim_drw_all(:,1)=data(7,:);

T_drw_all(:,1)=data(8,:);
P_ID_all(:,1)=data(9,:)+1;  %"+1" is to start from Particle ID from 1
TL_drw_all(:,1)=data(10,:);
number_of_tries=max(P_ID_all);
%===End of Loading DRW Data======%

%===Evaluation of the mean Lagrangian time scale T_{L} modeled by DRW===%
count=1;
for n=1 : length(v_prim_drw_all)-1
    if abs(v_prim_drw_all(n+1)-v_prim_drw_all(n))>10^-3 && TL_drw_all(n+1,1)~=0
        TL(count,1)=TL_drw_all(n+1,1);
        u_prim_TL(count,1)=u_prim_drw_all(n+1,1);
        v_prim_TL(count,1)=v_prim_drw_all(n+1,1);
        w_prim_TL(count,1)=w_prim_drw_all(n+1,1);
        count=count+1;
    end
end
I=mean(TL)
%================================%
```

```
%==========Sorting DRW model data for post-processing=============%
%Finding the minimum number of data for each realization (stop).
for m=1 : number_of_tries
    [column]=find(P_ID_all==m);
    stop_mat(m,1)=length(column);
end
stop=min(stop_mat);

for m=1 : number_of_tries

    % Isolating the values of ONE realization for DRW model.
    index=find(P_ID_all==m);
    X_drw(:,1)=X_drw_all(index);
    Y_drw(:,1)=Y_drw_all(index);
    Z_drw(:,1)=Z_drw_all(index);
    v_drw(:,1)=v_drw_all(index);
    u_prim_drw(:,1)=u_prim_drw_all(index);
    v_prim_drw(:,1)=v_prim_drw_all(index);
    w_prim_drw(:,1)=w_prim_drw_all(index);
    T_drw(:,1)=T_drw_all(index);

    %Saving the sorted positions of each realization
    Xp(1:stop,m) = X_drw(1:stop,1);
    Yp(1:stop,m) = Y_drw(1:stop,1);
    Zp(1:stop,m) = Z_drw(1:stop,1);


    %Calculating the displacement of each realization in each direction
    dy(1:stop,m) = Y_drw(1:stop,1) - abs((U_ave*T_drw(1:stop,1)));
    dx(1:stop,m) = X_drw(1:stop,1) - 0;
    dz(1:stop,m) = Z_drw(1:stop,1) - 0;

    %Saving the sorted vel. fluctuation of each realization
```

```
    v_prim(1:stop,m) = v_prim_drw(1:stop,:);
    u_prim(1:stop,m) = u_prim_drw(1:stop,:);
    w_prim(1:stop,m) = w_prim_drw(1:stop,:);


    %Saving the sorted time steps of each realization
    Tp(1:stop,m) = T_drw(1:stop,:);


     if m~=number_of_tries
         clear X_drw Y_drw Z_drw v_drw u_prim_drw v_prim_drw w_prim_drw T_drw
     end

end

clear X_drw_all Y_drw_all Z_drw_all V_drw_all
clear u_prim_drw_all v_prim_drw_all w_prim_drw_all
clear T_drw_all


for j=1 : stop

    dy_rms(j,1)=std(dy(j,:),1);
    dx_rms(j,1)=std(dx(j,:),1);
    dz_rms(j,1)=std(dz(j,:),1);

    v_prime_rms(j,1)=std(v_prim(j,:),1);
    u_prime_rms(j,1)=std(u_prim(j,:),1);
    w_prime_rms(j,1)=std(w_prim(j,:),1);

    Tp_ave(j,1)=mean(Tp(j,:));

end
```

```
%=======End Sorting DRW model data for post-processing=============%

%=======Autocorrelation function and it's integral==========%
count2=1;
for t=2
    count1=1;
        for tau=1 : stop-t
            for j=1:number_of_tries

                R_num(1,j) = (w_prim(t,j)*w_prim(t+tau,j));
                R_denum1(1,j)=(w_prim(t,j)^2);
                R_denum2(1,j)=(w_prim(t+tau,j)^2);

            end

            R_tau(tau,1)=mean(R_num)/(sqrt(mean(R_denum1))*sqrt(mean(R_denum2)));
            kesi(tau,1)=Tp_ave(t+tau)-Tp_ave(t);
            clear R_num;clear R_denum;clear R_denum1;clear R_denum2;
        end

    I_new_all(count2,1)=trapz(R_tau)*mean(diff(Tp_ave))
    I_new_limited(count2,1)=trapz(R_tau(1:50,1))*mean(diff(Tp_ave))

    cmap = hsv(6);  %# Creates a 6-by-3 set of colors from the HSV colormap

    figure(1)
    plot(kesi,R_tau,'-','Color',cmap(1,:))
    title('Velocity Autocorrelation Function','FontSize',14,'FontWeight','bold','Colo
    xlabel('\zeta','FontSize',14,'FontWeight','bold','Color','k')
    ylabel('R_{\zeta}','FontSize',14,'FontWeight','bold','Color','k')
    grid on
    count2=count2+1;
end
```

```
%==============%


%===Statistical Calculation (G.I Taylor Disperssion Theory)===%
LHS_v=(sqrt(2*I*Tp_ave)).*v_prime_rms;
LHS_u=(sqrt(2*I*Tp_ave)).*u_prime_rms;
LHS_w=(sqrt(2*I*Tp_ave)).*w_prime_rms;

%All Realizations dispersion Map
figure(2)
plot(Yp,Zp,'*')
title(['Realizationzs path - C_T = ',num2str(2*CL),' - TI = ',num2str(TI)])
xlabel('Y [m]')
ylabel('Z [m]')
grid on
axis([0 200 -5 5])

%Numerical (DRW) vs. Theoretical (G.I. Taylor) dispersion comparison
figure(3)
plot(Tp_ave,dy_rms,'.')
hold on
plot(Tp_ave,LHS_v(1:stop,1),'r.')
hold on
title(['Y Direction - C_T = ',num2str(2*CL),' - TI = ',num2str(TI)])
xlabel('t [sec]')
ylabel('RMS(Y)')
hleg1 = legend('DRW prediction','G.I Taylor theory');
set(hleg1,'Location','NorthWest')
xlim([0 100])
Ylim([0 1.50])
grid on
```

```
figure(4)
plot(Tp_ave,dx_rms,'.')
hold on
plot(Tp_ave,LHS_u(1:stop,1),'r.')
hold on
title(['X Direction - C_T = ',num2str(2*CL),' - TI = ',num2str(TI)])
xlabel('t [sec]')
ylabel('RMS(Y)')
hleg1 = legend('DRW prediction','G.I Taylor theory');
set(hleg1,'Location','NorthWest')
xlim([0 100])
Ylim([0 1.50])
grid on

figure(5)
plot(Tp_ave,dz_rms,'.')
hold on
plot(Tp_ave,LHS_w(1:stop,1),'r.')
hold on
title(['Z Direction - C_T = ',num2str(2*CL),' - TI = ',num2str(TI)])
xlabel('t [sec]')
ylabel('RMS(Y)')
hleg1 = legend('DRW prediction','G.I Taylor theory');
set(hleg1,'Location','NorthWest')
xlim([0 100])
Ylim([0 1.50])
grid on
```

```
#include "udf.h"
#include "dpm.h"

DEFINE_DPM_SCALAR_UPDATE(suspended_particles, c, t, initialize, p)
{
  FILE *fpy1;
   real pressure, x[ND_ND],y[ND_ND];
   int ID;
   pressure=C_P(c,t);
   C_CENTROID(x,c,t);
   fpy1=fopen("calibration_inert_withoutturbine_DRW_500try_allvelprim_TL_Le0point5_CI

       fprintf(fpy1,"%f %f %f %f %f %f %f %f %d %f\n",P_POS(p)[0], P_POS(p)[1], P_POS

   fclose(fpy1);
}
```

BIBLIOGRAPHY

[1] Boon J. D. *Secrets of the tide: tide and tidal current analysis and applications, storm surges and sea level trends.* Horwood, 2004.

[2] Garrett C. and Cummins P. The efficiency of a turbine in a tidal channel. *Journal of Fluid Mechanics*, 588:243–251, 2007.

[3] Couch S., Bryden I., and Jeffrey H. Tidal current energy: Development of a device performance protocol. In *International Conference on Clean Electrical Power (ICCEP)*, 2007.

[4] Bahaj A., Batten W., Molland A., and Chaplin J. Power and thrust measurments of marine current turbines under various hydrodynamic flow conditions in a cavitation tunnel and a towing tank. *Renewable energy*, 32:407, 2007.

[5] Batten W., Chaplin J., Bahaj A., and Molland A. Experimentally validated numerical method for hydrodynamic design of horizontal axis tidal turbines. *Ocean Engineering*, 34:1013, 2007.

[6] Barnsley M. and Wellicome J. Final report on the second phase of development and testing of a horizontal axis wind turbine test rig for the investigation of stall regulation aerodynamics. Technical report, 1990.

[7] Wind energy handbook. *Burton T., Sharpe D., Jenjins N., and Bossanyi E.* Wiley, 2000.

[8] Batten W., Chaplin J., Bahaj A., and Molland A. The prediction of the hydrodynamic performance of marine current turbines. *Renewable energy*, 33:1085, 2008.

[9] Ng K. W. and Wei H. L. 20022012: 10 years of research progress in horizontal-axis marine current turbines. *Energies*, 6:1497–1526, 2013.

[10] Michelen C., Murray J., Neary V., and Barone M. Cactus open source code for hydrokinetic turbine design and analysis: Model performance evaluation and public dissemination as open source design tool. In *Proceedings of the 2nd Marine Energy Technology Symposium, Seattle*, 2014.

[11] Lawson M., Li Y., and Sale D. Development and verification of a computational fluid dynamics model of a horizontal-axis tidal current turbine. In *Proceedings of the 30th International Conference on Ocean, Offshore, and Arctic Engineering*, 2011.

[12] Kang S., Borazjani I., Colby J. A., and Sotiropoulos F. Numerical simulation of 3d flow past a real-life marine hydrokinetic turbine. *Advances in Water Resources*, 2012.

[13] Gunawan B., Michelen C., Neary V., Coe R., Johnson E., Fontaine A., Meyer R. S., and Jonson M. Straka W. Model validation using experimental measurements from the garfield thomas water tunnel at the applied research laboratory (arl) at penn state university. In *The 2nd Marine Energy Technology Symposium*, April 2014.

[14] Polagye B., Cavagnaro R., Niblick A., Hall T., Thomson J., and Aliseda A. Cross-flow turbine performance and wake characterization. In *Proceedings of the 1st Marine Energy Technology Symposium, Washington, DC.*, 2013.

[15] Bachant P. and Wosnik M. Performance measurements of cylindrical- and spherical-helical cross-flow marine hydrokinetic turbines, with estimates of exergy efficiency. *Renewable Energy*, 2014.

[16] Bachant P. and Wosnik M. Reynolds number dependence of cross-flow turbine performance and near-wake characteristics. In *The 2nd Marine Energy Technology Symposium*, April 2014.

[17] Stelzenmuller N. Marine hydrokinetic turbine array performance and wake characteristics. Master's thesis, University of Washington, 2013.

[18] Javaherchi T. Numerical modeling of tidal turbines: Methodology development and potential physical environmental effects. Master's thesis, University of Washington, 2010.

[19] Hansen M. O. L., Sørensen J. N., Michelsen J. A., and N. N. Sørensen. A global Navier-Stokes rotor prediction model. *AIAA Paper 97-0970*, 1997.

[20] Carcangiu C. E. *CFD-RANS Study of Horizontal Axis Wind Turbines*. PhD thesis, Universit degli Studi di Cagliari, 2008.

[21] Duque E. P. N., Johnson W., van Dam C. P., Cortes R., and Yee K. Numerical predictions of wind turbine power and aerodynamic loads for the NREL phase II combined experiment rotor. *AIAA Paper 2000-0038*, 2000.

[22] Sørensen N. N., Michelsen J. A., and Schreck S. Navier stokes predictions of the nrel phase vi rotor in the nasa ames 80 ft * 120 ft wind tunnel. *Wind Energy*, 5:151, 2002.

[23] Javaherchi T., Antheaume S., and Aliseda A. Hierarchical methodology for the numerical simulation of the flow field around and in the wake of a horizontal axis wind turbine: Rotating reference frame, blade element method and actuator disk model. *Wind Engineering*, 38:181–201, 2014.

[24] Hand M., Simms D., Fingersh L., Jager D., Cotrell J., Schreck S., and Larwood S. Unsteady aerodynamics experiment phase 6: Wind tunnel test configurations

and available data campaigns. Technical report, National Renewable Energy Laboratory (NREL), 2001.

[25] Blanchfield J., Rowe A., Wild P., and Garrett C. The power potential of tidal streams including a case study for masset sound. In *Proceedings of the 7th European Wave and Tidal Energy Conference, EWTEC*, 2007, 1114 September, Porto, Portugal.

[26] Clarke J., Connor G., Grant A., and Johnstone C. Design and testing of a contra-rotating tidal current turbine. *Proceedings of the Institution of Mechanical Engineers, Part A: Journal of Power and Energy*, 221:171179, 2007.

[27] Harrison M., Batten W., and Bahaj A. A blade element actuator disc approach applied to tidal stream turbines. In *OCEANS 2010, IEEE*, 2010.

[28] Turnock S., Phillips A., Banks J., and Nicholls-Lee R. Modelling tidal current turbine wakes using a coupled rans-bemt approach as a tool for analysing power capture of arrays of turbines. *Ocean Engineering*, 38:1300–7, 2011.

[29] Guanghui B., Jun L., Pengfei F., and Guojun L. Numerical investigations of the effects of different arrays on power extractions of horizontal axis tidal current turbines. *Renewable Energy*, 53:180–186, 2013.

[30] Churchfield M. J., Li. Y., and Moriarty P. J. A large-eddy simulation study of wake propagation and power production in an array of tidal-current turbines. *Phil. Trans. R. Soc. A*, 371, 2013.

[31] Divett T., Vennell R., and Stevens C. Optimization of multiple turbine arrays in a channel with tidally reversing flow by numerical modelling with adaptive mesh. *Phil. Trans. R. Soc. A*, 371, 2013.

[32] ODoherty D., Mason-Jones A., ODoherty T., Byrne C., Owen I., and Wang W. Considerations of improved tidal stream turbine performance using double rows

of contra-rotating blades. In *Proceedings of the 8th European wave and tidal energy conference. Uppsala, Sweden.*, 2009.

[33] Polagye B., Cleve B. V., Copping A., and Kirkendall K., editors. *Environmental Effects of Tidal Energy Development*, number NOAA Technical Memorandum NMFS F/SPO-116, 22-25 March 2010.

[34] Bassett C., Thomson J., and Polagye B. Sediment-generated noise and bed stress in a tidal channel. *Journal of Geophysical Research*, 118 (4):2249–2265, 2013.

[35] Bassett C., Thomson J., and Polagye B. Characteristics of underwater ambient noise at a proposed tidal energy site in puget sound. *MTS/IEEE Oceans 2010, Seattle*, 2010.

[36] Abernethy C. S., Amidan B. G., and Cada G. F. Simulated passage through a modified kaplan pressure regime: A supplement to "laboratory studies of the effects of pressure and dissolved gas supersaturation on turbine-passed fish". Technical report, Pacific Northwest National Laboratory, 2002.

[37] Abernethy C. S., Amidan B. G., and Cada G. F. Laboratory studies of the effects of pressure and dissolved gas supersaturation on turbine-passed fish. Technical report, Pacific Northwest National Laboratory, 2001.

[38] Abernethy C. S., Amidan B. G., and Cada G. F. Fish passage through a simulated horizontal bulb turbine pressure regime: A supplement to "laboratory studies of the effect of pressure and dissolved gas supersaturation on turbine-passed fish". Technical report, Pacific Northwest National Laboratory, 2003.

[39] Romero-Gomez P. and Richmond M. C. Discrete element modeling of blade-strike frequency and survival of fish passing through hydrokinetic turbines. *Proceedings of the 2nd Marine Energy Technology Symposium, Seattle*, 2014.

[40] Dehbi A. A CFD model for particle dispersion in turbulent boundary layer flows. *Nuclear engineering and design*, 238:707–715, 2008.

[41] Berlemont A., Picart A., and Gouesbet G. The code disco-2 for predicting the behaviour of discrete particles in turbulent flows and its comparison against the code disco-1 and experiments. In *Third international conference on numerical methods in laminar and turbulent flows, Seattle, WA, Pineridge Press, White Plains.*, 1983, pp. 963-973.

[42] Berlmont A., Desjonqueres P., and Gouesbet G. Particle lagrangian simulation in turbulent flows. *International journal of Multiphase flows*, 19:19–34, 1990.

[43] Brown D. J. and Hutchinson P. The interaction of solid on liquid and turbulent fluid flow fields-a numerical simulation. *Journal of Fluids Engineering*, 101:265–269, 1979.

[44] Wilcox D. C. *Turbulence Modeling for CFD, 3rd edition.* DCW Industries, Inc., La Canada CA, 2006.

[45] Chen P. P. and Crow C. T. One the monte-carlo method for modeling particle dispersion in turbulence. In *Gas-Solid flow, energy sources technology conference, New Orleans*, 1984 (10) 37-41.

[46] Coimbra C. F. M., Shirolkar J. S., and Queiroz McQuay M. Modeling partice disperssion in a turbulent, multiphase mixing layer. *J. of wind engineering and Industrial Aerodynamics*, 73:79–97, 1998.

[47] Couch S. and Bryden I. Large-scale physical respose of the tidal system to energy extraction and its significance for informing environmental and ecological impact assessment. In *Ocean 2007 - Europe*, 2007.

[48] Simms D, Schreck S, Hand M, and Fingersh L-J. Nrel unsteady aerodynamics experiment in the nasa-ames wind tunnel: A comparison of predictions to measurements. Technical report, National Renewable Energy Laboratory (NREL), 2001.

[49] Milojević D. Lagrangian stochastic-deterministic (lsd) prediction of particle dispersion in turbulence. *Particle & particle systems characterization*, 7:181–190, 1990.

[50] Di Carlo A. and Foscoloand P. U. Hot syngas filtration in the freeboard of a fluidized bed gasifier: Development of a cfd models. *Powder Technology*, 222:117–130, 2012.

[51] Dufresne M., Vazquez J., Terfous A., Ghenaim A., and Poulet J. B. Cfd modeling of solid separation in three combined sewer overflow chambers. *Journal of environmental engineering*, 135:776–787, September 2009.

[52] Dufresne M., Vazquez J., Terfous A., Ghenaim A., and Poulet J. B. Experimental investigation and cfd modeling of flow, sedimentation, and solids separation in a combined sewer detention tank. *Computers & fluids*, 38:1042–1049, 2009.

[53] Elghobashi S. Particle-laden turbulent flows: direct simulation abd closure model. *Applied Scientific Research*, 48:301–314, 1991.

[54] Elghobashi S., Abou-Arab T., Rizk M., and Mostafa A. Prediction of the particle laden jet with a two-equation turbulence model. *International journal of Multiphase flows*, 10:697–710, 1984.

[55] Arnason G. *Measurments of particle dispersion in turbulent pipe flow.* PhD thesis, Washington State University, 1982.

[56] Taylor G.I. Diffusion by continuous movements. *Eddy motion in the atmosphere, Phil Trans*, page 1, 1915.

[57] Gosman A. D. and Ioannides E. Aspects of computer simulation of liqud-fueled combustors. *Journal of Energy*, (7)-6:482–490, 1983.

[58] Graham D. I. and James P. W. Turbulent dispersion of particles using eddy interaction models. *International journal of Multiphase flows*, 22:157–175, 1996.

[59] Greenfield C. and Quarini G. Particle deposition in a turbulent boundary layer, including the effect of thermophoresis. In *FEDSM97-3902 ASME fluids engineering division summer meeting*, June 22-26.

[60] Hutchinson P., Hewitt G. F., and Dukler A. E. Despersion of liquid or solid dispersions from turbulent gas stream: A stochastic model. *Chemical Engineering Science*, 26:419–439, 1971.

[61] Javaherchi T., Stelzenmuller N., and Aliseda A. Experimental and numerical analysis of a scale-model horizontal axis hydrokinetic turbines. In *The 2nd Marine Energy Technology Symposium*, April 2014.

[62] Javaherchi T., Stelzenmuller N., and Aliseda A. Experimental and numerical analysis of the doe reference model 1 horizontal axis hydrokinetic turbine. In *The 1st Marine Energy Technology Symposium*, April 2013.

[63] Dukowicz J. K. A particle-fluid numerical model for liquid sparys. *Journal of Computational Physics*, 35:229–253, 1980.

[64] Laith Z. and Rajagopalan R. Navier-stokes calculations of rotor-airframe interaction in forward flight. *Journal of the American Helicopter Society*, 40(2):57, 1995.

[65] Leybros A., Roubaud A., Guichardon P., and Boutin O. Supercritical water oxidation of ion exchange resins in a stirred reactor: Numerical modelling. *Chemical Engineering Science*, 69:170–180, 2012.

[66] Losurdoa M., Spliethoffa H., and Kielb J. Ash deposition modeling using a visco-elastic approach. *Fuel*, 102:145–155, 2012.

[67] Ruith M. Unstructured, multiplex rotor source model with thrust and moment trimming - fluent's vbm model. In *AIAA Applied Aerodynamics Conference*, 2005.

[68] Manwell J. F., McGowan J. G., and Rogers A. L. *Wind Energy Explained*. John Wiley & Sons.

[69] Maxey M. R. and Riley J. J. Equation of motion for a small rigid sphere in a nonuniform flow. *Phys. Fluids*, 26:883, 1983.

[70] Mazur Z., Campos-Amezcua R., Urquiza-Beltra'n G., and Garcia-Gutie'rrez A. Numerical 3d simulation of the erosion due solid particle impact in the main stop valve of a steam turbine. *Applied Thermal Engineering*, 24:1877–1891, 2004.

[71] Morsi S. and Alexander A. An investigation of particle trajectories in two-phase flow system. *Journal of Fluid Mechanics*, 55(2):193–208, 1972.

[72] Neary V. S., Hill C., Chamorro L. P., Gunawan B., and Sotiropoulos F. Experimental test plan doe tidal and river reference turbines. Technical report, Oak Ridge National Laboratory, 2012.

[73] Ormancey A. and Martinon J. Prediction of particle dispersion in turbulent flow. *Physico-Chemical hydrodynamics*, 5:229–244, 1983.

[74] Patel T., Laurence G., and Faram M. G. Grit removal from wastewater using secondary currents in open-channel flow around bends. *Journal of Environmental ENgineering*, 137:1026–1039, 2011.

[75] Stephen B. Pope. *Turbulent Flows, Chapter 7, section 7.1.3*. Cambridge University Press, 2006.

[76] Menter F. R. Two-equation eddy-viscosity turbulence models for engineering applications. *AIAA Journal*, 32(8):1598–1605, 1994.

[77] Rybalko M., Loth E., and Lankford D. A lagrangian particle random walk model for hybrid rans/les turbulent flows. *Powder Technology*, 221:105–113, 2012.

[78] Shams M., Ahmadi G., and Smith D. Computational modeling of flow and sediment transport and deposition in meandering rivers. *Advances in Water Resources*, 25:689, 2002.

[79] Shams M., Ahmadi G., and Smith D. Computational modeling of flow and sediment transport and deposition in meandering rivers. *Advances in Water Resources*, 25:689, 2002.

[80] Shuen J. S., Chen L. D., and Faeth G. M. Evaluation of stochastic model of partice dispersion in a turbulent round jet. *AICHE J.*, 29:167–170, 1983.

[81] Shuen J. S., Chen L. D., and Faeth G. M. Evaluation of stochastic model of partice dispersion in a turbulent round jet. *AICHE J.*, 29:167–170, 1983.

[82] Snyder W. H. and Lumley J. L. Some measurments of particle velocity autocorelation function in turbulent flow. *J. Fluid Mech*, 48:41–71, 1971.

[83] Sommerfield M., Kohnen G., and Ruger M. Some open questions and inconsistencies of lagrangian particle dispersion models. *9th Symp turbulent shear flows, Kyoto, Japan*, pages 16–18, 1993.

[84] Tian L. and Ahmadi G. Particle deposition in turbulent duct flows-comparisons of different model predictions. *Aerosol Science*, 38:377, 2006.

[85] T. Twidell, J. & Weir. *Renewable Energy Resources (2nd edition)*. Taylor & Francis, 2006.

[86] Wang Y. and James P. W. Assessment of ann eddy-interaction model and its refinments using predisctions of droplet deposition in a wave-plate demister. *Trans. Institution of chemical engineers*, 77-part A:692–698, 1999.

[87] Wells M. R. and Stock D. E. The effects of crossing trajectories on dispersion of particles in a turbulent flow. *J. Fluid Mech.*, 136:31–62, 1983.

[88] Warsi Z.U.A. *Fluid Dynamics, Theoretical and Computational Approaches.* CRC Press, 1993.

[89] Zhou Q. and Leschziner M. A. A time-orrelated stochastic model for particle dispersion in anisotropic turbulence. *8th symp turbulent shear flows, Technical University of Munich Germany*, 1991.